ULTRAFAST LATTICE DYNAMICS IN EXCITONIC SELF-TRAPPING OF QUASI-ONE DIMENSIONAL MATERIALS

By

FRANCIS XAVIER MORRISSEY III

A dissertation submitted in partial fulfillment of
the requirement for the degree of

DOCTOR OF PHILOSOPHY

Materials Science Program

MAY 2007

To the Faculty of Washington State University:

The members of the Committee appointed to examine the dissertation of FRANCIS XAVIER MORRISSEY III find it satisfactory and recommend that it be accepted.

_____

Chair

_____

_____

ACKNOWLEDGEMENTS

I would like to thank my advisor, Susan Dexheimer, for her support and advice during my graduate studies and without whom this dissertation would not have been possible. Her drive to solve scientific and technical problems, and enthusiastically encourage the execution of creative ideas has provided a standard for me to aspire to. Attending her course in quantum electronics provided valuable fundamentals.

I wish to express my sincere thanks to my colleague, Vasudevan Nampoothiri, who provided precious help in maintaining and troubleshooting laser system "issues" and for numerous insightful discussions. I would also like to thank all of the previous members of our laboratory for their tireless work that led to the initial laboratory built laser system, instrumentation, and data acquisition programs. I am particularly indebted to the work completed by Aaron Van Pelt, a MX pioneer, who identified the spectroscopic signature of excitonic self-trapping, the work for which I briefly reviewed in Chapter 4.

It is a pleasure for me to thank Jim Brozik, Basil Swanson, and Wayne Buschmann for preparation and characterization of the single-crystal samples. I thank Sergey Avanesyan for building the noncollinear optical parametric amplifier and his assistance with the Spectra-Physics Hurricane system. I thank Win Maw Hlaing Oo for his assistance in taking magnified exposures of the PtX crystals. I thoroughly enjoyed the insightful discussions with Dennis Merritt and Gary Vaillancourt over technical difficulties with the Spectra-Physics Hurricane Femtosecond System and the BMI α-1000 US 1 kHz Femtosecond Regenerative Amplifier, respectively. My skills in resolving plumbing impediments have been greatly enhanced. I thank Steve Langford for his nearly uninterrupted supply of liquid nitrogen and Tom Dickinson for his generous and

reasonable rescheduling of laser time on the 5th floor femtosecond tunable laser source. The fabrication of special mounts and intermediaries would have been impossible without the guidance and assistance of the knowledgeable technical staff, headed by George Henry, in the Instrument Shop. I would also like to thank Duke Beattie and Fred Schuetze of the Electronics Shop for their assistance in acquiring electronic components and advice in troubleshooting.

I thank my committee for their generous contribution of time; particularly, Matt McCluskey, for his assistance with issues including: vacuum system particulars, cryostat concerns, sample mounting, and liquid helium transfer questions. Participation in his solid state physics class proved invaluable.

I would also like to thank the members of the Physics Department and the Materials Science Program staff for their contributions; particularly, Lori Bruce. I was quite impressed with the department's enthusiastic (and financial) support for "Solid State Day", which provided a means, for not only the author, but many other crystal revelers to partake in a celebration of crystals. I would also like to thank the department for nominating me to the role of master of ceremonies as the famed Galileo Galilei during the annual pumpkin drop carried out from the 12th floor of the multi-million dollar Kate B. Webster Physical Sciences Building. My participation in this event, along with the successful execution of the very rigorous falling bodies experiment, wouldn't have been possible without the diligent assistance of numerous department members.

It has been a pleasure to work with former members of our laboratory including: Jianhua Liu and Keith Myers; Petros Zerom and Chengping Zhang (both of whom happened to also be my office cohorts). Best wishes go out to the next generation of scientists, Jason Mance, Grant

Eastland, and Chris Hamner, who will partake in spectroscopic investigations under the guidance of Susan Dexheimer.

Special thanks to my classmates for their unending support and encouragement: Natnael Embaye, Weiya Zhang, Jalal Nawash, Pavlo Rudenko, Juefei Zhou, Christopher Dudley, and Curtis Osterhoudt. I thank the following physicists for enjoyable and thought provoking discussions at various non-sanctioned physics events: Chris Bates, John Leraas, Brandon Shibley, Megan Betts, and Ashley Tracey.

I am grateful to my long time friend, Brian Welch, for his generosity during my few visits to the east coast. His expertise in nuclear "spallation(s)" is extensive. I thank my girlfriend, Thuy Hoang, for her optimism and support during the later portion of my graduate work and for the use of her laptop for my exam presentation. My interest in science is due in part to my past mentors, whose zeal was unprecedented: (high school) David Shalter, (undergraduate physics) Neil Shea, Madan Varma, Robert Tanczyn, and (Oak Ridge National Laboratory) Steve Allison. With great enthusiasm, I would like to thank my family, especially my parents, Fran and Marianne, for their patience and support.

Lastly, I would hope to extend my gratitude to the **multitude** of readers who will pour over this document with extraordinary intensity at the wee hours of the night wondering, "What is the nature of the interplay between localization and delocalization?" or "What does it mean to say *negative* $\Delta T / T$?" or "Why do the higher harmonics of the ground state dephase faster?" or "Does the spatial extent of the exciton change as it evolves to the equilibrated self-trapped state?" To all those readers – **enjoy!**

This work was financially supported by the National Science Foundation.

Ultrafast Laser Spectroscopy Group, 2001

Washington State University, Pullman WA

Left to Right: Petros Zerom, Jianhua Liu, Vasudevan Nampoothiri,

Susan Dexheimer, Author *(with IR Viewer)*, and Chengping Zhang

Users of the Femtosecond Tunable Laser Source, 2005

Washington State University, Pullman WA

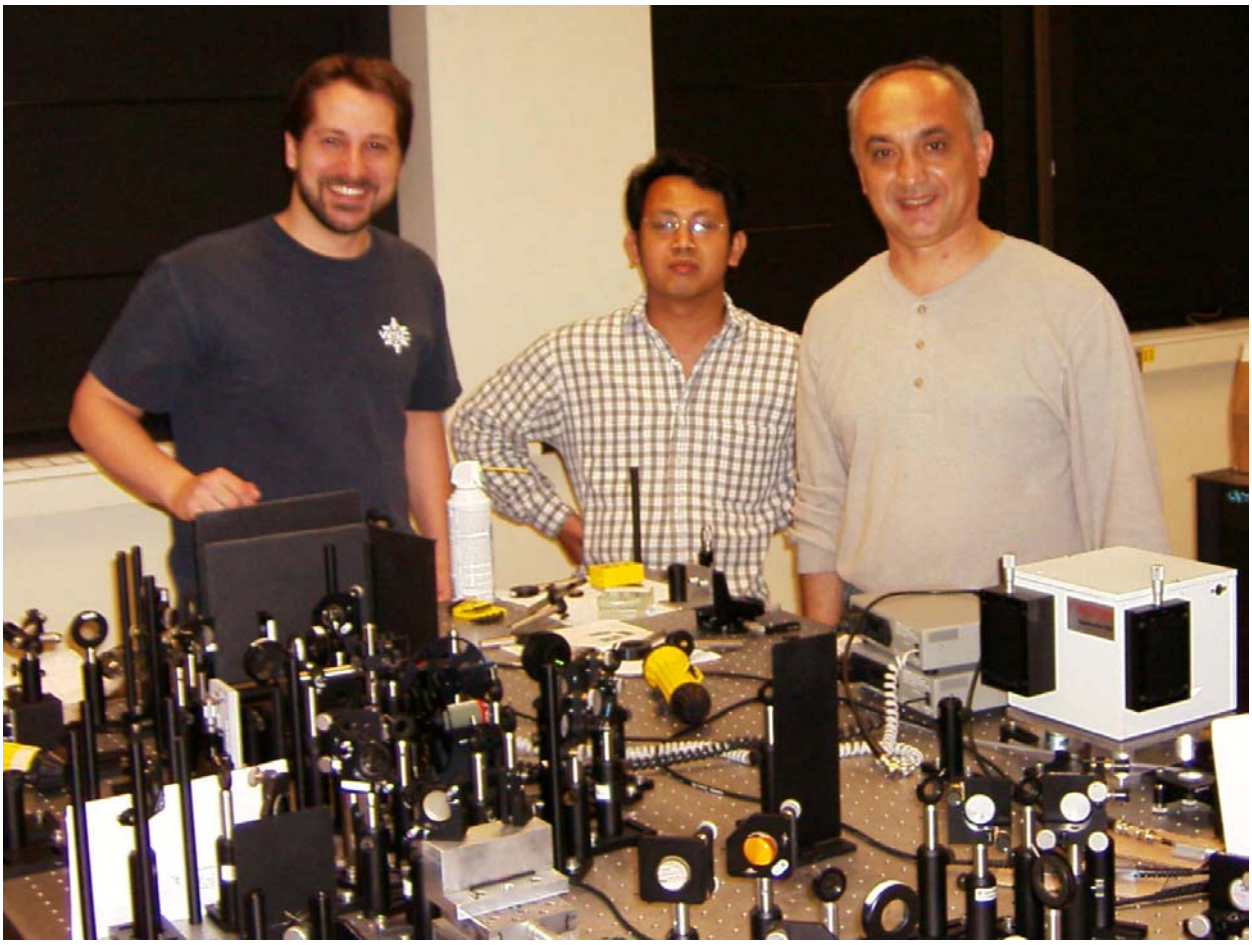

Left to Right: Author, Win Maw Hlaing Oo, and Sergey Avanesyan

For why, who writes such histories as these
Doth often bring the reader's heart such ease,
As when they sit and see what he doth note,
Well fare his heart, say they, this book that wrote!

John Higgins

Lest men suspect your tale untrue,
Keep probability in view.
The traveler leaping o'er those bounds,
The credit of his book confounds.

The painter who pleased Nobody and Everybody.

John Gay

He was in logic a great critic,
Profoundly skilled in analytic;
He could distinguish and divide
A hair, 'twixt south and southwest side;
On either which he would dispute,
Confute, change hands, and still confute;
He'd undertake to prove, by force
Of argument, a man's no horse;
He'd prove a buzzard is no fowl,
And that a lord may be an owl,
A calf an alderman, a goose a justice,
And rooks committee-men and trustees.
He'd run in debt by disputation,
And pay with ratiocination:
All this by syllogism true,
In mood and figure he would do.

From "Hudibras," Part I. Canto I.

Dr. Samuel Butler

All nature is but art, unknown to thee;
All chance, direction, which thou canst not see;
All discord, harmony not understood;
All partial evil, universal good;
And spite of pride, in erring reason's spite,
One truth is clear, Whatever is, IS right.

Essay on Man, Epistle I.

Alexander Pope

ULTRAFAST LATTICE DYNAMICS IN EXCITONIC SELF-TRAPPING

OF QUASI-ONE DIMENSIONAL MATERIALS

Abstract

by Francis Xavier Morrissey III, Ph.D.
Washington State University
May 2007

Chair: Susan Dexheimer

This dissertation presents an investigation of the localization of electronic excitations via electron-lattice interactions. Electronic localization is an important fundamental process in molecular-based electronic materials. Femtosecond vibrationally impulsive excitation techniques were used to directly time-resolve the lattice motion associated with the self-trapping dynamics in halogen-bridged mixed-valence linear chain complexes, $[Pt(en)_2X_2][Pt(en)_2]$, en = ethylenediamine ($C_2H_8N_2$) and (X = Br^- and I^-), or PtX.

Three sets of experimental studies were conducted:

(1) The investigation of PtI, representing the weak electron-phonon coupling limit, revealed a low frequency modulation of the induced absorbance that was assigned to the motion that drives the system to the self-trapped state. A formation component, which decays within approximately a single period of the low frequency motion, is assigned to the transfer of population from the free exciton to the self-trapped state. Previous impulsive excitation measurements on PtBr and PtCl, in conjunction with the PtI measurements in this dissertation, uncover the dependence of the self-trapping dynamics on electron-phonon coupling strength.

(2) The vibrational frequency of a characteristic mode of the self-trapped exciton in its equilibrated structure was determined using a multiple pulse pump-pump-probe sequence. Time-domain excited state resonant stimulated impulsive Raman excitation of PtBr revealed a vibrational mode associated with the equilibrated self-trapped exciton at 125 cm^{-1}. The upward shift in frequency from the final state of the intervalence charge transfer transition at 110 cm^{-1} to the equilibrated configuration is consistent with an increased degree of localization in the stabilized structure.

(3) Low temperature pump-probe measurements on PtBr uncovered an acoustic phonon response seen as a large amplitude 11 cm^{-1} modulation of the induced absorbance. Using this frequency, the localized lattice deformation was estimated to have a spatial extent of ~ 5 unit cells, which reflects the size of the self-trapped exciton, consistent with theoretical models for polaron formation. An enhancement of the excited state wavepacket dephasing time indicates that the vibrational coherence properties of the exciton at room temperature are not simply limited by the excited state structural distortion.

Table of Contents

List of Tables

List of Figures

For those who take from their surroundings what is needed,
and make of it something more.

Chapter 1

Introduction

This dissertation presents an investigation of the localization of electronic excitations via electron-lattice interactions. Electronic localization is an important fundamental process in a wide range of electronic materials, and can dramatically affect a material's optical and electronic transport properties. The following chapters present investigations into the fundamental physics of localized photoinduced electronic states of quasi-one-dimensional crystals; particularly, the halide-bridged mixed-valence transition metal linear chains. In these materials the creation of an electron-hole pair, or exciton, deforms the surrounding lattice resulting in the exciton's confinement or self-trapping.

The halide-bridged mixed-valence transition metal linear materials examined in this study are ideal for investigating the dynamics due to the material's strong electron-phonon coupling. In these materials, the relative interaction strength of the electron-phonon coupling can be chemically tuned by halide substitution in the molecular chains. This allows for a systematic investigation into the self-trapping dynamics as a function of relative electron-phonon coupling strength. The interaction between the lattice vibrations and the electronic dynamics of these materials is integral for exciton self-trapping. In these systems, optically induced charge transfer initiates a lattice motion resulting in the electronic localization, or self-trapping. The reduced dimensionality of these materials simplifies the resulting vibrational dynamics since the dominant motion occurs along the chain axis. The properties of the materials are discussed in Chapter 2.

To time-resolve the vibrational dynamics associated with the self-trapping of the exciton, impulsive excitation is employed. By using short laser pulses (as compared to the material's characteristic vibrational periods) to excite the material, the electronic and vibrational dynamics can be time-resolved. In these femtosecond spectroscopic measurements, the dynamics associated with the self-trapping of the exciton is investigated. The experimental method and equipment used to investigate the self-trapping dynamics are discussed in Chapter 3.

The experiments presented in this dissertation include: (1) measurements of excitonic self-trapping dynamics in the weak electron-phonon coupling limit in Chapter 4, (2) multiple-pulse excitation measurements investigating the dynamics of the equilibrated self-trapped exciton in Chapter 5, and (3) temperature dependent studies that reveal acoustic phonon dynamics associated with the self-trapping of the exciton in Chapter 6. The overall conclusion of these studies is presented in Chapter 7.

The investigation of the weak electron-phonon coupling limit revealed the dynamics that drive this system to the self-trapped state. These results, in conjunction with previous impulsive excitation measurements on the intermediate and strong electron-phonon coupled systems, provide a comparison of the dependence of the self-trapping dynamics on the relative coupling strength over a wide range.

The vibrational frequency of a characteristic mode of the self-trapped exciton in its equilibrated structure was determined using multiple pulse excitations. Time-domain excited state resonant stimulated impulsive Raman excitation of PtBr revealed the motion associated with the equilibrated self-trapped exciton.

Low temperature measurements have uncovered an acoustic phonon response seen as a large amplitude modulation of the induced absorbance of the exciton. In a simple physical

picture, the acoustic waves generated during self-trapping appear as replicas of the local lattice deformation. Using the measured acoustic frequency, the localized lattice deformation was estimated to have a spatial extent of ~ 5 unit cells. This deformation reflects the size of the self-trapped exciton consistent with theoretical models for polaron formation. Also observed was an increase in the vibrational coherence time of the excited state optical phonon oscillation associated with the self-trapping of the exciton. This increase indicates that the vibrational dephasing at room temperature is not simply limited by the excited state structural distortion.

Chapter 2

Properties of the Platinum Halide Complexes

2.1 Materials

The materials chosen for this study are a class of quasi-one-dimensional systems known as halide-bridged mixed-valence transition metal linear chains. From this class, the most extensively investigated systems are the platinum ethylenediamine complexes: $[Pt(en)_2X_2][Pt(en)_2]\cdot Y$, en = ethylenediamine ($C_2H_8N_2$), Y = $(ClO_4^-)_4$ or $(PF_6^-)_4$, or simply PtX(en), where the X represents one of three halides (Cl^-, Br^-, I^-) [1-5]. The studies presented herein examine the PtX(en) complexes, which were selected for the following reasons. By varying the halides, systematic tuning of the relative strength of the electron-phonon coupling allows for a methodical investigation of the localization of electronic excitations. Furthermore, the reduced dimensionality of these complexes leads to a strong coupling and a simplification of the vibrational dynamics. These three properties are discussed in more detail subsequently.

The organization of the chapter is as follows: First the ground state structural properties and their tunability are introduced. Then the optical properties and vibrational modes are reviewed. The theoretical modeling of the PtX system is discussed. The chapter ends with a review of the experimental observations of self-trapped excitons in these materials. Various properties of the PtX complexes (discussed throughout the remaining sections) are summarized at the end of section 2.5 in Table 2.1.

The PtX(en) crystal structure, determined by x-ray diffraction, is shown on the left hand side of Figure 2.1, where three unit cells of the chain are depicted. These linear chains consist of alternating platinum and halide ions, which define the one-dimensional geometry. The platinum

ions are transversely coordinated by ethylenediamine ligands in a nearly square planar configuration. The right hand side of Figure 2.1 shows the crystal packing viewed down the chain axis. The crystals are composed of an array of linear chains that are arranged parallel to one another. The counterions spatially separate the chains minimizing chain to chain interactions and also serve to balance the overall charge in the crystal. The crystals used in these studies have either PF_6^- or ClO_4^- counterions. In these cases, the substitution of different counterions results in only minor variations of the chain-axis properties.

Early synthetic procedures for preparing PtBr(en) were plagued with chlorine contamination [6] as seen by additional features in the vibrational spectra [7]. This fine structure in the ground state vibrational spectrum appeared similar to the effect of isotope splitting of the vibration seen in PtCl(en) [8]. Chlorine contamination level ≥ 10% significantly affected the ground state vibrational properties of PtBr(en) at excitation wavelengths near 800 nm, with a key signature being a strong defect mode at 210 cm^{-1} [9]. Three common preparations surveyed showed that two of the later synthetic routes still produced PtBr(en) with 1-3% Cl contamination [10]. Earlier preparations also yielded defects corresponding to an excess of either $Pt^{+(3+\delta)}$ or $Pt^{+(3-\delta)}$ charge states which can give rise to sub-gap defect states as seen in the optical absorption spectrum [1].

The materials in this study were synthesized by Jim Brozik [11] and Wayne Bushmann [1,12] using improved methods for preparing PtX crystals that are largely free of defects. The $[Pt(en)_2I_2][Pt(en)_2]\cdot(ClO_4)_4$, the $[Pt(en)_2Br_2][Pt(en)_2]\cdot(ClO_4)_4$, and the $[Pt(en)_2Br_2][Pt(en)_2]\cdot(PF_6)_4$ crystals were used to investigate the weak coupling limit (Chapter 4), the vibrational properties of the equilibrated self-trapped exciton (Chapter 5), and acoustic phonon dynamics (Chapter 6), respectively.

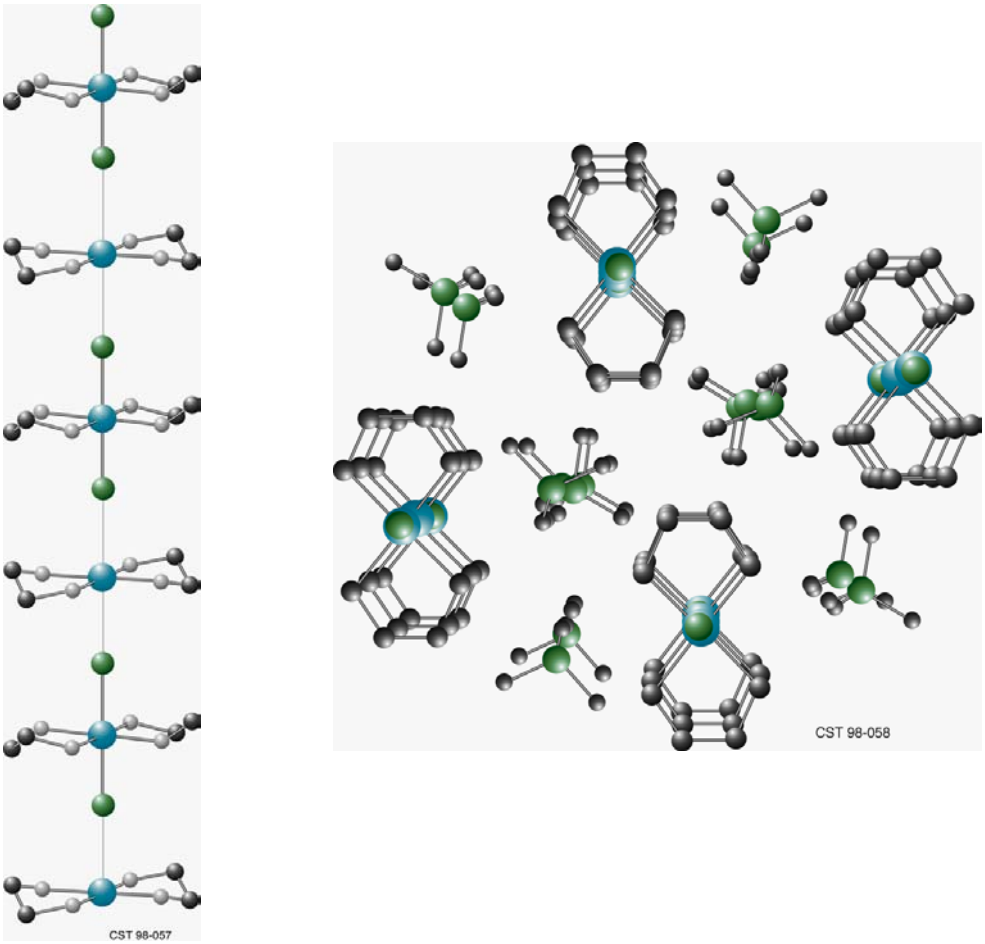

Figure 2.1: Left hand side: three unit cells of a PtX crystal chain. Each Pt (in blue) is coordinated by two ethylenediamine units (in **gray** and **black**) in a near square planar geometry. The bridging halides (in green) connect the Pt sites along the chain. H atoms are omitted for clarity.

Right hand side: the PtX chain and counterion arrangement, viewed down the direction of the chain axis. The structures were determined from x-ray diffraction studies. (Reprinted with permission from B. Swanson, J. Brozik, S. Love, G. Strouse, A. Shreve, A. Bishop, W.-Z. Wang, and M. Salkola, Physical Review Letters, 1999. **82**(16): pp. 3288-3291. Copyright 1999, American Physical Society.)

2.2 Ground State of the Material

The PtX system in the ground state has a chain axis lattice distortion due to a Peierls instability. For a one-dimensional material with a partially filled band, Rudolf Peierls found that the regular chain structure would never be stable [13]. Furthermore, the unstable regular chain structure stabilizes by a reconfiguration of its electronic density resulting in lower electronic symmetry. The stability of this transition is due to a gain in the binding energy caused by a lowering of the occupied electronic states. The lowering of these states occurs at vertical breaks in the energy band resulting from the change in symmetry. For a one-dimensional chain, there always exists a distortion that results in a net reduction in energy [13]. The idea of this instability follows directly from the Jahn-Teller theorem, which states that "a molecular system in a degenerate electronic state will be unstable and will undergo a distortion to form a system of lower symmetry and lower energy thereby removing the degeneracy" [14]. The degree of the distortion is limited by the increase in elastic energy of the lattice.

In the PtX systems, this instability results in a periodic bond length distortion, which is seen as alternating metal-halide bond lengths. This distortion is accompanied by a mixed-valence character on the Pt sites representative of a commensurate charge density wave (CDW). For PtX, the periodic distortion has a period of twice the metal-metal separation, which doubles the length of the unit cell. The platinum ions possess mixed-valence states, having alternating charge of either $+(3+\delta)$ or $+(3-\delta)$, where δ can have a values ranging from zero to one. The possibility of a fractional value is due to the delocalization of the electronic wavefunction over a number of alternating platinum sites. Reflecting this charge disproportionation, the platinum-halide bond lengths are distorted, where the halide ions (X^-) are closer to the $Pt^{+(3+\delta)}$ ions than the $Pt^{+(3-\delta)}$ ions.

Neglecting the ligands and counterions, two unit cells representing this mixed-valence character of the lattice in the ground state can be represented schematically as:

… -------X^----$Pt^{+(3+\delta)}$--- X^-------- $Pt^{+(3-\delta)}$------- X^----$Pt^{+(3+\delta)}$--- X^-------- $Pt^{+(3-\delta)}$…

2.3 Chemical Tuning by Halide Substitution

Halide substitution in the PtX complexes varies the strength of the CDW, which corresponds to a change in the charge distribution and bond lengths. The strength of the electron-lattice interaction ranges from strong to weak coupling as the halide is varied through the progression from Cl, Br, to I. A change in the valence delocalization is observed as the halide is varied based on modeling of x-ray photoelectron spectra [15,16]. This study found that δ is 0.91 for PtCl(en), 0.64 for PtBr(en), and 0.36 for PtI(en). This progression of delocalization parallels the increase in the radius of the halide, which enhances the transfer energy between metal ions. Metal halide interactions of the d_{z^2} (the z-axis being along the chain axis) of the Pt ion with the $5p_z$ orbitals of I and the $4p_z$ orbitals of Br enhance the electronic delocalization. The d_{z^2} interaction with the $3p_z$ orbital of Cl is weaker, consistent with PtCl(en) being near to the highly localized limit (δ = 1) [2].

The increased delocalization of the CDW correlates with a reduction of the lattice distortion amplitude [2]. The degree of lattice distortion, determined from x-ray diffraction of PtX(en), is characterized by the ratio of the short to the long metal-halide bond lengths, which varies as ρ ~ 0.743, 0.828, and 0.890 (viz., 2.319 Å and 3.122 Å; 2.484 Å and 3.001 Å; 2.712 Å and 3.048 Å) for X as Cl, Br, and I, respectively [17-19].

2.4 Optical Properties

The PtX crystals possess highly anisotropic optical properties. The intense optical absorption spectra of PtX are dominated by a metal-metal intervalence charge transfer (IVCT) transition. The IVCT transition transfers charge density between inequivalent platinum ions, and is strongly polarized along the chain axis. Figure 2.2 shows the optical absorption of the PtX(en) complexes transformed from powder diffuse reflectance measurements taken by Buschmann et al. [1]. The IVCT energy is peaked at 24100 cm^{-1} (415 nm), 17250 cm^{-1} (580 nm), and 12900 cm^{-1} (775 nm) for X = Cl, Br, and I. Wada et al. [15] measured the absorption spectra of the PtX(en) complexes transformed from reflectivity spectra of the single crystals where the incident light was polarized along the chain axis. The single crystal measurements are shifted in the IVCT energy (as compared to the diffuse reflectance results) where the peak values occur at 2.72 eV (456 nm), 1.95 eV (636 nm), and 1.37 eV (905 nm) for X = Cl, Br, and I.

The final state of the IVCT transition is a charge transfer exciton. Excitons are electrically neutral electron-hole pairs bound by a mutual Coulomb interaction [20-22]. In electronic band theory, excitonic states are found between the conduction and valence band since the negative Coulomb energy reduces the total excitation energy that would be needed to form a free electron and hole. In one-dimensional systems, the optical absorption band is dominated by excitons [23-25]. The lineshape of the absorption band has been modeled for the one-dimensional case and found to have a dominant contribution from the charge transfer exciton [26,27].

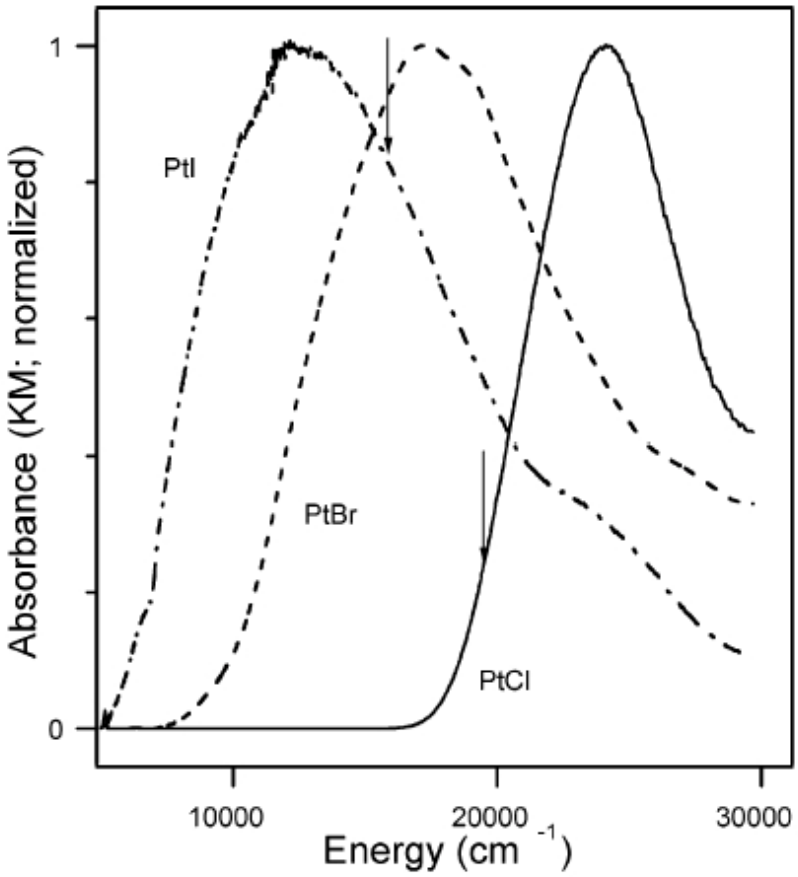

Room-temperature absorption spectra, presented as a Kubelka−Munk transform of diffuse reflectance data, for $[Pt(en)_2X_2]$-$[Pt(en)_2](ClO_4)_4$ where X = Cl (solid); X = Br (dotted); X = I (dot−dash). Spectra are normalized to the same peak value. From left to right, arrows correspond to 632.8 and 514.5 nm, which were the excitation wavelengths used for high-resolution resonance Raman spectroscopy in this work (632.8 nm for PtI and PtBr, 515.4 nm for PtCl).

Figure 2.2: The absorption spectra of the PtX(en) complexes transformed from powder diffuse reflectance measurements. The peak energies are quoted in the text. (Reprinted with permission from Buschmann, W., S. McGrane, and A. Shreve, Journal of Physical Chemistry A, 2003. **107**(40): pp. 8198-8207. Copyright 2003, American Chemical Society.)

2.5 Vibrational Modes

The PtX complexes possess vibrational modes along the chain axis, which have been extensively characterized [1,4,5,8-10,28-30]. The unit cell contains two platinum and two halide ions, which give rise to four chain axis vibrational modes. Symmetry considerations dictate which vibrations are infrared-active and which are Raman-active. Infrared absorption is permitted if the vibrational symmetry is the same as one of the components of the electronic dipole moment. Raman scattering [31] is permitted if the vibrational symmetry is the same as one of the components of the polarizability. An important distinction is that the infrared absorption is dependent on the intrinsic dipole moment of the system while the Raman effect is dependent on the dipole moment induced by the incident electric field. Group theory provides a powerful method that takes advantage of the system symmetry for determining the selection rules for these two processes. An eloquent exposition on this topic can be found in Reference [32].

The Raman-active symmetric stretch mode (ν_1) has the halide ions moving symmetrically about the platinum ions. There are two infrared-active modes. The higher frequency (ν_2) involves asymmetric halide ion motions about the platinum ions and the low-frequency mode (ν_3) involves relative motion of the platinum ions. The fourth mode is an acoustic mode, which is optically inactive in the ground state. The optically active ground state modes are represented schematically as:

$$\begin{array}{cccc} & \leftarrow & \rightarrow & \\ (\nu_1)\ \ldots\ \text{-------}\ Pt^{+(3-\delta)}\ \text{-------}\ X^{-}\ \text{---}\ Pt^{+(3+\delta)}\ \text{---}\ X^{-}\ \text{-------}\ Pt^{+(3-\delta)}\ \text{-------}\ldots & & & \\ \rightarrow & \leftarrow & \leftarrow & \rightarrow \\ (\nu_2)\ \ldots\ \text{-------}\ Pt^{+(3-\delta)}\ \text{-------}\ X^{-}\ \text{---}\ Pt^{+(3+\delta)}\ \text{---}\ X^{-}\ \text{-------}\ Pt^{+(3-\delta)}\ \text{-------}\ldots & & & \end{array}$$

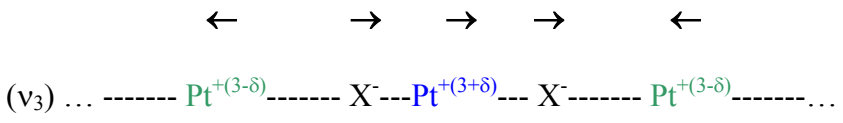

Due to the symmetries of the modes, only the symmetric stretch mode (ν_1) is coupled to the IVCT transition, so only the totally symmetric mode will be displaced in the exciting state.

The frequencies of the Raman-active symmetric stretch mode are 315 cm^{-1} (period = 106 fs) for PtCl(en), 175 cm^{-1} (period = 191 fs) for PtBr(en), and 127 cm^{-1} (period = 263 fs) for PtI(en). These frequencies are within the capacity of the time-resolved techniques used by the author due to the short optical pulses employed in the measurements (i.e., impulsive excitation) discussed in more detail in the next chapter.

X	e-ph coupling strength	δ (charge)	ρ (Å/Å)	E_{IVCT} peak (eV) ((nm))	ν_1 (cm^{-1})
Cl	Strong	0.91	0.743	2.72 (456)	315
Br	Intermediate	0.64	0.828	1.95 (636)	175
I	Weak	0.36	0.890	1.37 (905)	127
	(throughout)	2.2, 2.3	2.3	2.4	2.5

Table 2.1: Properties of the PtX(en) complexes as a function of the halide (X): electron-phonon (e-ph) coupling strength, degree of charge disproportionation (δ) [15,16], ratio of the short to long Pt-X bond lengths (ρ) [17-19], peak energy of the metal-metal intervalence charge transfer transition excitation (E_{IVCT}) [15], and the Raman-active symmetric stretch mode (ν_1) [4,5,28-30]. The final row identifies the section in which property is discussed.

2.6 Theory of Exciton Self-Trapping

2.6.1 Conditions for Self-Trapping

The idea of self-trapping (autolocalization) was first proposed by Lev Davidovich Landau, who correctly suggested the possibility of observing optical spectra associated with momentarily bound charge [33], which are now referred to as self-trapped excitons or exciton-polarons [34,35]. For the case of self-trapping, the formation of the exciton deforms the surrounding lattice and results in its own confinement.

For the general case of a free exciton in a crystal, the electronic excitation is subjected to two opposing interactions: delocalization and localization. The competition between these two interactions, namely, the energy reduction due to delocalization versus the relaxation of the lattice resulting from localization, leads to the criteria for the self-trapping condition [23]. The delocalization interaction can be thought of as the maximum energy released when the localized exciton is allowed to extend throughout the lattice. This is equivalent to the absolute value of the transfer energy between neighboring sites times the number of nearest neighbors, which is equal to half the exciton bandwidth. The localization interaction can be thought of as the stabilization gained by the lattice distortion. Therefore, two states are possible: the self-trapped state where the exciton localizes by an induced lattice distortion, and the free state where the exciton is delocalized in absence of the induced lattice distortion.

Elementary quantum theory dictates that a one-dimensional square well always has at least one bound state [36]. More sophisticated theoretical investigations into the nature of the localization as a function of dimensionality [24,37] revealed that a free exciton in one-dimension experiences a barrierless transition to the self-trapped state. Yutaka Toyozawa gives the general

case of self-trapping stability [24,34,35]:

$$g > \frac{\pi^2}{2d\left(N^{\frac{2}{d}-1}\right)} \tag{2.1}$$

where g is the electron-phonon coupling strength, d is the dimensionality, and N is the number of atoms in the lattice. The electron-phonon coupling strength is defined as the ratio of the relaxation energy of the lattice due to the localized exciton and the maximum energy released when a localized exciton is allowed to extend throughout the lattice. In one-dimension, the free exciton state is unstable when the electron-phonon coupling is greater than approximately the inverse of the number of atoms in the lattice. For the macroscopic approximation where N is very large suggests that any macroscopic one-dimensional system with a non-zero electron-phonon coupling strength will be stable to only the self-trapping case. Furthermore, this barrierless transition leads to extremely rapid formation dynamics of the self-trapping in one-dimension, which would be expected to occur on the order of a single vibrational period of the lattice.

2.6.2 Peierls-Hubbard Hamiltonian

The electronic excitations in the PtX systems have been modeled using Peierls-Hubbard (PH) Hamiltonians [2,3,5,38-41]. These PH models have proven to be very useful in predicting the properties of localized excitations and identifying trends associated with the tunability in the PtX complexes. Unfortunately, these numerical calculations possess two significant limitations: the inability to determine uniquely all of the Hamiltonian parameters and the difficulties in obtaining solutions for the entire Hamiltonian. Interestingly, this leads to modeling with a

Hamiltonian in which select terms are set to zero, those terms being different in various studies. Due to these limitations, it is not possible to definitively determine the absolute values and detailed characteristics of the PtX materials from these models.

The conceptual underpinning of these models is the effects of electron-phonon and electron-electron interactions corresponding to the Peierls and Hubbard [42] terms, respectively. These models implement a mean field method (e.g., post-Hartree-Fock method [43] that includes electron correlations) applied to a more tractable form of the tight-binding Peierls-Hubbard Hamiltonian. Other simplifications include applying the Born-Oppenheimer approximation [32,44], where the total wavefunction is written as the product of the electronic and vibrational wavefunctions.

With respect to this dissertation, one of the more important PH studies was conducted by Alan Bishop and co-workers [2] where they predict the spatial extent of the self-trapped exciton, the importance of which is discussed in more detail below. The work of Alan Bishop and co-workers used a reduced Hamiltonian of the form:

$$H = \sum_{l,\sigma} \left\{ \left(-t_0 + \alpha\Delta_l\right)\left(c^{\dagger}_{l,\sigma}c_{l+1} + c^{\dagger}_{l+1,\sigma}c_{l,\sigma}\right) + \left[(-1)^l e_0 - \beta_l\left(\Delta_l + \Delta_{l-1}\right)\right] c^{\dagger}_{l,\sigma}c_{l,\sigma} \right\}$$

$$+ \frac{1}{2}K_{MX}\sum_l \Delta_l^2 + \frac{1}{2}K_{MM}\sum_l \left(\Delta_{2l} + \Delta_{2l+1}\right)^2$$

where the first summation is over ℓ,σ (i.e., an atom at site ℓ with spin σ) and the following two are over only ℓ. M stands for the metal ions and X the halide ions in the halogen-bridged mixed-valence transition-metal complexes considered (the bulk of the study [2] investigating PtX). The supertransfer energy (or hopping integral, t_0) represents the kinetic energy of the electronic charge transfer between ions. Other key parameters include the lattice distortion amplitude ($\Delta_\ell \equiv \hat{y}_{\ell+1} - \hat{y}_\ell$, where $\hat{y}_\ell$ are the displacements from uniform lattice spacing of the atom at site ℓ), the

electronic site energy (e_0), and the number operator ($c^{\dagger}_{\ell,\sigma}\ c_{\ell,\sigma}$, where $c^{\dagger}_{\ell,\sigma}$ creates and $c_{\ell,\sigma}$ annihilates an electron in the orbital at site ℓ). The effective spring terms ($K_{MX,}\ K_{MM}$) account for all other intrinsic interactions (i.e., core-electron repulsion, ligand-ligand interaction, etc.). Of key importance is the electron-phonon coupling (Peierls contribution) which is described by the hopping integral dependence on distance (α) and the on-site energy of the breathing mode of its neighbors along the chain (β_ℓ). This modeling has found that the strongest electron-phonon coupling arises from the breathing mode of the X ions coupling to the electronic density operator at the M site between the two X ions. A brief chronological synopsis of the PH modeling of the PtX systems is presented henceforth.

2.6.3 Peierls-Hubbard Modeling

Early models, like those of Dionys Baeriswyl and Alan Bishop [38], used approximations relevant to the strong coupling case limit (i.e., PtCl). The results of their calculations were consistent with some experimental observations of PtCl (e.g., resonant Raman effect and inter-valence absorption), though, could not reproduce other characteristics (e.g., observed luminescence). For example, their simplified PH model predicted no direct luminescence from the self-trapped exciton state even though a strong photoluminescence had been observed, as specifically discussed in the next section.

Further work using the PH model has found that after the exciton self-traps the system may decay non-radiatively into other species. The collection of works by Keiichiro Nasu et al. [39-41], and by Kaoru Iwano [45] showed that the decay channels are dependent on the electron-phonon coupling, the intra-, and inter-site Coulombic repulsion. An important result of this modeling shows that the PtX (CDW) systems in the final state of the charge transfer evolve into

the self-trapped exciton.

The comprehensive works by Alan Bishop and co-workers [2,3] predict a number of the important characteristic trends of the PtX(en) complexes including: electronic energy levels, optical absorption, photoinduced states, and the degree over which the induced states extend. In these studies the self-trapped exciton was referred to as a neutral bipolaron, which is sometimes referred to in the literature as a polarexciton or exciton-polaron.

Subsequent refinements in the modeling of the PtX chains by Alan Bishop and co-workers investigate replacing the harmonic spring constant between the metal and halide sites (used previously [2]) with an ion-ion repulsion force along with a term addressing the Coulomb attraction between the metal and halide sites [5]. These refinements attempt to incorporate the anharmonic effects at a more fundamental level to better address the more localized dynamics.

2.6.4 Predictions on Spatial Extent of the Self-Trapped Exciton

PH modeling predicts the trend in the extent of the localization of the self-trapped state. In the strong electron-phonon coupling case, the self-trapped exciton will be strongly localized and in the weak electron-phonon coupling case, it will be more delocalized. Moreover, the modeling predicts that for the PtCl(en) complex, the localization will be within a few unit cells of the chain structure [2] approaching the highly localized limit. The schematic structure of the CDW ground state (a) and the equilibrated self-trapped exciton in the highly localized limit (b) can be represented as:

(a) … -------X^----$Pt^{+(3+\delta)}$--- X^-------- $Pt^{+(3-\delta)}$------- X^----$Pt^{+(3+\delta)}$--- X^-------- $Pt^{+(3-\delta)}$…

(b) … -------X^----$Pt^{+(3+\delta)}$----- X^------- Pt^{+3}------ X^-------Pt^{+3}------ X^------- $Pt^{+(3-\delta)}$…

The PH modeling also predicts the spatial extent for the delocalized case of PtI(en). For the weak electron-phonon coupling case, the exciton is predicted to extend over more than 20 unit cells of the chain structure [2]. The prediction for the intermediately coupled PtBr(en) has a value between the two coupling limits, where it extends over 5 unit cells [2].

2.7 Observation of Self-Trapped Excitons in PtX

Initial evidence for self-trapped excitons in the PtX materials was reported in luminescence and Raman studies. The work by Wada et al. [46] observed a large photoluminescence Stokes-shift in the PtX chains. This large shift is not only an indicator of self-trapping but also an indicator of a strong electron-phonon coupling in these materials. Clark noted the evidence of strong electron-phonon coupling in PtX(en) seen in the resonant Raman scattering spectra of the PtX crystals [4]. The resonant Raman scattering spectra had a progression of the symmetric stretch extending to many overtones (in PtI(en) to the 9^{th}, in PtBr(en) to the 10^{th}, and in PtCl(en) to the 14^{th} at low temperature). Evidence for the electronic localization of defect states in PtX was observed by electron paramagnetic resonance studies [47]. These photoinduced defect states in PtX were found to extend over a limited number of unit cells, with the defect being more delocalized as X progresses from Cl, Br, to I. The photoinduced self-trapped state of the exciton is expected to show similar behavior as predicted by the PH modeling (discussed in the previous section).

A number of early time-resolved optical measurements were conducted on the PtX materials. Time-resolved photoluminescence studies with a resolution of 7 ps conducted by Tanino et al. measured the lifetime of the self-trapped exciton to be on the order of 100 ps [48]. Tanino et al. also put an upper limit of 7 ps on the barrierless transition from the free exciton to

the self-trapped state based on lifetimes of the luminescence and the resonant Raman lines [48]. Time-resolved photoluminescence studies conducted by Wada et al. [49] attribute a long term decay time of ~ 70 ps with the depopulation of the self-trapped exciton. Separate studies by Ooi et al. [50] and Kanner et al. [51] examined the transient absorption of PtBr and PtCl, respectively. These measurements assigned a redshifted induced absorbance signal to the self-trapped exciton state, having a lifetime of ~ 100 ps. Two important points can be drawn from these early time-resolved measurements. First, the photoinduced self-trapped exciton in the PtX complexes is found to be metastable, decaying on the order of ~ 100 ps. Second, the barrierless transition from the free to the self-trapped state occurs rapidly, where these early measurements had insufficient time resolution to observe the femtosecond formation dynamics.

More recent femtosecond impulsive excitation pump-probe measurements conducted by Aaron Van Pelt revealed the excited state lattice motion that leads to the self-trapped state in PtBr(en) [52,53]. Subsequent works use impulsive excitation to study exciton self-trapping in halide-bridged mixed-valence transition metal linear chains [54-56]. Excited state lattice motions were also observed via time-resolved photoluminescence [57,58]. The mechanism and the technique for observing the lattice dynamics associated with the self-trapping are reviewed in Chapter 3. The vibrationally impulsive time-resolved measurements on PtX presented in this dissertation have revealed additional dynamics associated with excitonic self-trapping, as discussed in subsequent chapters.

2.8 References for Chapter 2

1. Buschmann, W., S. McGrane, and A. Shreve, *Chemical tuning of nonlinearity leading to intrinsically localized modes in halide-bridged mixed-valence platinum materials.* Journal of Physical Chemistry A, 2003. **107**(40): pp. 8198-8207.

2. Gammel, J., A. Saxena, I. Batistic, A. Bishop, and S. Phillpot, *Two-band model for halogen bridged mixed-valence transition-metal complexes. I. Ground state and excitation spectrum.* Physical Review B, 1992. **45**(4): pp. 6408-6434.

3. Weber-Milbrodt, S., J. Gammel, A. Bishop, and E. Loh, Jr., *Two-band model for halogen-bridged mixed-valence transition-metal complexes. II. Electron-electron correlations and quantum phonons.* Physical Review B, 1992. **45**(12): pp. 6435-6458.

4. Clark, R., *Raman and resonance Raman spectroscopy of linear chain complexes,* in *Advances in infrared and Raman spectroscopy,* R. Clark and R. Hester, Editors. 1984, Wiley. pp. 95-132.

5. Scott, B., S. Love, G. Kanner, S. Johnson, M. Wilkerson, M. Berkey, B. Swanson, A. Saxena, X. Huang, and A. Bishop, *Control of selected physical properties of MX solids: an experimental and theoretical investigation.* Journal of Molecular Structure, 1995. **356**: pp. 207-229.

6. Huckett, S., R. Donohoe, L. Worl, A. Bulou, C. Burns, J. Laia, D. Carroll, and B. Swanson, *Mixed-halide MX chain solids: Effect of chloride doping on the crystal structure and resonance Raman spectra of* $[Pt(en)_2Br_2][Pt(en)_2](ClO_4)_4$. Chemistry of Materials, 1991. **3**: pp. 123-127.

7. Conradson, S., R. Dallinger, B. Swanson, R. Clark, and V. Croud, *Resonance Raman study of the* ν_1 *band structure of* $[Pt(en)_2Br_2][Pt(en)_2](ClO_4)_4$. Chemical Physics Letters, 1987. **135**(4,5): pp. 463-467.

8. Love, S., L. Worl, R. Donohoe, S. Huckett, and B. Swanson, *Origin of the fine structure in the vibrational spectrum of* $[Pt(C_2H_8N_2)_2][Pt(C_2H_8N_2)_2Cl_2](ClO_4)_4$*: Vibrational localization in a quasi-one-dimensional system.* Physical Review B, 1992. **46**(2): pp. 813-816; the before mentioned study discusses the origin of the fine structure in PtCl(en) due to isotope effects. The following study incorrectly applies the same reasoning to the observed fine structure of the Raman spectra in a chlorine contaminated PtBr(en) sample: Tanaka, M. and S. Kurita, *Fine structures of the resonant Raman spectra in quasi-one-dimensional crystals of halogen-bridged mixed-valence platinum compounds.* Journal of Physics C: Solid State Physics, 1986. **19**: pp. 3019-3028.

9. Huang, X., A. Saxena, A. Bishop, L. Worl, S. Love, and B. Swanson, *Segment length dependence of Raman frequency and optical properties in mixed-halide* $PtCl_xBr_{1-x}$ *chain solids.* Solid State Communications, 1992. **84**(10): pp. 957-961.

10. Huckett, S., R. Donohoe, L. Worl, A. Bulou, C. Burns, and B. Swanson, *On the origin of the resonance Raman ν_1 dispersion and fine structure of PtBr.* Synthetic Metals, 1991. **41-43**: pp. 2773-2776.

11. Brozik, J. B. Scott, and B. Swanson, *Synthetic control of intrinsic ground-state defects in a mixed valence quasi-one-dimensional Pt halide chain.* Inorganica Chimica Acta, 1999. **294**: pp. 275-280.

12. Buschmann, W., B. Scott, R. Donohoe, B. Swanson, and A. Shreve, *Synthetic control of defect content in $[Pt(en)_2Cl_2][Pt(en)_2](ClO_4)_4$.* Chemistry of Materials, *in preparation.*

13. Peierls, R., *Quantum Theory of Solids,* 1955, Oxford University Press. pp. 108-112.

14. Jahn, H., and E. Teller, *Stability of polyatomic molecules in degenerate electronic states. I. Orbital degeneracy.* Proceedings of the Royal Society of London. Series A, Mathematical and Physical Sciences, 1937. **161**(905): pp. 220-235.

15. Wada, Y., T. Mitani, M. Yamashita, and T. Koda, *Charge transfer exciton in halogen-bridged mixed-valent Pt and Pd complexes: Analysis based on the Peierls-Hubbard Model.* Journal of the Physical Society of Japan, 1985. **54**(8): pp. 3143-3153.

16. Yamashita, M., N. Matsumoto, and H. Kida, *Studies of mixed-valence complexes of platinum and palladium. IV. X-ray photoelectron spectra of some of the platinum complexes.* Inorganica Chimica Acta, 1978. **31**: pp. L381-L382.

17. Clark, R., V. Croud, R. Wills, P. Bates, H. Dawes and M. Hursthouse, *Mixed-valence linear-chain complexes: X-ray structural characterization of a $Pd^{II}/Pd^{IV}Br_2$ chain and of three mixed-metal chains, $[NiPt(en)_4Cl_2]^{4+}$, $[PdPt(pn)_4Cl_2]^{4+}$ and $[NiPt(pn)_4Cl_2]^{4+}$, all as perchlorate salt.* Acta Crystallographica Section B: Structural Science, 1989. **45**: pp.147-152.

18. S. Love, S. Huckett, L. Worl, T. Frankcom, S. Ekberg, and B. Swanson, *Far-infrared spectroscopy of halogen-bridged mixed-valence platinum-chain solids: Isotope-substitution studies.* Physical Review B, 1993. **47**(17): pp. 11107-11123.

19. Huckett, S., B. Scott, S. Love, R. Donohoe, C. Burns, E. Garcia, T. Frankcom, B. Swanson, *Effects of temperature on the crystal and molecular structure of the mixed-valence linear chain $[Pt(en)_2][Pt(en)_2X_2][ClO_4]_4$ (X = Cl, Br).* Inorganic Chemistry, 1993. **32**: pp. 2137-2144.

20. Kittel, C., *Introduction to solid state physics.* 1996, New York: John Wiley & Sons. chapter 11.

21. Ashcroft, N. and N. Mermin, *Solid State Physics*, 1976, Philadelphia: Saunders College. pp. 626-628.

22. Frenkel, J., *On the transformation of light into heat in solids I.* Physical Review, 1930. **37**: pp. 17-44; Frenkel, J., *On the transformation of light into heat in solids II.* Physical Review, 1931. **37**: pp. 1276-1294; exciton formation due to the absorption of light by solids was further discussed in Peierls's early work: Peierls, R., *Zur theorie der absorptionsspektren fester körper*. Annale der Physik (*The theory of the absorption spectra of solid bodies*. Annals of Physics), 1932. **13**(5): pp. 905-952.

23. Toyozawa, Y., *Electrons, Holes, and Excitons in Deformable Lattice* presented in *Relaxation of Elementary Excitations,* Springer Series in Solid-State Sciences. Volume 18, R. Kubo and E. Hanamura, Editors. 1980, Springer-Verlag. pp. 3-18.

24. Toyozawa, Y. and Y. Shinozuka, *Stability of an Electron in Deformable Lattice -- Force Range, Dimensionality and Potential Barrier --*. Journal of the Physical Society of Japan, 1980. **48**(2): pp. 472-478.

25. Shinozuka, Y. and N. Ishida, *Self-trapping of an exciton in quasi-low dimensional systems*. Journal of the Physical Society of Japan, 1995. **64**(8): pp. 3007-3017.

26. Iwano, K. and K. Nasu, *Theory for spectral shape of optical absorption in halogen-bridged mixed-valent metal complexes.* Journal of the Physical Society of Japan, 1992. **61**(4): pp. 1380-1389.

27. Schreiber, M. and Y. Toyozawa, *Numerical experiments on the absorption lineshape of the exciton under lattice vibrations. I. The overall lineshape.* Journal of the Physical Society of Japan, 1982. **51**(5): pp. 1528-1536.

28. Donohoe, R., R. Dyer, and B. Swanson, *The red and near-infrared resonance raman spectroscopy of photoinduced defects in the mixed-valence linear chain complexes* $[Pt^{II}(en)_2][Pt^{IV}(en)_2Cl_2][ClO_4]_4$. Solid State Communications, 1990. **73**(**7**): pp. 521-525.

29. Degiorgi, L., P. Wachter, M. Haruki, and S. Kurita, *Far-infrared optical investigations on quasi-one-dimensional halogen-bridged mixed-valence compounds.* Physical Review B, 1989. **40**(5): pp. 3285-3293.

30. Love, S., S. Huckett, L. Wori, T. Frankcom, S. Ekberg, and B. Swanson, *Far-infrared spectroscopy of halogen-bridged mixed-valence platinum-chain solids: isotope-substitiution studies.* Physical Review B, 1993. **47**(17): pp. 11 107-11 123.

31. Raman, C., K. Krishnan, *A new type of secondary radiation.* Nature, 1928. **121**: pp. 501-502; Raman, C., *A change of wave-length in light scattering.* Nature, 1928. **121**: page 619.

32. McHale, J., *Molecular spectroscopy.* 1999, Upper Saddle River: Prentice-Hall.

33. Landau, L., *Briefe, vorläufige Mitteilungen und Diskussionen: Über die bewegung der elektronen im kristallgitter*. Physikalische Zeitschrift der Sowjetunion (*Letter, Preliminary Notices and Discussion: About the motion of electrons in a crystal lattice*. Physical Journal of the Soviet Union), 1933. **3**: pp. 664-665; Landau predicated two methodologies for the modeling of the prognosticated electronic self-trapping (which he refers to as "(the electron's) location to stick to"; "(Elektron) Stelle zu haften"). One involves separately the free electron and the lattice (where he considers diamond) and the other accounts for a slightly perturbed lattice spatially (for sodium chloride).

34. Song, K. and R. Williams, *Self-Trapped Excitons*, Springer Series in Solid-State Sciences. Volume 105. 1996, New York: Springer.

35. Ueta, M., H. Kanzaki, K. Kobayashi, Y. Toyozawa, and E. Hanamura, *Excitonic Processes in Solids*, Springer Series in Solid-State Sciences. Vol. 60. 1986, New York: Springer.

36. Cohen-Tannoudji, C., B. Diu, and F. Laloe, *Quantum Mechanics, Volume One*, 1977, New York: Wiley-Interscience Publication. pp. 74-77.

37. Emin, D. and T. Holstein, *Adiabatic theory of an electron in a deformable continuum.* Physical Review Letters, 1976. **36**(6): pp. 323-326.

38. Baeriswyl, D. and A. Bishop, *Halogen-Bridged Metal Compounds for High-T_C Superconductors?* Physica Scripta, 1987. **T19**: pp. 239-245; Baeriswyl, D. and A. Bishop, *Localized polaronic states in mixed-valence linear chain complexes.* Journal of Physics C: Solid State Physics, 1988. **21**: pp. 339-356.

39. Mishima, A. and K. Nasu, *Nonlinear lattice relaxation of photogenerated charge-transfer excitation in halogen-bridged mixed-valence metal complexes. I. Soliton and self-trapped exciton.* Physical Review B, 1989. **39**(9): pp. 5758-5762.

40. Mishima, A. and K. Nasu, *Nonlinear lattice relaxation of photogenerated charge-transfer excitation in halogen-bridged mixed-valence metal complexes. II. Polaron channel.* Physical Review B, 1989. **39**(9): pp. 5763-5766.

41. Suzuki, M. and K. Nasu, *Nonlinear lattice-relaxation process of excitons in quasi-one-dimensional halogen-bridged mixed-valence metal complexes: Self-trapping, solitons, and polarons.* Physical Review B, 1992. **45**(4): pp. 1605-1611; for an extensive compilation of related articles by Nasu see the Journal of the Physical Society of Japan.

42. Hubbard, J., *Electron correlations in narrow energy bands*. Proceedings of the Royal Society of London. Series A, Mathematical and Physical Sciences, 1963. **276**: 238-257.

43. Hartree, D., *The wave mechanics of an atom with a non-Coulomb central field. Part II. Some results and discussion*. Proceedings of the Cambridge Philosophical Society, 1928. **24**: pp. 111-132; Fock, V., *Naherungsmethode zur Losung des quantenmechanischen Mehrkorperproblems.* Zeitschrift fur Physik (*Approximate method for solution of quantum many body problem.* Journal of Physics) 1930. **61**: pp. 126-148; Fock, V., *Self-consistent field mit Austausch fur Natrium.* Zeitschrift fur Physik (*Self-consistent field with exchange for Sodium.* Journal of Physics) 1930. **62**: pp. 795-805; both Hartee and Fock (first and second reference, respectively) arrived at the same set of equations (non-linear set of integro-differential equations of single electron functions) to evaluate the potential energy and hence, reduce the many-electron problem to a manageable single electron problem (obtaining a solution to Schrödinger equation). Each arrived at these equations using two different methods: Hartee applied the method of successive approximations while Fock used the variational principle. Fock's improvement over Hartree involves selecting a wavefunction (with the correct symmetry properties) that takes into account the antisymmetry of the complete (fermion) function, resulted in a self-consistent field.

44. Eckart, C., *The kinetic energy of polyatomic molecules.* Physical Review, 1934. **46**(5): pp. 383-387; Born, M. and R. Oppenheimer, *Zur Quantentheorie der Molekeln,* Annalen der Physik (On the Quantum Theory of Molecules, Annuals of Physics), 1927. **84**: pp. 457-484.

45. Iwano, K., *Relaxation processes yielding nonlinear excitations in the extended Peierls-Hubbard model for photoexcited MX chains.* Journal of the Physical Society of Japan, 1997. **66**(4): pp. 1088-1096.

46. Wada, Y., K. Era, and M. Yamashita, *Luminescence lifetimes in halogen bridged mixed valence metal complexes.* Solid State Communications, 1988. **67**(10): pp. 953-956.

47. Donohoe, R., L. Worl, C. Arrington, A. Bulou, and B. Swanson, *Photoinduced defects in the bromide-bridged platinum linear chain $[Pt(en)_2][Pt(en)_2Br_2](ClO_4)_4$ (with en = ethylenediamine).* Physical Review B, 1992. **45**(23): pp. 13185-13195.

48. Tanino, H., W. Rühle, and K. Takahashi, *Time-resolved photoluminescence study of excitonic relaxation in one-dimensional systems.* Physical Review B, 1988. **38**(17): pp. 12 716- 12 718.

49. Wada, Y., U. Lemmer, E. Gobel, and M. Yamashita, *Time-resolved luminescence study of self-trapped exciton relaxation in ordered and disordered one-dimensional MX-chain systems.* Journal of Luminescence, 1994. **58**: 146-148.

50. Ooi, H., M. Yamashita, and T. Kobayashi, *Ultrafast Optical Response in a Quasi-one-dimensional Halogen-Bridged Mixed-Valence Complex $[Pt(en)_2][PtBr_2(en)_2](ClO_4)_4$.* Solid State Communications, 1993. **86**(12): pp. 789-793

51. Kanner, G., G. Strouse, B. Swanson, M. Sinclair, J. Jiang, and N. Peyghambarian, *Subpicosecond dynamics of excitons and photoexcited intrinsic polarons in the quasi-one-dimensional solid PtCl.* Physical Review B, 1997. **56**(5): pp. 2501-2509.

52. Dexheimer, S., A. Van Pelt, J. Brozik, and B. Swanson, *Femtosecond vibrational dynamics of self-trapping in a quasi-one-dimensional system.* Physical Review Letters, 2000. **84**(19): pp. 4425-4428.

53. Dexheimer, S., A. Van Pelt, J. Brozik, and B. Swanson, *Ultrafast vibrational dynamics in a quasi-one-dimensional system: Femtosecond impulsive excitation of the PtBr(en) mixed-valence linear chain complex.* Journal of Physical Chemistry A, 2000. **104**(18): pp. 4308-4313.

54. Van Pelt, A. and S. Dexheimer, *Ultrafast dynamics of excitonic self-trapping* in Ultrafast Phenomena XII, T. Elsaesser, S. Mukamel, M. Murnane, N. Scherer, Editors. 2000, Springer-Verlag. pp. 393-397.

55. Sugita, A, T. Saito, H. Kano, M. Yamashita, and T. Kobayashi, *Wave packet dynamics in a quasi-one-dimensional metal-halogen complex studied by ultrafast time-resolved spectroscopy.* Physical Review Letters, 2001. **86**(10): pp. 2158-2161.

56. Wada, Y., N. Matsushita, and H. Haneda, *Ultrafast dynamics of lattice relaxed states in quasi-one-dimensional MX-chain compounds.* . Journal of Luminescence, 2004. **108**: pp. 285-289.

57. Tomimoto, S., S. Saito, T. Suemoto, K. Sakata, J. Takeda, and S. Kurita, *Observation of the wave-packet oscillation during the exciton self-trapping process in a quasi-one-dimensional halogen-bridged Pt complex.* Physical Review B, 1999. **60**(11): pp. 7961- 7965.

58. Tomimoto, S., S. Saito, T. Suemoto, J. Takeda, and S. Kurita., *Ultrafast dynamics of lattice relaxation of excitons in quasi-one-dimensional halogen-bridged platinum complexes.* Physical Review B, 2002. **66**(15): pp. 155112-155121.

Chapter 3

Experimental Methods

3.1 Transient Optical Absorption Spectroscopy

The pump-probe technique [1] uses a pump pulse that excites the sample followed by a probe pulse, which measures the change in the optical properties due to the pump. The change in the optical transmission due to pump excitation of the sample (ΔT) is measured by modulating the pump beam with a mechanical chopper and measuring the resulting modulation of the transmitted probe intensity using a lock-in amplifier [2]. This signal is divided by the total transmission of the probe beam through the sample without the pump and is referred to as the differential transmittance ($\Delta T / T$) [3]. For a small change in transmittance, $\Delta T / T$ is proportional to the change in absorbance. The time evolution of the differential transmittance is resolved by varying the time delay between the pump and probe pulse.

Figure 3.1 shows a simplified schematic of the apparatus used to carry out the pump-probe measurements. In the optical setup, the pump and the probe beams are focused to the same spot on the sample. The path length difference between the pump and the probe beam is varied using a computer controlled translation stage. With the pump path length fixed, the path length of the probe arm is varied resulting in a relative change in length that corresponds to the delay time. Zero delay time is the case where the pump and probe pulse arrive at the sample at the same time having both traversed the same path length. Positive time delay means that the probe arrives at the sample after the pump pulse, where the probe pulse travels over a longer path length than the pump. A change of 0.3 μm in path length of the probe arm relative to the pump corresponds to a one femtosecond change in delay time.

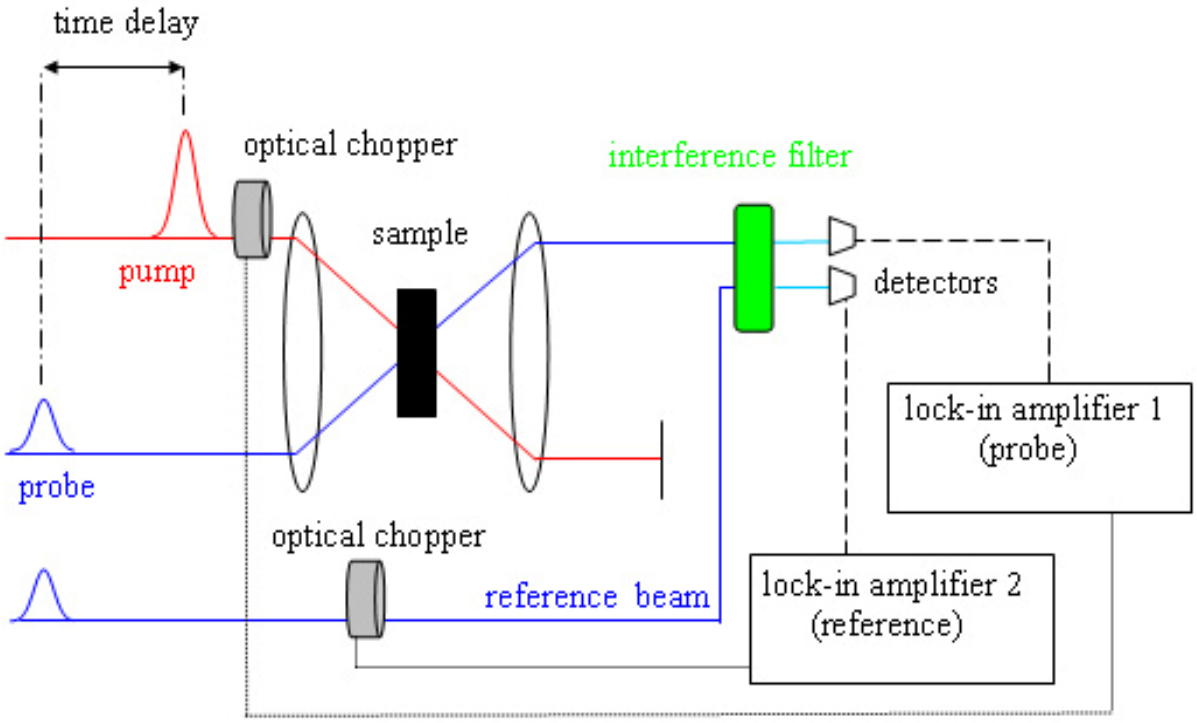

Figure 3.1: A simplified schematic of the apparatus used to carry out the pump-probe technique.

The remainder of this section will address several key issues: (3.1.1) the distinction between degenerate and nondegenerate pump-probe techniques, (3.1.2) generation of a reference beam (shown in Figure 3.1) and its use for noise reduction and normalization, discussion of (3.1.3) hardware and (3.1.4) software used, (3.1.5) pulse characterization, and (3.1.6) pulse compression.

3.1.1 Degenerate and Nondegenerate Pump-Probe Techniques

In degenerate pump-probe measurements, the pump and probe pulses are derived from the same pulse by using a beamsplitter. The pump pulse passes through the beamsplitter and has a much greater intensity than the probe pulse, which reflects off of the beamsplitter. To ensure that the probe pulse affects the sample negligibly, the intensity of the probe pulse is set to a value at least five times less than the pump pulse intensity. The beamsplitters used in this study had reflectivities of 10% and 20%. To account for the added dispersion seen by the pump pulse after passing through the beamsplitter, a "matched" compensation plate (being composed of the same material and thickness) was added to the probe line.

In the nondegenerate (or two-color) pump-probe measurements presented in Chapters 4 and 6, the probe pulse is derived from a femtosecond white light continuum [4], which is generated by focusing a portion of the amplifier beam into a 2 mm sapphire plate. The spectral broadening of the pulse is due to self-phase modulation [5], which is the process where the phase of an optical pulse changes due to the nonlinear intensity dependence of the index of refraction of the material it passes through. This change in the index results in higher frequencies in the trailing edge of the pulse and lower frequencies in the leading edge.

To measure the transient absorption spectrum, the probe beam is wavelength resolved after transmission through the sample using either interference filters or a monochromator. Wavelength-resolved pump-probe measurements have uncovered spectroscopic signatures of excitonic self-trapping in PtX(en), discussed in Chapter 4.

The pump-probe apparatus (a photograph shown in Figure 3.2) can be configured for either degenerate or nondegenerate measurements. A separate apparatus was constructed to allow excitation of the sample with multiple pump pulses for the experiments discussed in Chapter 5. Details of the multiple pulse pump-probe apparatus are provided in Section 5.1.

Control of the pump and probe beam intensities was achieved using neutral density filters and pairs of Newport Polarcor™ absorptive linear polarizers, composed of borosilicate glass with aligned silver particles. The second Polarcor™ polarizer, generally called an analyzer, was oriented to ensure that the polarization of the light into the optical apparatus remained horizontal to ensure optimal excitation of the PtX complexes (see Section 2.4). The transmitted intensity is varied by rotating the orientation of the first polarizer. For the ideal case of zero absorption,

$$I(\theta) = I_0 \cos^2 \theta \tag{3.1}$$

where I(θ) is the transmitted intensity through the polarizer pair, I_0 is the incident intensity into the polarizer pair, and θ is the difference in the orientation of the transmission axes between the two polarizers [6]. When θ = 0º the polarizers have the same orientation resulting in maximum transmission while for θ = 90º the polarizers are crossed and the intensity is zero.

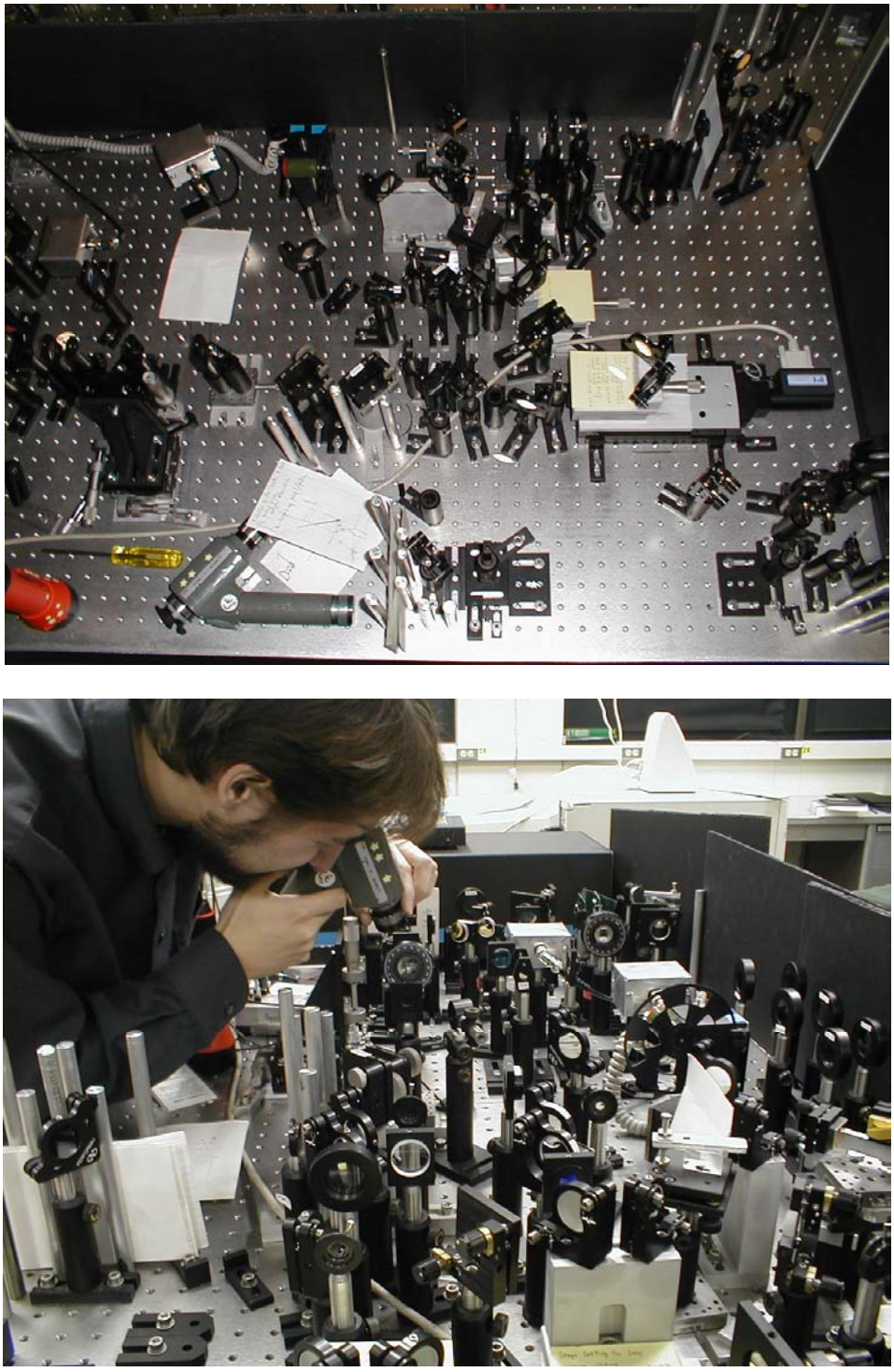

Figure 3.2: The pump-probe apparatus used to investigate the vibrational dynamics associated with excitonic self-trapping.

3.1.2 Reference Beam

A reference beam is obtained by extracting a small portion of continuum probe pulse using a beamsplitter that is set up just prior to the pump-probe apparatus. Just before detection, the probe and reference beams are propagated parallel to one another and are vertically displaced. Both beams pass through either an interference filter or a monochromator. This beam arrangement ensures that the probe and reference line are monitoring the same portion of the continuum.

Noise variations in the continuum probe intensity can be corrected for using the reference beam. The reference beam normalizes ΔT by the value of the total transmission of the probe without pump interaction (T). The reference line intensity is set to the value of the probe intensity after transmission through the sample in absence of the pump. The reference line intensity is varied using a pair of linear variable metallic neutral density filters. The second variable filter is introduced in the reference line in a mirror image configuration so as not to produce a gradient in the intensity distribution. A reference beam is also used to monitor the noncollinear and collinear optical parametric amplifiers discussed in Section 3.2.2.

3.1.3 Detection Electronics and Hardware

The optical setup was configured with one of two sets of EG&G photodiodes. For the measurement of $\Delta T / T$ at probe wavelengths ranging from the visible to 1 μm, as was the case in Chapters 4 and 6, the C300808E N-type Si PIN photodiodes were used. For the measurement of $\Delta T / T$ beyond 1 μm, as was the case in Chapter 5, the C30642G InGaAs PIN photodiodes were used. The Si and InGaAs photodiodes were linear to 1 mV and 6 mV, respectively. The photodiodes were kept in the linear range by attenuating the light just before the detector using

metallic neutral density filters.

Measurement of $\Delta T / T$ was obtained by phase sensitive detection [2] using two Stanford Research Systems Model SR830 DSP Lock-In Amplifiers. One lock-in amplifier measures the change in transmission (ΔT) signal while the other measures the transmission (T) signal. These signals were obtained from the photodiodes monitoring the probe and reference line, respectively. Phase sensitive detection selects out a particular component of the signal at a specific reference frequency and phase. Frequency components away from the reference, even if thousands of times larger, are rejected allowing for the detection of very small AC signals. The reference signal input derived from the chopper driver had a frequency of between 100 and 110 Hz and was set to trigger on the positive edge. The photodiodes were connected to the A input of the lock-in having a 10 MΩ, 25 pF input impedance. Ground signal input mode was selected providing a 10 Ω isolation of the connector shields from the chassis. The input was AC coupled, which acts as a high pass filter, passing signals above 160 mHz. The Notch filters, having a width of 10 Hz, were used to attenuate signals at the line frequency (60 Hz) and its harmonic (120 Hz). The reserve mode was set to Normal to ensure the 120 dB actual dynamic reserve value ceiling was not exceeded in the lowest sensitivity range used (1 μV). Low Noise reserve mode was not used since it often provided insufficient sensitivity at the low end of the range resulting in signal digitization. The lock-in was typically set to a time constant of 100 ms. The output mode was X which is the output of the phase sensitive detector (i.e., the component in phase with the chopper reference signal).

Prior to the measurements, the reference phase shift was adjusted so that the measured signal phase was 0º. The lock-in implements this by subtracting the present measured value of θ from the reference phase shift. In the experiment, this is executed by chopping the pump beam at

the reference frequency while blocking the probe beam and pressing the Auto Phase button; thereby setting the phase to the scattered pump light. The probe and reference beams were monitored on general purpose interface bus (GPIB) addresses 8 and 9, respectively.

3.1.4 Data Acquisition Program

An overview of the procedure for data acquisition is as follows. The program, written in National Instruments™ LabVIEW executes five steps. (1) The program moves the translation stage to the starting position at negative time delay. (2) $\Delta T / T$ is plotted on screen and recorded in an ascii file. (3) The stage is moved to the next delay time. (4) Steps 2 and 3 are repeated until the translation stage reaches the end of the scan range. (5) If signal averaging is implemented, steps 1 through 4 are repeated for n number of scans.

(Steps 1 and 2) After moving the Physik Instrumente high precision translation stage to a particular delay time, the program acquires the values of both the lock-in voltage from a photodiode monitoring the intensity of the transmitted probe beam and a second lock-in voltage from a photodiode monitoring the intensity of the reference line. The two channels are acquired separately, using two lock-in amplifiers, and transmitted to a file via GPIB 24 pin (IEEE-488) bus along with the corresponding delay time and calculated values discussed below. The dwell time of the program at a particular delay time position was set to 200 ms.

(Step 3) The program then moves the translation stage to the next delay time based on the input value for the step size. High resolution measurements had step sizes of either 8 or 10 fs. Variations of the programs allowed for regions of different step sizes in delay space and the flexibility of using an input file for variable delay steps (e.g., logarithmic). Larger step sizes were taken in regions that did not require high resolution.

(Steps 4 and 5) The program steps though a number of delay times, acquiring ΔT / T at each point. This is analogous to capturing the time evolution of a horse's gallop depicted in a series of photos in Figure 3.3. The program repeats the scan sequence n number of times for the purpose of signal averaging. Real-time plotting of the intensity of the transmitted probe beam divided by the reference line allows for monitoring during acquisition. The program plots the current scan and the current average of the scans during acquisition.

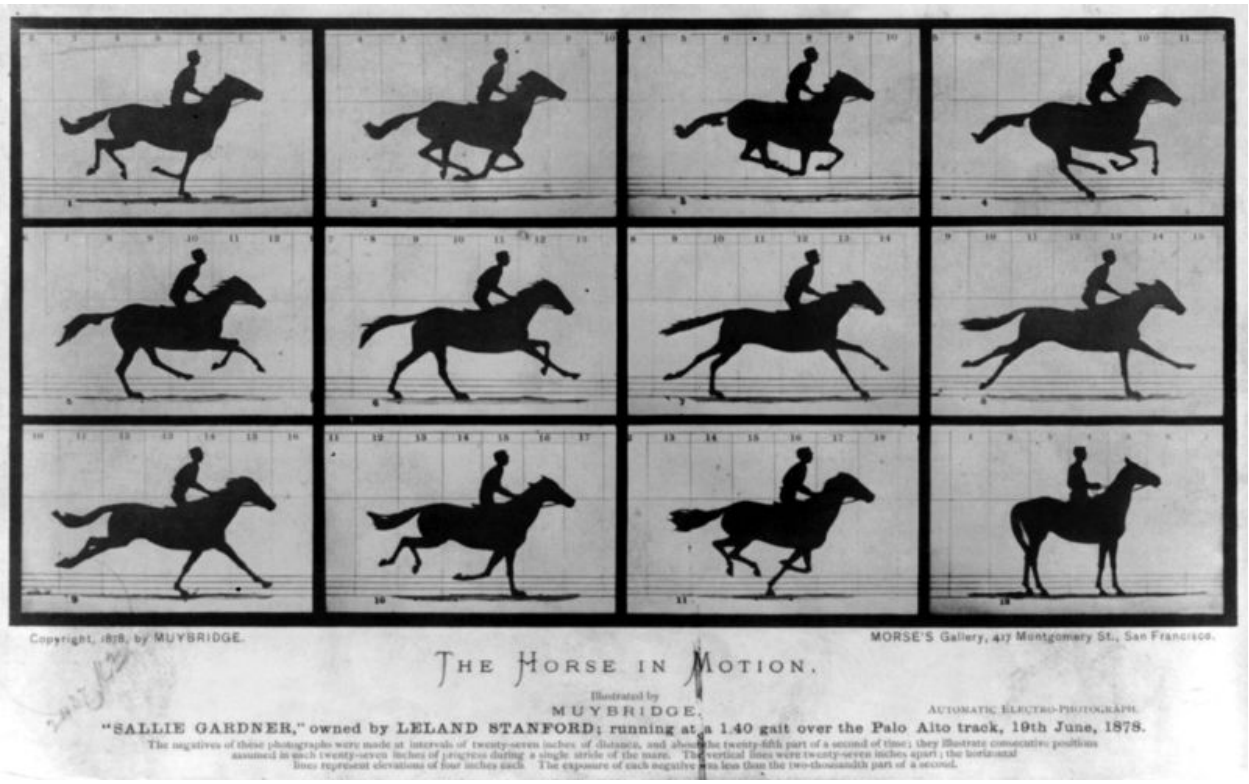

Figure 3.3: The Horse in Motion by Eadweard Muybridge. "Sallie Gardner," owned by Leland Stanford; runnng at a 1:40 gait over the Palo Alto track, 19th June 1878 (obtained from the United State Library of Congress Prints and Pictures division under digital ID cph.3a45870).

3.1.5 Pulse Characterization

The pulses out of the amplifier were characterized by an intensity autocorrelation [1,7] where the pump and probe pulses were focused into a CASIX high grade Czochralski grown 50 μm thick β-Barium Borate (BBO) crystal [8] (with a hygroscopic protective coating) cut for phase matching of 800 nm light. The mixing of the pump and probe pulse (centered at 800 nm) in the nonlinear crystal results in a second harmonic signal [9] (centered at 400 nm):

$$S(\tau) \propto \int I'(t) I(t-\tau) dt \tag{3.2}$$

where the measurement of the first order correlation function [S(τ)] is the time overlap of the "known" function I′(t) with the varied function I(t - τ). Since the test function (of known pulse width) can not be synthesized, the pulse in question is its own test function; hence, *auto*correlation. Using the degenerate pump-probe setup described above, I′(t) is the pump pulse intensity and I(t - τ) is the time varying probe pulse intensity. Assuming the optical pulse has the shape of a $\text{sech}^2(t)$ function, the autocorrelation full width half maximum (FWHM) is divided by 1.543, which is the hyperbolic secant-squared ($\text{sech}^2(t)$) pulse profile function fitting parameter [3], to determine its "actual" temporal FWHM. A typical autocorrelation is shown in Figure 3.4.

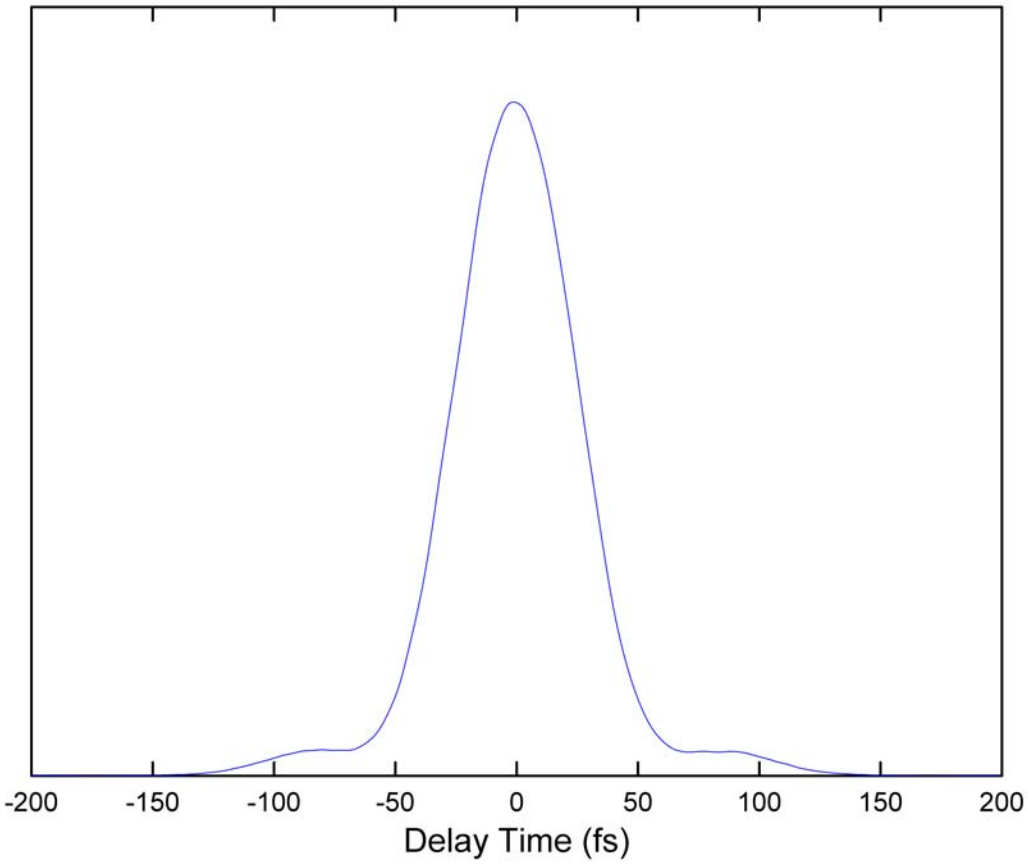

Figure 3.4: An autocorrelation of a 35 fs pulse out of the amplifier detailed in Section 3.2.1. The measurement was taken using a BBO crystal.

The bandwidth of the pulse and its duration are related by the uncertainty principle through a Fourier transform. For the case where the dispersion is zero (i.e., a pulse with a constant phase across its component frequencies), the pulse is referred to as transform-limited and is constrained by a duration-bandwidth minimum:

$$\Delta v \ \Delta t = C \tag{3.3}$$

where $\Delta\upsilon$ is the bandwidth, Δt is the pulse duration, and C is a constant. Assuming a $\mathrm{sech}^2(t)$ pulse intensity profile, the constant becomes 0.315 [3]. In terms of the wavelength,

$$\left|\Delta t\right| = 0.315 \left(\frac{c}{\lambda_0^2}\right)\Delta\lambda \tag{3.4}$$

where λ_0 is the central wavelength, $\Delta\lambda$ is the bandwidth, and c is the speed of light in vacuum. This follows from the relation:

$$c = v \ \lambda \tag{3.5}$$

where υ is the frequency and λ is the wavelength. The values of the spectral bandwidth and pulse duration are determined from the FWHM. Typically, the spectrum of the amplifier has a FWHM of 28 nm as shown in Figure 3.5. Figure 3.4 shows the pulse derived from this spectrum, which had a width of 35 fs and is close to transform-limited.

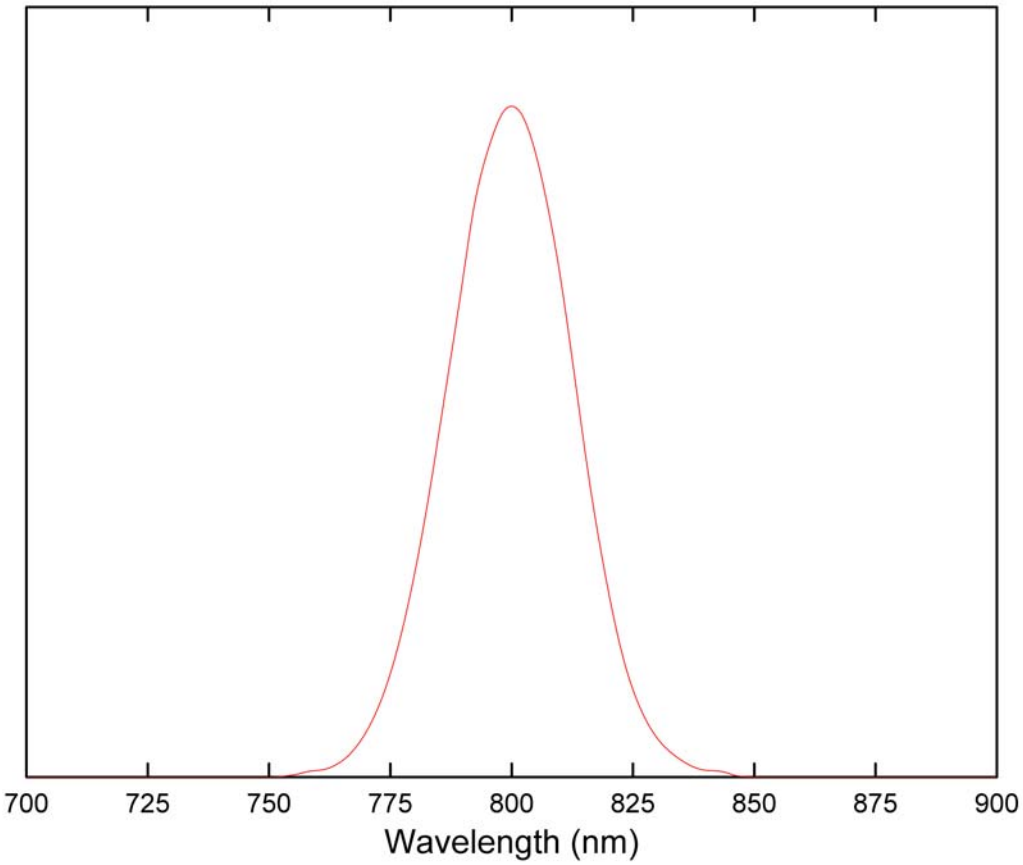

Figure 3.5: The spectrum of a 35 fs pulse out of the amplifier shown in Figure 3.4 and detailed in Section 3.2.1. The amplifier spectrum is centered at 800 nm and has a FWHM of 28 nm.

The continuum probe pulse is characterized by a cross-correlation [3], which is analogous to an autocorrelation. In the cross-correlation, the "known" test function is the 800 nm pump pulse determined from the autocorrelation. The pump pulse and the continuum probe are mixed in a BBO crystal and the signal is detected at the sum of the input frequencies selected by a monochromator. From energy conservation,

$$\omega_{pu} + \omega_{pr} = \omega_{cc} \tag{3.6}$$

where ω_{pu} is the pump frequency ($\propto$ 1 / 800 nm), ω_{pr} is the continuum probe frequency of interest, and ω_{cc} is the resulting summed frequency. Figure 3.6 shows the cross-correlations over the wavelength range of 1250 nm to 1350 nm after pulse compression (discussed below) was optimized for minimal pulse chirp.

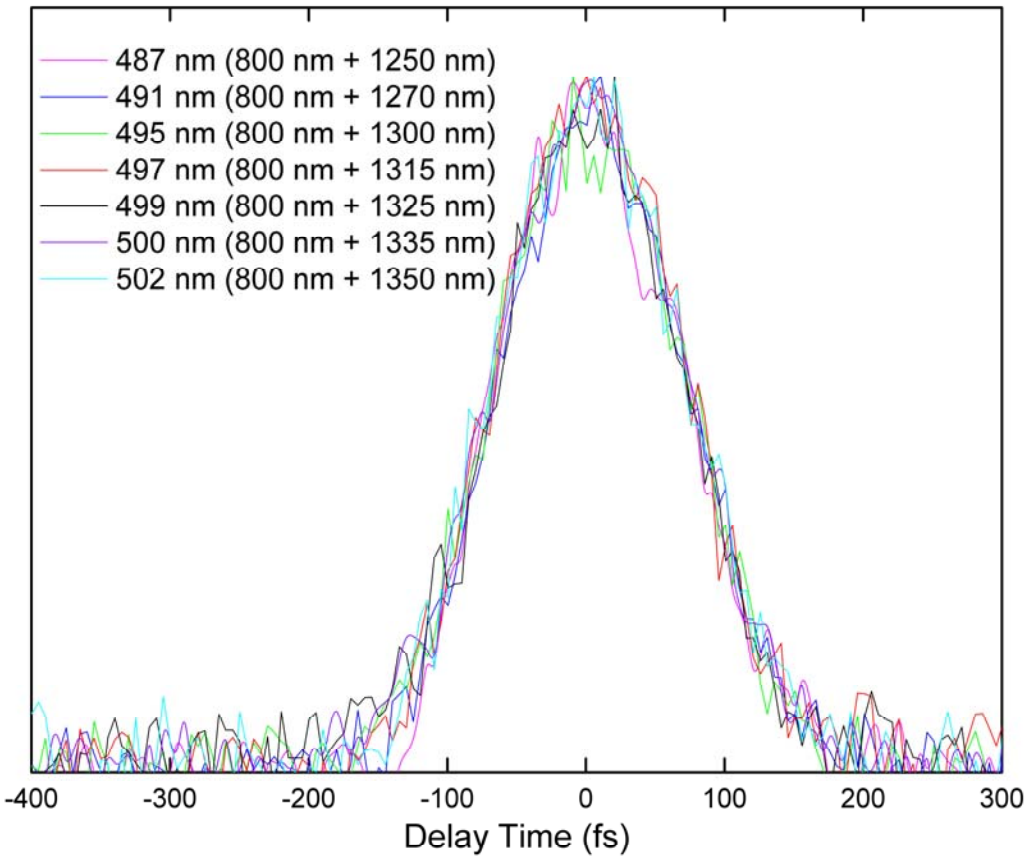

Figure 3.6: Cross-correlations after optimization of the prism compression. Shown are the cross-correlations of the amplifier pump pulse, having a pulse duration of ~ 110 fs centered at 800 nm, and the output of the optical parametric amplifier, having a pulse duration of ~ 45 fs centered at 1.31 μm. The systems these pulses are derived from are discussed in more detail in Section 3.2.2.

3.1.6 Pulse Compression

The measurements presented in this dissertation required that the continuum pulse be compressed in order to have the needed time resolution to observe wavepacket motion discussed in Section 3.3. There are two reasons that the uncompressed continuum pulse duration is insufficiently short. The white light continuum generation process results in a pulse duration longer than the amplifier pulse, and significant dispersion is experienced by the broadband white light continuum pulse as it travels through the optical components in the pump-probe apparatus. From the white light continuum, the near-infrared portion of the spectrum was selected for the probe since it overlaps the exciton absorption in the PtBr(en) and PtI(en) materials.

Compression of the near-infrared portion of the white light continuum (shown in Figure 3.7) is accomplished with a dispersive delay line constructed from a pair of fused silica prisms, in which higher frequency components of the continuum pulse are given shorter path lengths [10]. The prism pair, illustrated in Figure 3.8, introduces negative group velocity dispersion, which is defined as the negative of the second derivative of the phase with respect to the frequency. An increase in the prism separation increases the amount of negative group velocity dispersion seen by the continuum pulse. This compensates for the positive second-order dispersion the pulse experiences when traveling through optical components.

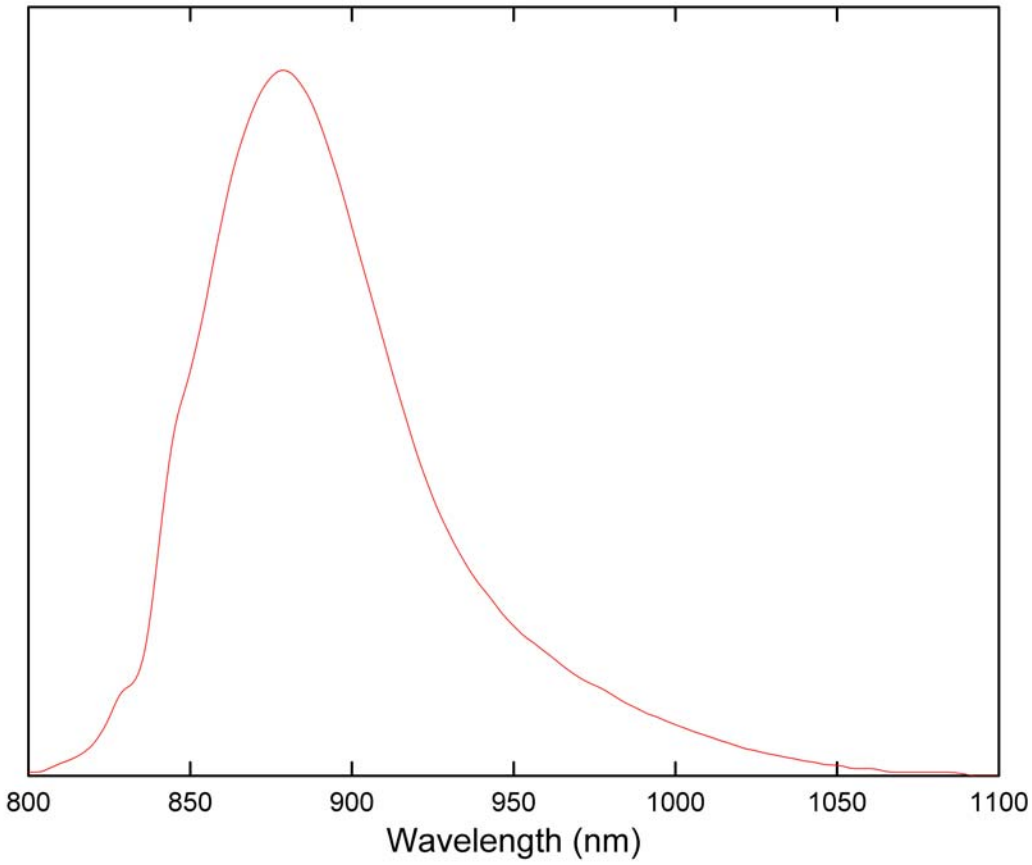

Figure 3.7: The near-infrared portion of a white light spectrum generated in a 2 mm thick sapphire plate pump at 800 nm with 35 fs pulse. The continuum pulse first passed through an 850 nm long pass filter to remove the residual pump pulse energy before characterization using a monochromator.

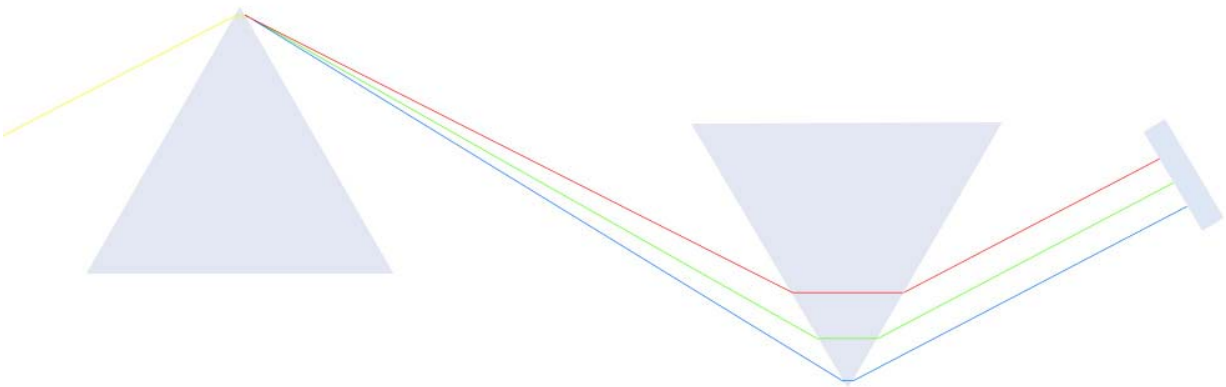

Figure 3.8: Prism pair used as phase dispersive elements to cause wavelength-dependent optical path lengths. The prismatic compression system uses two Brewster-cut prisms set to minimum deviation along with a mirror that sends the spatially chirped beam back through the prism pair. The prism pair introduces negative group velocity dispersion since the shorter wavelength components traverse the prism sequence in a shorter time than the longer wavelength components.

The prism compression is not ideal since it only corrects for second order dispersion and not higher orders. The very act of implementing prism compression increases the amount of third order dispersion. Second and third order dispersion, introduced by a prismatic pulse compressor, is proportional to the prism separation distance [10]. For typical prism glass, when the prism separation is optimized for zero second order dispersion, the third order dispersion will be non-zero. The magnitude of the third order term is strongly dependent on the selection of the prism material [11].

The prisms can also be used to spectrally select the near-infrared portion of the continuum by passing the beam through the first fused silica prism (which spatially disperses the wavelength components) and positioning the second prism to only capture the near-infrared portion. A mirror just after the second prism reflects the pulse back through the prisms to spatially reconstruct the beam profile. Specific parts of the near-infrared portion of the spectrum were selected using long pass filters with a cutoff frequency at either 850 nm or 900 nm.

A prism sequence was also used to compress pulses generated by an optical parametric amplifier (OPA), as discussed in Section 3.2.2. An example is shown in Figure 3.9, which shows the compression of an OPA signal pulse at 1.35 μm.

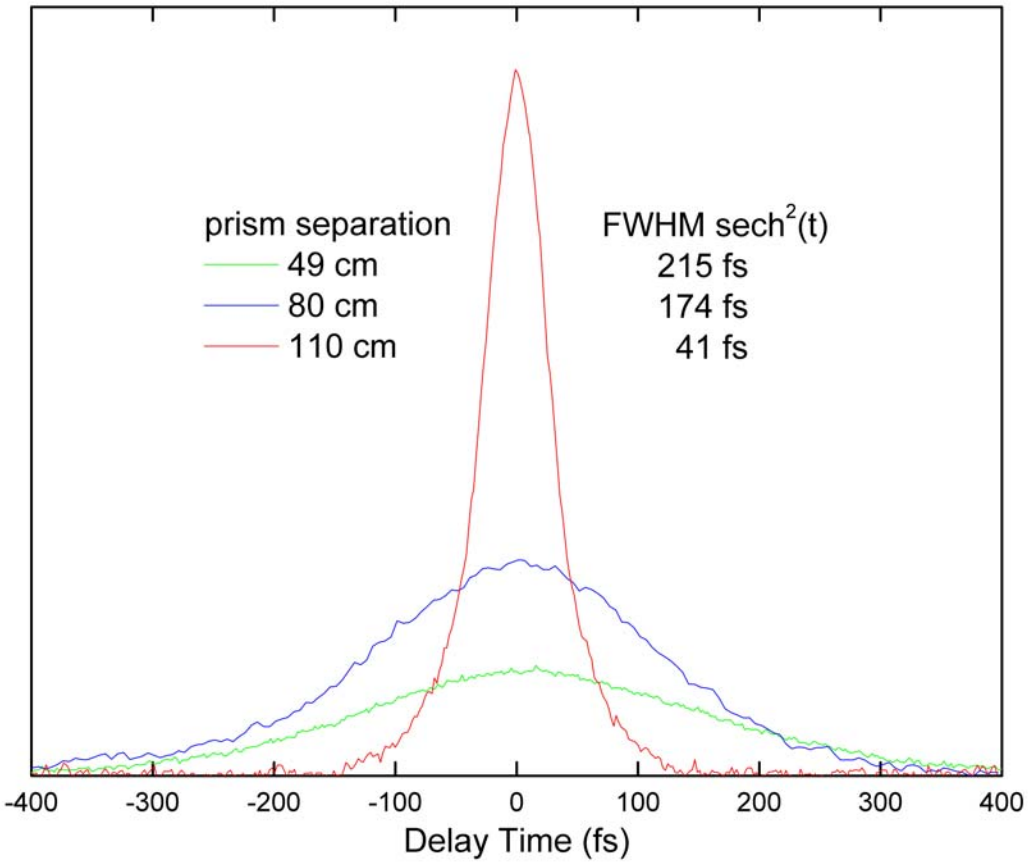

Figure 3.9: The output of an optical parametric amplifier tuned to 1.35 μm was frequency doubled in a BBO crystal resulting in 675 nm light having a spectral FWHM of 26 nm. The figure shows the degree of dispersion compensation by adjusting the prism separation.

3.2 Laser Instrumentation

This study was conducted using two separate laser systems. Both laser systems are composed of an oscillator, which generates spectrally broad femtosecond pulses, and an amplifier, which increases the pulse intensity while reducing the repetition rate of the pulse train.

In the oscillators, a continuous wave (CW) laser pumps a Ti:sapphire crystal [8]. In this material, a small percentage of the aluminum ions are replaced by titanium ions, which are responsible for the lasing. The titanium ions introduced into sapphire have their electronic ground state split into a pair of vibronically broadened levels, resulting in a large gain bandwidth and a broad emission band [12].

The oscillators operate in the pulsed regime due to mode-locking [13], which is the condition where a number of optical modes have the same phase at one point in the resonator which leads to constructive interference. Over time the modes at all other points in the cavity have randomly distributed phases which destructively interfere. As time evolves, the optical pulse, which comprises the point of common phase, moves throughout the cavity, resulting in a repetition rate of twice the cavity length divided by the speed of light.

The amplifiers are based on the chirped pulse amplification (CPA) architecture [14]. Briefly, CPA involves a three step process depicted in Figure 3.10. (1) A “high” intensity spectrally broad optical pulse is temporally stretched using a diffraction grating resulting in a linear frequency-chirp where the longer component wavelengths experience a shorter component path length. (2) The “low” intensity stretched pulse is then safely amplified in a Ti:sapphire crystal using regenerative amplification. A Pockels cell and polarizing optics provide the mechanism for switching a pulse into and out of the amplifier cavity. (3) The amplified pulse is recompressed by introducing the reverse of the frequency dependent path length difference

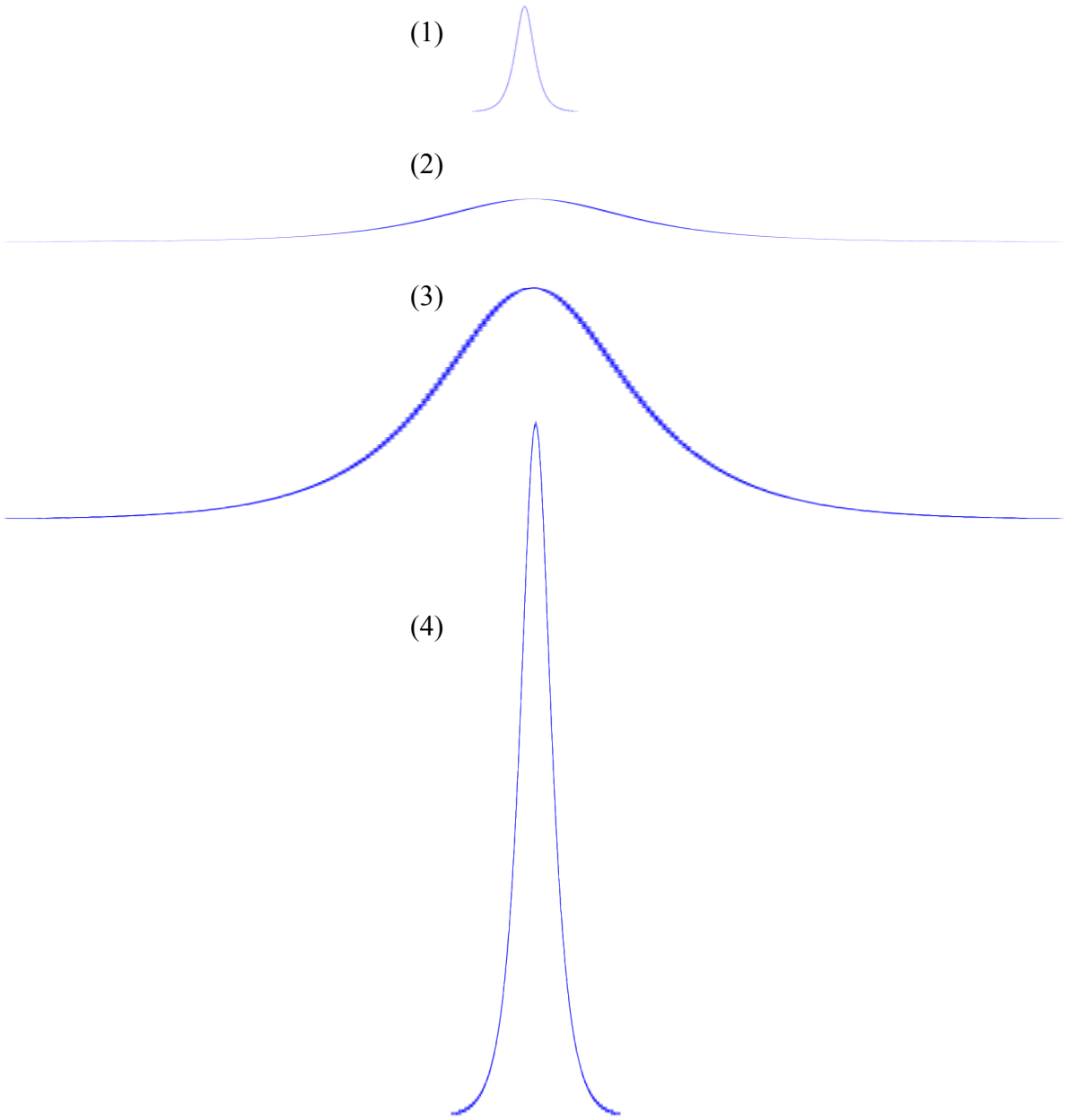

Figure 3.10: Chirped Pulse Amplification is a technique for amplifying pulses while avoiding optical damage. The method begins with a pulse (1) which is stretched by several orders of magnitude temporally (2) and then safely amplified (3). After which, the amplified pulse is compressed (4) resulting in a high intensity short pulse. (The amplitude and width of the pulses shown are not to scale.)

caused by the stretcher.

In principle, reacquiring the unamplified pulse duration is limited by only gain narrowing, which causes the frequencies at the peak of the gain curve to be amplified more than those at the edges. In practice, the pulse shape and duration are also limited by higher orders of dispersion. Compensation of the second and third order dispersion of the amplified pulse is dependent on three compressor parameters: (1) the grating groove density, (2) the angle of incidence on the grating, and (3) the grating separation, where only the latter two can be adjusted.

3.2.1 Laboratory Built Femtosecond Laser / BMI Amplifier

Experiments using short pulse excitation at 800 nm were carried out using an amplified laser system. A laboratory built mode-locked Ti:sapphire oscillator, based on the design of Murnane and Kapteyn [15], is pumped with a Spectra-Physics Millennia laser, and the output from the oscillator seeds a BMI α-1000 US regenerative amplifier. A typical spectrum of a pulse out of the Ti:sapphire oscillator is shown in Figure 3.11.

The mechanism which drives the self-locking of the modes in the oscillator is Kerr-lens mode-locking (KLM) [16]. KLM is based on the nonlinear intensity dependence in the index of refraction, which affects both the temporal (self-phase modulation [5]) and spatial (self-focusing [17]) characteristics of the radiation as it interacts with the laser medium.

The Spectra-Physics Millennia pump laser is based on a neodymium yttrium vanadate ($Nd:YVO_4$) crystal [18] with a transition energy of 1064 nm. The crystal is pumped by two fiber-coupled high power laser diode bars (AlGaAs [8]). The laser is intracavity doubled in a noncritically phase-matched lithium triborate (LiB_2O_3 or LBO) crystal [8]. The Millennia

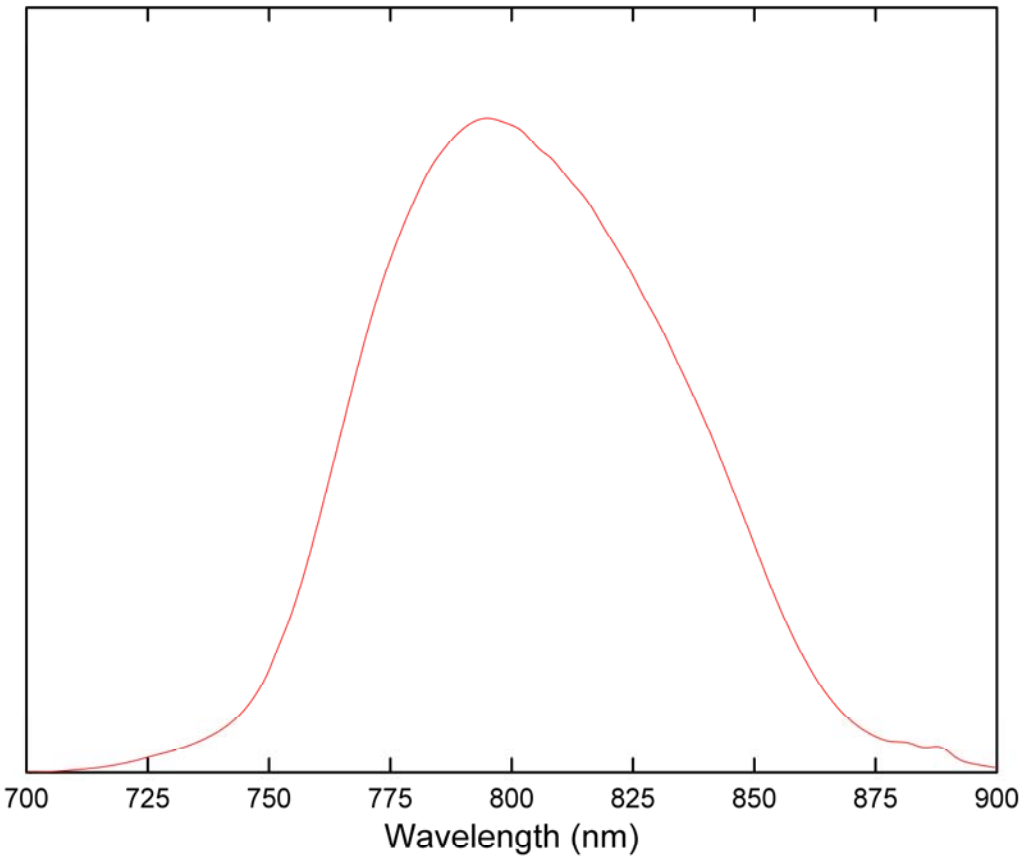

Figure 3.11: The oscillator spectrum is centered at 795 nm and has a FWHM of 78 nm.

produces a continuous wave of green light at 532 nm with ~ 5 W maximum power.

The BMI α-1000 US 1 kHz Amplifier System [19] is based on the principle of chirped pulse amplification [14]. Explained below are the three components of this system: the stretcher, the amplifier, and the compressor.

The stretcher component consists of a single grating and an afocal device, meaning that the optical components introduce no net convergence or divergence of the beam. An important property of the stretcher is its chromatic and spherical aberration-free design [20]. This is achieved with an afocal all-reflective Öffner triplet [21].

Trapping of the seed pulse in the amplifier cavity is achieved by changing the polarization of the pulse so that it is transmitted through a polarizer which would have otherwise reflected the pulse out of the cavity [22]. When the seed pulse transits a Pockels cell [23] (which uses a potassium di-deuterium phosphate (KD*P) crystal [8]) located in the amplifier cavity, a high voltage is applied changing the polarization of the pulse. The trapped seed pulse is amplified and then released by applying a second high voltage to the Pockels cell, reverting the pulse to its original polarization. Timing electronics allows for the synchronization between the oscillator and the regenerative amplifier.

Once trapped in the cavity, the stretched seed pulse is amplified in a Ti:sapphire crystal [12] pumped with a flashlamp pumped intracavity doubled multi-kHz Nd:YLF ($Nd:LiYF_4$) laser. In the pump laser assembly, the output of a krypton continuous discharge DC arc lamp, produced by Verre et Quartz, pumps the Nd:YLF rod [18]. The CW output of the Nd:YLF rod at 1053 nm is Q-spoiled [24] by an intracavity acousto-optic Q-switch [25] and intracavity doubled in an LiB_2O_3 (LBO) crystal [8]. The pump laser outputs a 500 ns pulse at 527 nm with ~ 12 W maximum power.

The compressor component reverses the wavelength dependent path lengths introduced by the stretcher. The compressor compensates for the second and third order dispersion introduced by the stretcher and amplifier with a parallel grating pair. The compressor can also be adjusted to compensate for dispersion due to additional optical components introduced between the output of the compressor and the sample.

The system produces optical pulses 35 fs in duration, with a 1 kHz repetition rate, centered at 800 nm, and having an energy of ~ 1 mJ per pulse. A representative measurement of the output pulse width and spectrum are shown in Figures 3.4 and 3.5, respectively.

3.2.2 Spectra-Physics Hurricane Commercial Femtosecond Laser

Experiments involving tunable excitation pulses were carried out using the Spectra-Physics Hurricane system. This system is an all diode pumped, kilohertz Ti:sapphire regenerative amplifier system composed of five modular components: (1) The Mai Tai, which is an actively mode-locked Ti:sapphire oscillator, (2) the stretcher optics, (3) the Evolution pump laser, (4) the regenerative amplifier, (5) and the compressor optics. The latter four components make up the chirped pulse amplification scheme [14].

The Mai Tai component employs an active mode-locking scheme [26] via an acousto-optical modulator (AOM) inserted into the oscillator cavity. The AOM, which generates a periodic loss in the cavity, is driven with a RF signal having a frequency related to the cavity length. The active mode-locking method is as follows. Initially, the Mai Tai is operating in a partially phase-locked condition where mode beating occurs at the cavity frequency. This is detected by a photodiode and amplified. The AOM is set to twice the cavity frequency where the phase is set to allow maximum transmission of the pulse in the modulator. Variations in the

cavity length due to environmental effects are compensated for in real-time via a feed-back loop that adjusts the RF signal frequency.

The oscillator pulse is amplified in a Ti:sapphire crystal that is pumped by Positive Light's Evolution: a diode pumped (AlGaAs [8]) Nd:YLF [18], which lases at 1053 nm, and is acousto-optic Q-switched [25]. An intracavity noncritically phase-matched LBO crystal [8] produces pulsed green light at 527 nm via second harmonic generation [9]. The Evolution produces optical pulses ~ 100 ns in duration with ~ 8 W maximum power.

The stretcher (and compressor) use a four-pass configuration where the pulse is positively (and negatively, for the case of the compressor pass) chirped by diffraction off of a single grating with 2000 lines per mm. After deflection off of a mirror, the pulse reflects off of the grating a second time. The pulse then retraces its path though the stretcher (compressor) to spatially reconstruct the beam profile.

The system produces optical pulses ~ 110 fs in duration, with a 1 kHz repetition rate, centered at 800 nm, and having an energy of ~ 1 mJ per pulse. A representative measurement of the Hurricane pulse duration and spectrum are shown in Figures 3.12 and 3.13, respectively.

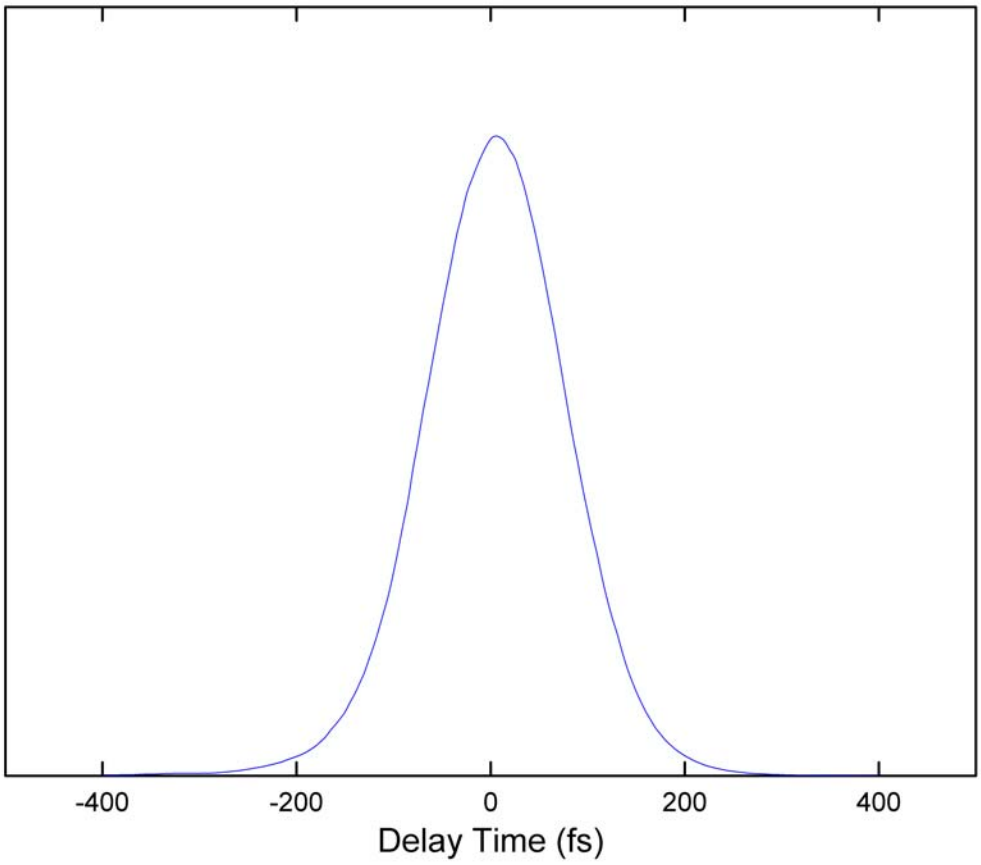

Figure 3.12: An autocorrelation of a 107 fs FWHM ($sech^2(t)$) pulse out of the Hurricane system. The measurement was taken using a BBO crystal.

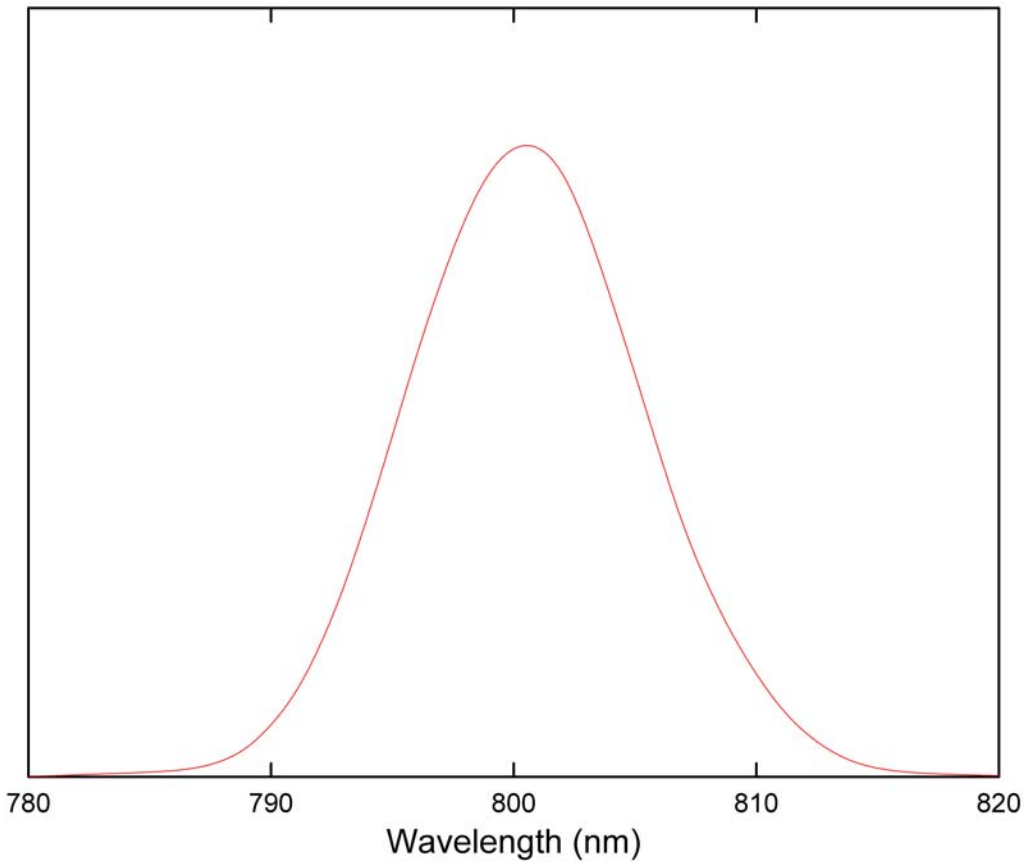

Figure 3.13: The Hurricane spectrum is centered at 800 nm and has a FWHM of 12 nm.

A portion of the output from the Hurricane amplifier is diverted to the Spectra-Physics 800C Ultrafast Optical Parametric Amplifier (OPA) [27]. In optical parametric amplification, a high intensity pump beam amplifies a low intensity seed beam resulting in a signal and idler beam. The process can be thought of as an input pump photon being split into two lower energy photons as constrained by energy conservation:

$$\omega_{pu} = \omega_s + \omega_i \tag{3.7}$$

where ω_{pu} is the pump frequency ($\propto$ 1 / 800 nm), ω_s is the signal frequency, and ω_i is the idler frequency [28]. Momentum conservation requires that

$$\frac{n_{pu}}{\lambda_{pu}} = \frac{n_s}{\lambda_s} + \frac{n_i}{\lambda_i} \tag{3.8}$$

where λ is the input wavelength and n is the refractive index of the nonlinear crystal, which is dependent on frequency and input angle. The added condition of momentum conservation allows for the tunability of the output wavelength by changing the nonlinear crystal angle relative to the input beams and thereby changing n.

The Spectra-Physics OPA uses a small amount of the output of the Hurricane amplifier (at 800 nm) focused into a sapphire plate in order to generate a white light continuum [4], which is used as the seed beam in the parametric process. The remainder of the Hurricane output is used as the pump. Optical parametric amplification requires that both the pump and the seed pulse are temporally and spatially overlapped in a BBO crystal. In conjunction with adjusting the BBO crystal angle, the time delay of the continuum seed pulse can be varied in order to amplify a specific portion of the chirped continuum pulse. Additional wavelengths can be generated using second harmonic generation, which frequency doubles either the signal or idler beam in a second BBO crystal.

The spectrum of the OPA output is significantly broader than the Hurricane output, which allows for a shorter pulse. The OPA output produces optical pulses tunable from ~ 0.5 to ~ 2 μm with an energy of ~ 20 μJ per pulse where the short wavelength range is achieved by second harmonic generation of the infrared OPA output. The output of the OPA can be used as either the pump or the probe or both. A second OPA allows for separately tunable pump and probe pulses. In the multiple pump-probe measurements discussed in Chapter 5, the OPA output was centered at 1.31 μm and was used as both a pump and a probe. Compression of the OPA pulse is accomplished with a dispersive delay line constructed from a pair of fused silica prisms. An autocorrelation and spectrum of a compressed OPA pulse is shown in Figures 5.1 and 5.2, respectively.

Also available was a laboratory built single-stage blue pumped noncollinearly phase matched optical parametric amplifier (NOPA) [29] tunable from the visible to the near infrared [30]. The two pulses used in the NOPA are generated as follows. The output of the amplifier is frequency doubled, generating a pulse centered at 400 nm. A white light continuum is produced by focusing a portion of the amplifier output into a 2 mm sapphire plate. In the NOPA, the blue pump pulse and a continuum seed pulse are overlapped (in time and space) in a BBO crystal. The timing between the pump and probe pulse and the tilt of the BBO crystal are adjusted for a particular output wavelength of either the signal or idler pulse. As compared to the OPA, the NOPA provides the possibility of shorter pulses at the expense of output power.

3.3 Vibrationally Impulsive Excitation

To time resolve the vibrational dynamics, the impulsive excitation technique is employed. This process is possible only when the optical pulses used to excite the material are short compared to the material's characteristic vibrational periods [31]. The impulsive limit is defined as the limit in which the pulse duration is less than a single vibrational period. When the pulse duration is short with respect to the vibrational period, the bandwidth of the optical pulse spans a number of vibrational sublevels within an electronic state.

The observation of coherent vibrational motion requires, not only being within the impulsive limit, but also that the vibrational mode has some degree of coupling to the electronic excitation. In the case where these criteria are true, short pulse excitation produces a coherent superposition of vibrational states forming nonstationary vibrational wavepackets. As described in more detail below, vibrational wavepackets can be generated on both the excited state electronic potential energy surface and the ground state surface. Using the pump-probe technique it is possible to time-resolve the vibrational motion since the wavepacket motion modulates the transient absorbance signal [32-34].

The impulsive excitation processes for a molecular system are shown schematically in Figures 3.14 and 3.15 where the vertical axis represents the potential energy and the horizontal axis represents a normal coordinate. Shown in the figures are the ground (S_0) and excited state (S_1), the vibrational sublevels within each state, and the vibrational wavepacket.

3.3.1 The Excited State

Generation of the excited state wavepacket is detailed in Figure 3.14. This process begins when the molecule in the ground vibrational state (in blue) on the ground state surface (S_0) is

impulsively excited (represented by the vertical red arrow) by the pump pulse, creating a coherent superposition of vibrational states, or a wavepacket, in the excited state (S_1). On the excited state surface the wavepacket evolves (represented by the **black** arrow) due to a change in the equilibrium internuclear separation (i.e., well minimum). For the simplified case of a harmonic potential well, the wavepacket would oscillate at the characteristic frequency of the well. The vertical transition indicates that no nuclear motion occurs during the transition, and follows from the Franck-Condon principle [35]. Condon notes that, "the electronic transition is supposed to happen in a negligibly short time as compared to the period of the nuclear vibrations."

In a pump-probe experiment, the pump pulse generates a wavepacket in the excited state. After this, the probe pulse investigates the state of the wavepacket (not shown in figure). By varying the relative time delay between the pump and the probe pulse, the evolution of the wavepacket is monitored. Probe pulse interaction can result in the wavepacket transition to a higher electronic state (seen in the signal as an induced absorption) or the wavepacket can undergo stimulated emission to a lower electronic state (seen in the signal as an induced transmission). Wavepacket motion is seen in the signal as an oscillatory modulation at the frequency of the excited state vibration.

In the case of self-trapping, structural changes occur after impulsive excitation. The self-trapping dynamics that result are monitored by observing the excited state wavepacket evolution. Time-resolved pump-probe measurements have uncovered excited state wavepacket oscillations in PtX(en), discussed in Chapters 4.

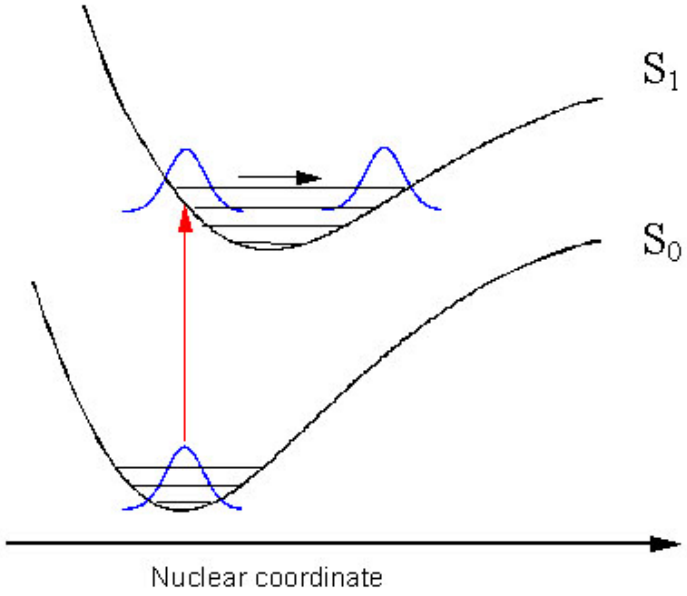

Figure 3.14: Schematic of the potential energy surfaces for an impulsive excitation where the optical response has a contribution from an excited state vibration.

3.3.2 The Ground State

Ground state vibrational wavepackets can be generated by the resonantly enhanced stimulated impulsive Raman process [32] shown in Figure 3.15. Initially a pump field brings the system to the excited state. Within the duration of the pump pulse, the non-stationary wavepacket starts to evolve on the excited state potential energy surface. It then interacts with the pump field a second time, driving the wavepacket down to the ground state at a position displaced from the initial equilibrium position. The nonstationary ground state wavepacket motion is monitored with a time delayed probe pulse. The probe pulse is absorbed in the transition of the nonstationary ground state wavepacket to the higher electronic state, which is seen as an induced absorbance signal with oscillatory modulation at the frequency of the ground state vibration.

The amplitude of the wavepacket oscillation from the electronic ground state is dependent on the duration of the pump pulse [32]. No ground state vibration would be observed in the two limiting cases of a delta-function pump pulse (with a FWHM of zero) and a pump pulse with a duration greater than the vibrational period. For the case of a very short pulse, the excited state wavepacket does not become significantly displaced before returning to the ground state, resulting in only small amplitude oscillation about the ground state equilibrium position. For the case of a pulse duration approaching the vibrational period, its duration allows for a longer period of wavepacket evolution on the excited state surface, resulting in a dispersive spread of the wavepacket. Therefore, the wavepacket that returns to the ground state more closely approaches that of the stationary state, resulting in only small amplitude oscillations. The optimum pulse width for generating coherent ground state vibrations lies between these two extrema.

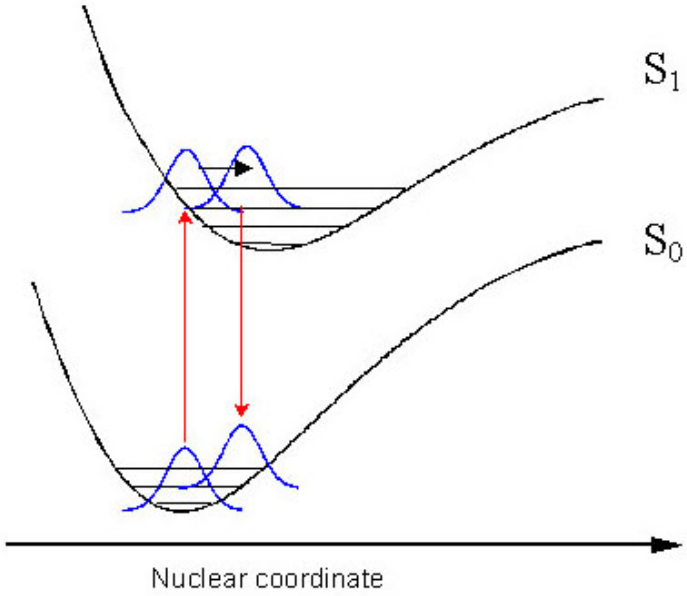

Figure 3.15: Schematic of the potential energy surfaces for an impulsive excitation where the optical response has contributions from the ground state vibrations.

3.4 References for Chapter 3

1. Ippen, E. and C. Shank, *Techniques for measurements* in Ultrashort light pulses. Picosecond techniques and applications. Topics in applied physics. Volume 18. Shapiro, S., Editor. 1977, New York: Springer-Verlag. chapter 3; (also, Reference [27], pp. 417-420 and pp. 204-228, first and second book cited, respectively); the pump-probe technique uses an optical apparatus that loosely resembles a Michelson interferometer. In the literature, this system is sometimes referred to as a "Michelson-like" apparatus. The "original" Michelson interferometer is described in the following reference and illustrated in Figure 1 therein: Michelson, A., *The relative motion of the earth and the luminiferous ether.* The American Journal of Science, 1881. **22**: pp.120-129; Michelson, A., *On the application of interference-methods to spectroscopic measurements. I.* Philosophical Magazine and Journal of Science, 1891. **31**: pp. 338-346; the subsequent references discuss the use of this instrument for spectroscopic measurements: Michelson, A., *On the application of interference-methods to spectroscopic measurements. II.* Philosophical Magazine and Journal of Science, 1892. **34**: pp. 280-299.

2. Meade, M., *Lock-in amplifiers: principles and applications*. 1983, London: Peter Peregrinus; phase sensitive detection was demonstrated for the first time: Dicke, R., *The measurement of thermal radiation at microwave frequencies*. The Review of Scientific Instruments, 1946. **17**(7): pp. 268-275.

3. Diels, J. and W. Rudolph, *Ultrashort laser pulse phenomena: fundamentals, techniques, and applications on a femtosecond time scale.* 1996, San Diego: Academic Press. chapters 5-9; C. Hirlimann, A. Ducasse, C. Rulliére, B. Couillaud, T. Amand, X. Marie, F. Salin, L. Sarger, J. Oberlé, M. Joffre, and A. Bonvalet, *Femtosecond laser pulses: Principles and experiments.* Rulliére, C., Editor. 1998, Germany: Springer. chapters 3-4, 6-8.

4. Fork, R., C. Shank, C. Hirlimann, R. Yen, and W. Tomlinson, *Femtosecond white-light continuum pulses.* Optics Letters, 1983. **8**(1): pp. 1-3; this phenomenon was first reported in: Alfano, R. and S. Shapiro, *Emission in the region 4000 to 7000 Å via four-phonon coupling in glass.* Physical Review Letters, 1970. **24**(11): pp. 584-587.

5. Boyd, R., *Nonlinear Optics*, 1992, California: Academic Press. *(self-phase modulation, $\chi^{(3)}$)* chapter 4, pp. 275-277; first identified and reported by Brewer, R., *Frequency shifts in self-focused light.* Physical Review Letters, 1967. **19**(1): pp. 8-10; the process was theoretically explained by Shen, Y. and Loy, M., *Theoretical interpretation of small-scale filaments of light originating from moving focal spots.* Physical Review A, 1971. **3**(6): pp. 2099-2105.

6. Malus, E., *Sur une propriété de la lumière réfléchie par les corps diaphanes.* Memoires de Physique et de Chimie. Société d'Arcueil (On a property of the light reflected by the diaphanous bodies, Memoires of Physics and Chemistry. Society of Arcueil), 1809. **2**: pp. 143-158.

7. Weber, H., *Method for pulsewidth measurement of ultrashort light pulses generated by phase-locked lasers using nonlinear optics*. Journal of Applied Physics, 1967. **38**(5): pp. 2231-2234; Armstrong, J., *Measurement of picosecond laser pulse widths*. Applied Physics Letters, 1967. **10**(1): pp.16-18.

8. Dmitriev, V., G. Gurzadyan, and D. Nikogosyan, *Handbook of nonlinear optical crystals.* 1999, New York: Springer.

9. Boyd, R., *Nonlinear Optics*, 1992, California: Academic Press. *(second harmonic generation, $\chi^{(2)}$)* pp. 78-85; first reported by Franken, P., A. Hill, C. Peters, and G. Weinreich, *Generation of optical harmonics.* Physical Review Letters, 1961. **7**(4): pp. 118-119.

10. Fork, R., O. Martinez, and J. Gordon, *Negative dispersion using pairs of prisms.* Optics Letters, 1984. **9**(5): pp. 150-152.

11. Huang, C., H. Kapteyn, J. McIntosh, and M. Murnane, *Generation of transform-limited 32-fs pulses from a self-mode-locked Ti:sapphirelaser.* Optics Letters, 1992. **17**(2): pp. 139-141.

12. Moulton, P., *Spectroscopic and laser characteristics of Ti:Al_2O_3.* Journal of the Optical Society of America B, 1986. **3**(1): pp. 125-132.

13. Hargrove, L., R. Fork, and M. Pollack, *Locking of He-Ne laser modes induced by synchronous intracavity modulation.* Applied Physical Letters, 1964. **5**(1): pp. 4-5; DiDomenico, Jr., M., *Small-signal analysis of internal (coupling-type) modulation of lasers.* Journal of Applied Physics, 1964. **35**(10): pp. 2870-2876; these articles include the first reported mode-locking of a laser resonator and the theoretical constructs for the "internal locking of the optical cavity modes", respectively; mode-locking was first proposed by Lamb, W., *Theory of an optical maser.* Physical Review, 1964. **134**: pp. A1429-A1450.

14. Maine, P., D. Strickland, M. Pessot, J. Squier, P. Bado, G. Mourou, and D. Harter, *Chirped pulsed amplification: Present and future*. in Ultrafast Phenomena VI, T. Yajima, K. Yoshihara, C. Harris, and S. Shionoya, Editors. 1988, Springer-Verlag. pp. 2-7; the principle of chirped pulse amplification (CPA) has been extensively employed for decades in radar systems and was referred to as pulse coding and compression (PCC). The premise behind the technique of PCC is to use a long amplified pulse to obtain a target size and distance (as accurately as if a short pulse, which requires excessively high transmission power for adequate range, had been used). The process sends a weak short pulse through a dispersion delay line (*chirped*), followed by an amplifier unit, whereupon it is sent to a transmission array antenna and then to the target. The return pulse (*chirped*) reflected from the target and received by the array is amplified and sent to a compression line. The pulse is then reconstructing by compressing it into its original duration thereby retrieving the target information; Brookner, E., *Phased-Array Radars*. Scientific American, 1985. **252**(2): pp. 94-102; the following reference is the first experiment reporting of applying PCC to the optical regime: Strickland, D. and G. Mourou, *Compression of amplified chirped optical pulses*.

Optical Communications, 1985. **56**(3): pp. 219-221.

15. Asaki, T., C. Huang, D. Garvey, J. Zhou, H. Kapteyn, M. Murnane, *Generation of 11-fs pulses from a self-mode-locked Ti:sapphirelaser.* Optics Letters, 1993. **18**(12): pp. 977-979; it is interesting to note that some of the studies undertaken in this dissertation were conducted in the same laboratory space once occupied by the above named individuals; that being, facilities on the 6th floor of the multi-million dollar Kate B. Webster Physical Sciences building, Department of Physics, 99164-2814. Kapteyn-Murnane Laboratories L.L.C. was started in late 1994 and now provides Ti:sapphire oscillators and amplifiers.

16. Spence, D. P. Kean, and W. Sibbertt, *60-fsec pulse generation from a self-mode-locked Ti:sapphire laser.* Optics Letters, 1991. 16(1): pp. 42-44.

17. Boyd, R., *Nonlinear Optics*, 1992, California: Academic Press. *(self-focusing, $\chi^{(3)}$)* pp. 257-258, 261-262; first reported in a presentation at the 1964 Spring meeting of the Optical Society of America: *(abstract)* Hercher, M., *Laser-induced damage in transparent media.* Journal of the Optical Society of America, 1964. **54**(4): p. 563; a thorough discussion of the process has been given by Kerr, E., *Filamentary tracks formed in transparent optical glass by laser beam self-focusing. II. Theoretical analysis.* Physical Review A, 1971. **4**(3): pp. 1195-1218.

18. Harmer, A., *Fluorescence of Nd^{3+} in lithium yttrium fluoride.* Journal of Physics and Chemistry of Solids, 1969. **30**: pp. 1483-1491.

19. Salin, F., J. Squier, G. Mourou, and G. Vaillancourt, *Multikilohertz $Ti:Al_2O_3$ amplifier for high-power femtosecond pulses.* Optics Letters, 1991. **16**(24): pp. 1964-1966; Vaillancourt, G., T. Norris, J. Coe, P. Bado, G. Mourou, *Operation of a 1-kHz pulse-pumped Ti:sapphireregenerative amplifier.* Optics Letters, 1990. **15**(6): pp. 317-319; the author has enjoyed many insightful discussions with Gary Vaillancourt while resolving technical issues with the BMI amplifier system.

20. Cheriaux, G., P. Rousseau, F. Salin, J. Chambaret, B. Walker, L. Dimauro, *Aberration-free stretcher design for ultrashort-pulse amplification.* Optics Letters, 1996. **21**(6): pp. 414-416.

21. Offner, A., *Unit power imaging catoptric anastigmat.* June 21, 1971, U.S. patent, 3,748,015.

22. Bado, P., M. Bouvier, J. Coe, *Nd:YLF mode-locked oscillator and regenerative amplifier.* Optics Letters, 1987. **12**(5): pp. 319-321; Figure 3 in this reference illustrates pulse "catch and release" in a regenerative amplifier.

23. Pockels, F., *Ueber den Einfluss des elektrostatischen Feldes auf das optische Verhalten piëzoelektrischer Krystalle.* Abhandlungen der Königlichen Gesellschaft der Wissenschaften zu Göttingen Mathematisch Physikalische Klasse (Over the influence of the electrostatic field on the optical behavior of piezoelectric crystal, Papers of the royal society of the sciences to Goettingen, mathematical physical class), 1893. **39**: p. 1-204; Pockels F., *Lehrbuch der Kristallopti (Text book of crystal optics)*, 1906, Leipzig und Berlin: B.G. Teubner.

24. Hellwarth, R., *Control of fluorescent pulsations* in Advances in Quantum Electronics. J. Singer, Editor. 1961, New York: Coloumbia University Press. pp. 334-341; Hellwarth, R. and F. McClung, *Giant pulsations from Ruby.* Journal of Applied Physics, 1962. **33**: pp. 838-841; first reports on Q-switching.

25. Bommel, H. And K. Dransfield, *Excitation of very high frequency sound in quartz.* Physical Review Letters, 1958. 1: page 237; L. Brillouin, *Diffusion de la lumiere et des rayons X par un corps transparent homegene.* Annuaires de la Physique (Diffusion of the light and x-rays by a transparent homogeneous body. Annuals of Physics), 1922. **17**: pp. 88; acousto-optical modulation was first experimentally observed and theoretical considered by the above two references, respectively; Slater discovers that when the light is incident upon the acoustic wavefront at the Bragg angle maximum scattering occurs: Slater, J. *Interactions of waves in crystals.* Review of Modern Physics, 1958. 30: page 197-222.

26. Kuizenga, J. and A. Siegman, *FM and AM mode locking of the homogeneous laser – Part I: Theory.* IEEE Journal of Quantum Electronics, 1970. **6**(11): pp. 694-708; first paper on active mode-locking theory of a solid state laser with either phase (FM) or amplitude (AM) modulation.

27. Cerullo, G. and S. DeSilvestri, *Ultrafast optical parametric amplifiers.* Review of Scientific Instruments, 2003. **74**(1): pp. 1-18; the first experimental observation of optical parametric amplification is presented in the following reference: Giordmaine, J. and R. Miller, *Tunable Coherent Parametric Oscillation in $LiNbO_3$ at Optical Frequencies*. Physical Review Letters,

1965. **14**(24): pp. 973-976; the first theoretical treatment of optical parametric amplification where the pump, signal, and idler wave is free to have different directions of propagation: Kroll, N., *Parametric Amplification in Spatially Extended Media and Application to the Design of Tuneable Oscillators at Optical Frequencies*. Physical Review, 1962. **127**(4): pp. 1207-1211; the fundamental idea was first consider in: Lord Rayleigh, *On maintained vibrations.* The London, Edinburgh and Dublin Philosophical Magazine and Journal of Science, 1883. series 5, volume 15: pp 229-235; Lord Rayleigh, *On the maintenance of vibrations by forces of double frequency, and on the propagation of waves through a medium endowed with periodic structure.* The London, Edinburgh and Dublin Philosophical Magazine and Journal of Science, 1887. series 5, volume 24: pp 145-159.

28. Boyd, R., *Nonlinear Optics*, 1992, California: Academic Press. *(parametric amplification, $\chi^{(2)}$)* pp. 75-78; Yariv, A. *Quantum Electronics*, Third Edition. 1989, New York: John Wiley & Sons. pp. 407-411.

29. Wilhelm, T., J. Piel, and E. Riedle, *Sub-20-fs pulses tunable across the visible from a blue-pumped single-pass noncollinear parametric converter.* Optics Letters, 1997. **22**(19): pp. 1494-1496; the first communication of an optical parametric amplifier pumped with a blue pulse and seeded with a white-light continuum: Reed, M., M. Steiner-Shepard, M. Armas, and D. Negus, *Microjoule-energy ultrafast optical parametric amplifiers.* Journal of the Optical Society of America B, 1995. **12**(11): pp. 2229-2236.

30. Piel, J., M. Beutter, and E. Riedle, *20-50-fs pulses tunable across the near infrared from a blue-pumped noncollinear parametric amlifier.* Optics Letters, 2000. **25**(3): pp. 180-182.

31. Dhar, L., J. Rogers, K. Nelson, *Time-resolved vibrational spectroscopy in the impulsive limit.* Chemical Reviews, 1994. **94**: pp. 157-193.

32. Pollard, W., S. Dexheimer, Q. Wang, L. Peteanu, C. Shank, and R. Mathies, *Theory of dynamic absorption spectroscopy of nonstationary states. 4. Application to 12-fs resonant impulsive raman spectroscopy of bacteriorhodopsin.* The Journal of Physical Chemistry, 1992. **96**: pp.6147-6158.

33. Dexheimer, S., Q Wang, L. Peteanu, W. Pollard, R. Mathies, and C. Shank, *Femtosecond impulsive excitation of nonstationary vibrational states in bacteriorhodopsin.* Chemical Physics Letters, 1992. **188**(1,2): pp. 61-66.

34. Pollard, W., S. Lee, and R. Mathies, *Wave packet theory of dynamic absorption spectra in femtosecond pump-probe experiments.* Journal of Chemical Physics, 1990. **92**(7): pp. 4012-4028.

35. Condon, E., *A theory of intensity distribution in band systems.* Physical Review, 1926. **28**(6): pp. 1182-1201; Franck, J., *Elementary processes of photochemical reactions.* Transactions of the Faraday Society, 1926. **21**: pp. 536-542.

Chapter 4

Observation of the Self-Trapping Dynamics in the Weak Electron-Phonon Coupling Limit

The structural tunability of the PtX complexes allows for a systematic investigation of the self-trapping dynamics. Halide substitution, discussed in Section 2.3, allows for the varying of the relative electron-phonon coupling strength, where the characteristics of these systems range from the highly distorted valence-localized PtCl to the less distorted valence-delocalized PtI. PtBr represents the intermediate case of moderate distortion and delocalization. The studies conducted by the author on the PtI complex (documented in this chapter) along with previous impulsive excitation studies carried out on PtBr [1] and PtCl [2] provide a comprehensive picture of the self-trapping dependence on the electron-phonon coupling strength, which extends over a wide range.

Much of the interpretation of the PtX series is based on impulsive excitation pump-probe experiments conducted by Aaron Van Pelt on the intermediate strength electron-phonon coupled PtBr [1,3]. The interpretation of the PtBr measurements has established the spectroscopic signatures of the self-trapped exciton dynamics. A review of this interpretation will provide a framework for explaining the results of PtI presented in Sections 4.2 to 4.4.

4.1 Review of PtBr Data and Analysis

Impulsive excitation of the IVCT transition in $[Pt(en)_2Br_2][Pt(en)_2]\cdot(PF_6)_4$ (or PtBr) leads to the formation of a self-trapping exciton, which is evident based on spectroscopic signatures established by Van Pelt [1,3]. These spectroscopic signatures include: (1) self-trapped exciton

formation identified by an induced absorbance, and (2) the measurement of a ~ 110 cm^{-1} oscillatory component associated with the excited state vibrational dynamics. In addition, oscillatory modulation from the impulsive Raman excitation of the ground state is also observed in these measurements.

Initial measurements on PtBr conducted by Van Pelt were carried out using a degenerate pump-probe configuration. In these experiments, the measurement was carried out on PtBr using an optical pump-probe apparatus, where a beamsplitter generates a pump and probe pulse. A fixed pump and a variable probe path length provide a time delay between the pulses. The differential transmittance was measured using lock-in amplification. (The details of the experimental setup are presented in Section 3.1.) A 1 kHz Ti:sapphire regenerative amplifier (discussed in Section 3.2.1) produces optical pulses 35 fs in duration centered at 800 nm. This setup was chosen since the spectrum of the pulse overlaps both the IVCT transition and the self-trapped exciton absorbance [4,5].

Figure 4.1 shows the time-resolved differential transmittance of PtBr using an 800 nm pump and a detection wavelength of 830 nm. In the figure, the y-axis represents the differential transmittance ($\Delta T / T$) where a negative value indicates an induced absorbance. The x-axis represents the delay time where at positive delay the probe arrives after the pump pulse. The data show an induced absorbance that is modulated by wavepacket oscillations.

The linear prediction singular value decomposition method (LPSVD) [6], briefly explained in Appendix A, was used to fit the data to a sum of exponentially damped cosines and exponentials:

$$S(t) = \sum_i a_i \, e^{-\frac{t}{\tau_i}} \cos(2\pi \nu_i t + \phi_i) \tag{4.1}$$

where the sum is over i (the number of components), a_i is the amplitude, τ_i is the exponential decay constant, υ_i is the frequency, and ϕ_i is the phase. Exponential decays are included as zero-frequency components. Van Pelt found that the simple exponentially damped cosine wave model for the vibrational dynamics provided an excellent characterization of the time-resolved response. The result of this analysis are plotted with a solid line on top of the data in Figure 4.1. The fits were started at a delay time of ~ 100 fs to avoid complications arising from temporal overlap of the pump and probe pulse leading to nonlinear optical processes (e.g., cross-phase modulation [7,8]). The parameters of the individual components obtained from the LPSVD are listed in Table 4.1. Contributing to the signal are four oscillatory components and two exponentials.

Three of the vibrational frequencies are attributed to the ground state response. These include the fundamental ground state oscillation of the symmetric stretch mode at 176 cm^{-1} and its harmonics at 351 cm^{-1} and 510 cm^{-1}. These vibrations have been observed in the Raman spectrum of PtBr [4,9-11] with Raman line widths consistent with the observed pump-probe measured dephasing times. The ground state mechanism is the resonantly enhanced impulsive stimulated Raman process discussed in Section 3.3.2.

Not seen in the Raman spectrum, but observed in the pump-probe data, is a large amplitude strongly damped component at ~ 110 cm^{-1}. This low frequency component is assigned to the self-trapping dynamics associated with the lattice motion that drives the system to the self-trapped state. Accompanying this vibration is a formation of the induced absorbance discussed below. A detailed discussion of the excited state response, in terms of the nondegenerate pump-probe measurements, is presented later.

There are two zero-frequency components observed: a fast formation of the induced absorbance associated with the self-trapped state and a slow decay representing the self-trapped exciton depopulation. The fast exponential formation component has a time constant comparable to a single vibrational period of the low frequency vibration (~ 300 fs period) associated with the self-trapping. This rapid formation is consistent with a barrierless transition of the exciton from a free to self-trapped state in one-dimension, as discussed in Section 2.6. A long term exponential decay of the induced absorbance, on the order of tens of picoseconds, reflects the lifetime of the self-trapped exciton. This optical absorption is characteristic of a probe induced transition from the self-trapped exciton potential to a higher-lying electronic state.

The individual components determined from the LPSVD are plotted in Figure 4.2. The sum of these components equals the solid fit line in Figure 4.1.

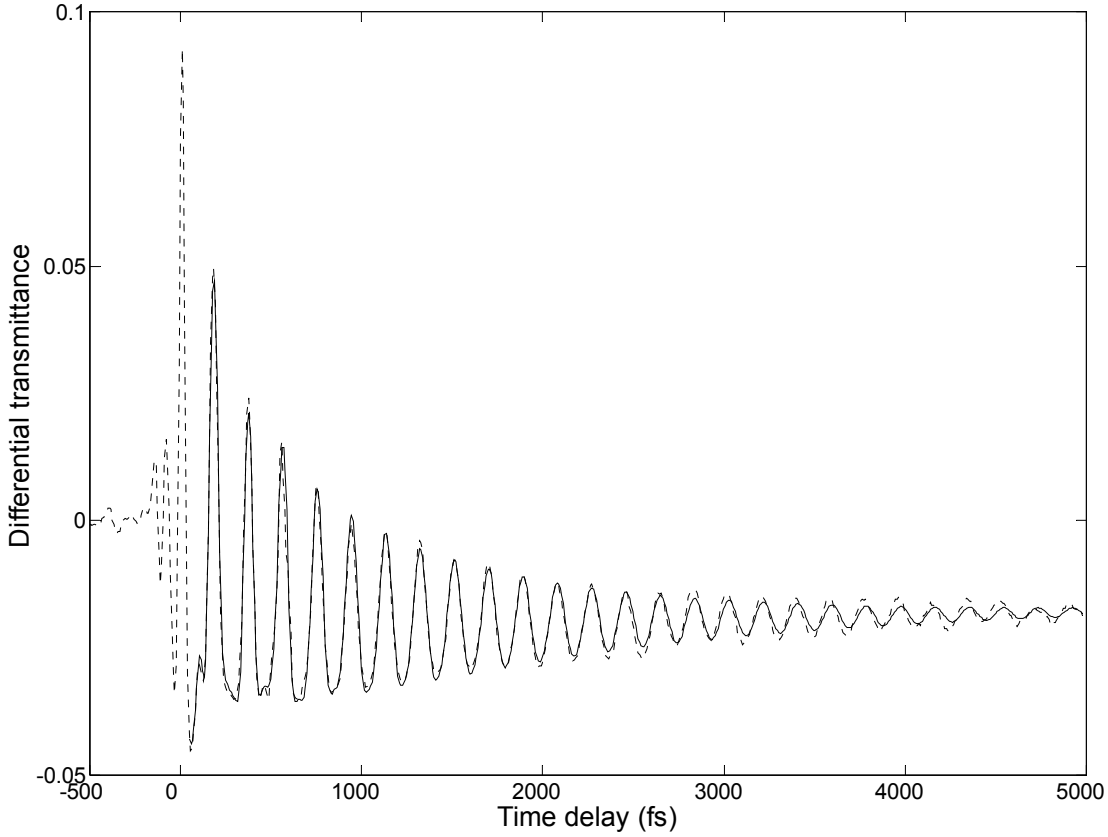

Figure 4.1: Comparison of the differential transmittance of PtBr (dotted line) with a fit to the multi-component model (solid line) of Equation 4.1. In the degenerate pump-probe measurement, PtBr was excited with a 35 fs pulse centered at 800 nm and probed at a detection wavelength of 830 nm. (Reprinted with permission from Dexheimer, S. L., A. D. Van Pelt, J. A. Brozik, and B. I. Swanson, Journal of Physical Chemistry A, 2000. **104**(18): pp. 4308-4313. Copyright 2000, American Chemical Society.)

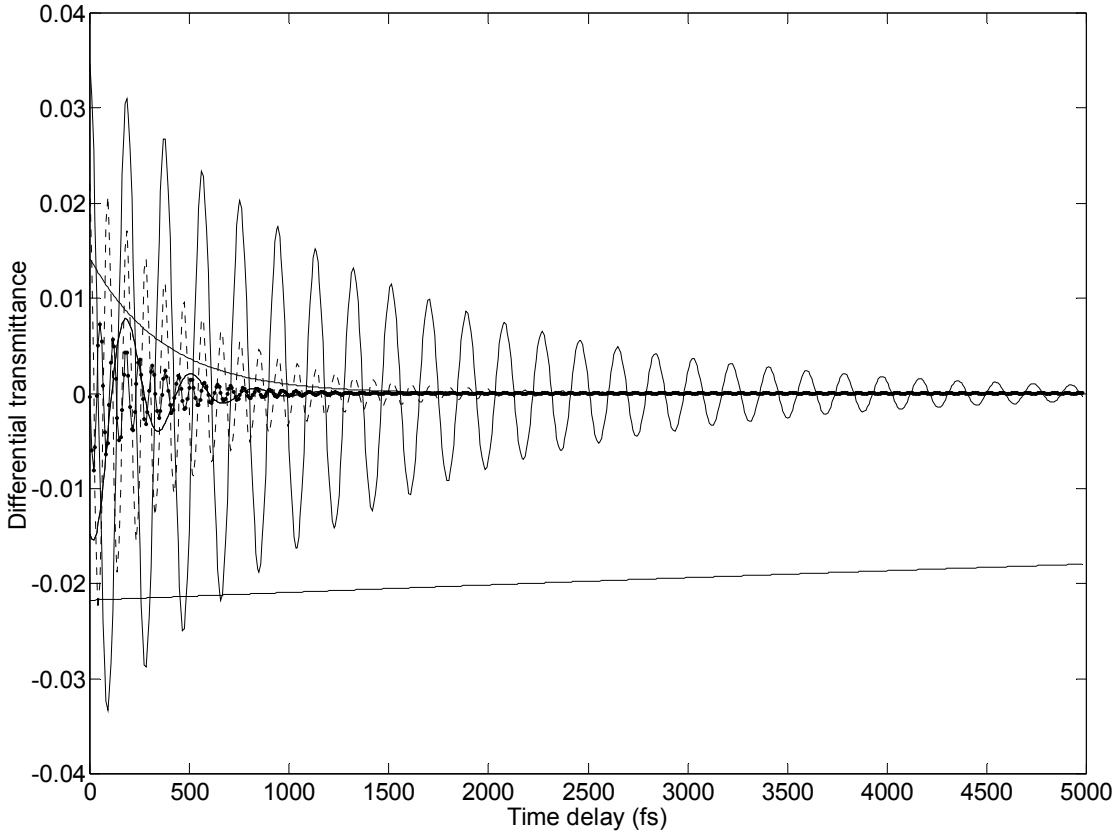

Figure 4.2: The individual components of the LPSVD for the degenerate 830 nm PtBr probe data in Figure 4.1. The component parameters are listed in Table. 4.1. (Reprinted with permission from Dexheimer, S. L., A. D. Van Pelt, J. A. Brozik, and B. I. Swanson, Journal of Physical Chemistry A, 2000. **104**(18): pp. 4308-4313. Copyright 2000, American Chemical Society.)

	Freq. (cm^{-1})	τ (fs)	ϕ (deg)	Amplitude
decay	0	26000	…	0.022
formation	**0**	**370**	…	0.014
excited state	**103**	**240**	149	0.0085
fundamental symmetric stretch	176	1300	9	0.018
second harmonic	351	510	17	0.012
third harmonic	510	210	80	0.0043

Table 4.1: Parameter results of the LPSVD for the time-resolved differential transmittance measurements of PtBr in Figure 4.1.

Nondegenerate pump-probe measurements were carried out to determine the evolution of the ~ 110 cm^{-1} component as a function of probe wavelengths outside the IVCT transition but within the red-shifted self-trapped exciton absorption band. Time-resolved differential transmittance of PtBr taken at a series of probe wavelengths, selected from a compressed broadband femtosecond white light continuum, is plotted in Figure 4.3(a).

Evolution of the wavepacket in the excited state is seen in the dependence of the phase of the ~ 110 cm^{-1} component with respect to the detection wavelength. Since the 830 nm probe wavelength falls within the pump spectrum, the wavepacket is probed in the Franck-Condon region, with an initial phase near 180°. As the probe wavelength sweeps from 830 nm to 940 nm, the wavepacket moves from nearly one classical turning point to the other. This is seen from the progression of the phase from 155° for 830 nm to 14° for 940 nm [1]. This shift in phase reflects the shift of the induced absorbance to longer wavelengths as the wavepacket propagates in the excited state.

Two components are assigned to the excited state response: (1) the ~ 110 cm^{-1} oscillation, reflecting the lattice motion associated with the self-trapping, and (2) the formation component, which represents the transition of the population between the free and self-trapped state. The sum of these two components assigned to the excited state, extracted from the LPSVD, is plotted in Figure 4.3(b).

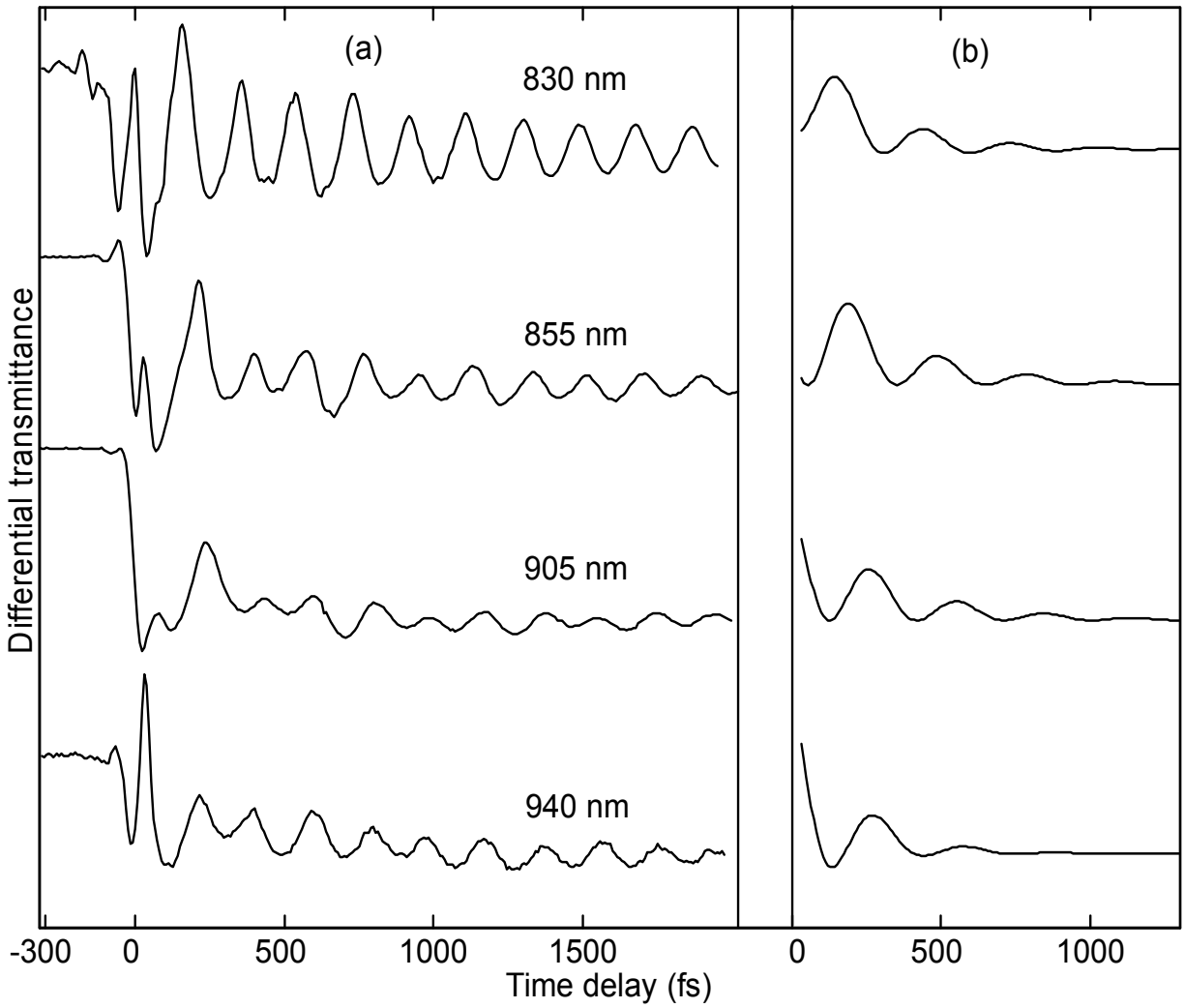

Figure 4.3: (a) The nondegenerate pump-probe PtBr data excited with a 35 fs pulse centered at 800 nm and probed at four detection wavelengths (830 nm, 855 nm, 905 nm, and 940 nm). (b) The sum of the low frequency and exponential formation component (assigned to the excited state response) for each probe wavelength obtained from the LPSVD results. (Reprinted with permission from Dexheimer, S. L., A. D. Van Pelt, J. A. Brozik, and B. I. Swanson, Physical Review Letters, 2000. **84**(19): pp. 4425-4428. Copyright 2000, American Physical Society.)

A complementary approach has detected excited state wavepacket motion in $[Pt(en)_2Br_2][Pt(en)_2]\cdot(ClO_4)_4$ at ~ 110 cm^{-1} (with a period of ~ 300 fs) measured using time-resolved photoluminescence [12,13]. In the first of these papers [12], Shinichi Tomimoto et al. assigned the motion to the wavepacket in the self-trapped exciton potential, while in the latter paper [13] they state that this motion is responsible for the "triggering [of] the localization of the electronic wavefunction and for energetic stabilization of the localized state". Their measured response in PtBr(en) appears consistent with the studies presented in this dissertation, aside from the model-dependent shift in the time axis introduced in the initial time-resolved photoluminescence measurements in Reference [12].

4.2 PtI Data and Analysis

Time-resolved measurements were carried out by the author on $[Pt(en)_2I_2][Pt(en)_2]\cdot(ClO_4)_4$ (or PtI) using the optical pump-probe apparatus. A fixed pump and a variable probe path length provide a time delay between the pulses. The differential transmittance was measured using lock-in amplification. (The details of the experimental setup are presented in Section 3.1.) A 1 kHz Ti:sapphire regenerative amplifier (discussed in Section 3.2.1) produces optical pulses 35 fs in duration centered at 800 nm, which excites the IVCT transition. The transmission was probed with a compressed white light continuum, generated by focusing a portion of the amplifier beam into a 2 mm sapphire plate. Figure 4.4 shows the time-resolved differential transmittance of PtI with an induced absorbance that is modulated by wavepacket oscillations initiated by impulsive excitation.

The data were analyzed using both LPSVD [6] and nonlinear least squares fitting method (NLLS) [14] using equation 4.1. An overview of the NLLS is present in Appendix B. The

advantage of NLLS over LPSVD is the ability to constrain the number of components in the model, fit multiple data sets simultaneously, and fix select parameters. The disadvantage of using NLLS over LPSVD is that the algorithm is more computationally intensive and requires a careful choice of initial values for the parameters. The initial values were obtained by analyzing the data using the LPSVD method. The results of the fitted data in Figure 4.4 are shown in Table 4.2, while the component plots extracted by NLLS fits are shown in Figure 4.5.

One of the key difficulties of the analysis is the extraction of the excited state oscillation from the PtI signal since the vibration has a frequency close to the ground state symmetric stretch, for reasons discussed in Section 4.5. This problem is exemplified in the fast Fourier transform (FFT) [15] of the PtI measurement (after long term exponential decay and formation components were extracted) shown in Figure 4.6. The excited state contribution is not resolved from the peak of the fundamental ground state symmetric stretch vibration due to the two frequencies being in close proximity. The two close frequencies have relatively short dephasing times, even for the ground state, resulting in wider peaks, further compounding the problem. Although the peaks are not fully resolved in the FFT, LPSVD and NLLS can successfully extract components.

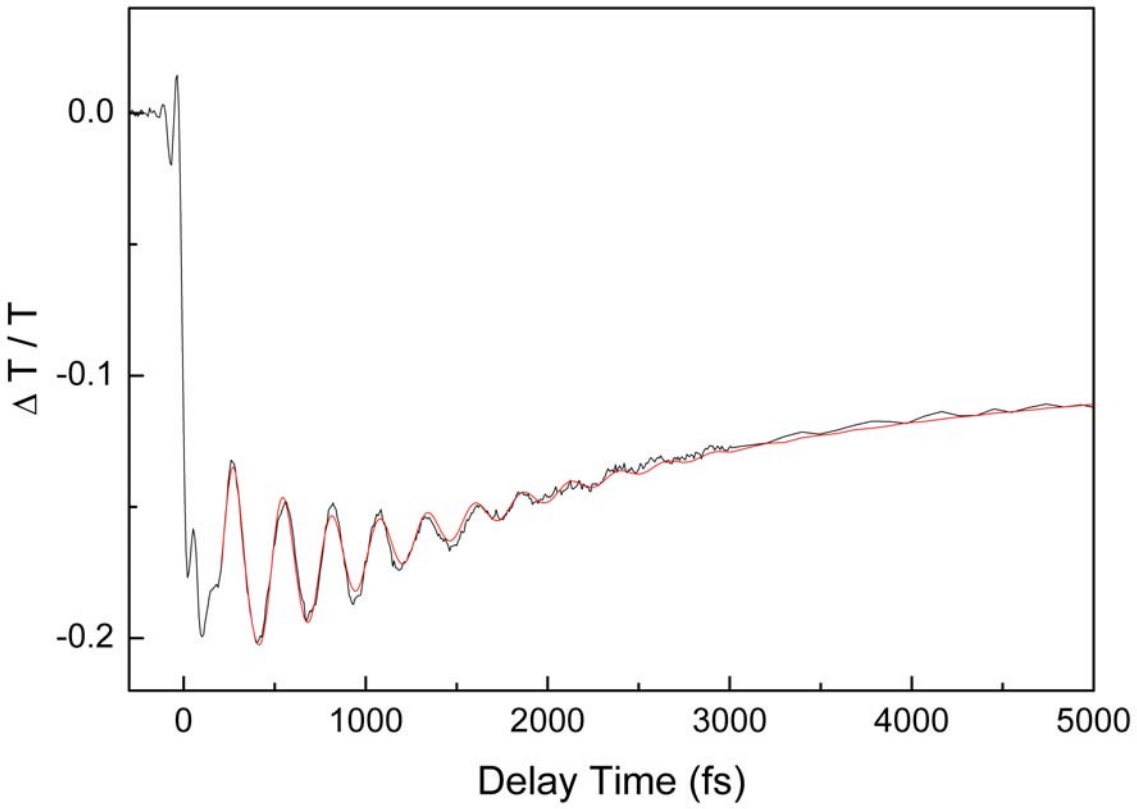

Figure 4.4: Comparison of the time-resolved differential transmittance of PtI (in grey) with a NLLS fit to the multi-component model (in red) of Equation 4.1. In the nondegenerate pump-probe measurement, PtI was excited with a 35 fs pulse centered at 800 nm and probed with a compressed continuum at a detection wavelength of 940 nm.

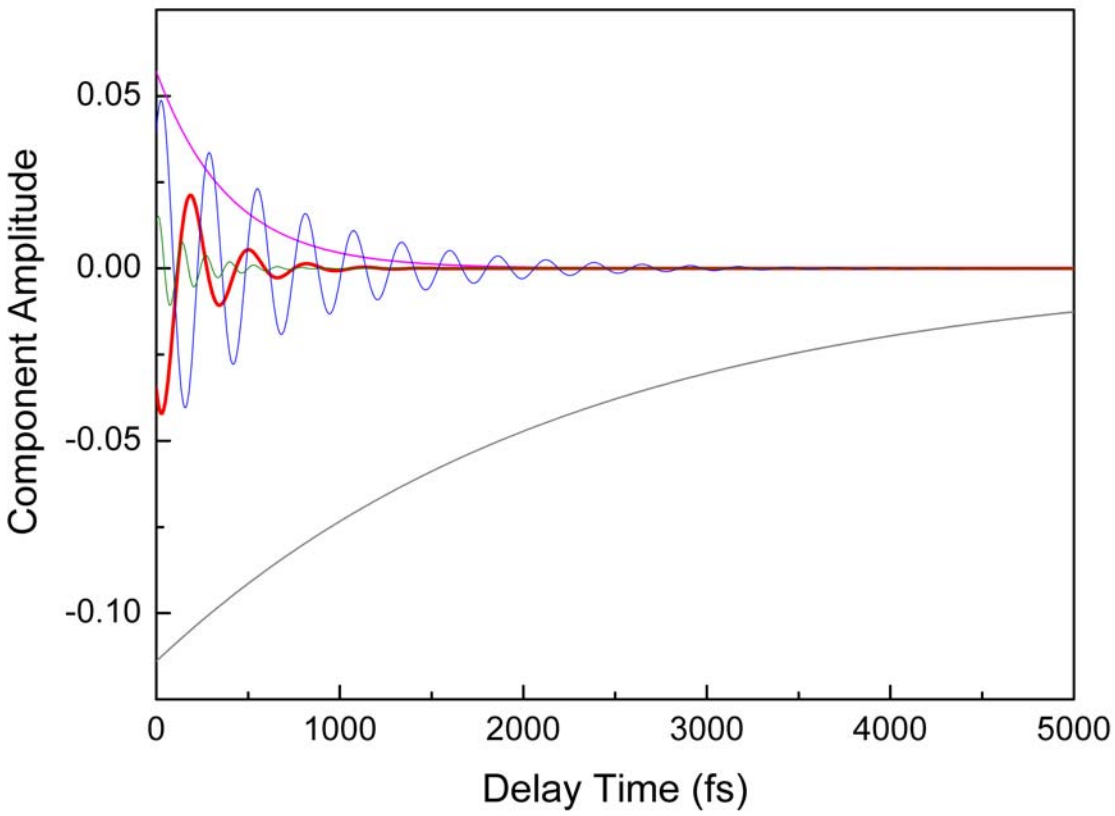

Figure 4.5: Component plots determined by NLLS of the PtI data (in Figure 4.4) at a detection wavelength of 940 nm. Contributing to the response are two zero frequency components (gray and magenta), a low frequency component at 106 cm^{-1} (red), the ground state symmetric stretch at 127 cm^{-1} (blue), and the second harmonic 254 cm^{-1} (green).

	Frequency (cm^{-1})	τ (fs)
decay	0	
formation	**0**	**390**
low	**106**	**230**
fundamental symmetric stretch	127	700
second harmonic	254	190

Table 4.2: Parameter results from the NLLS for the time-resolved differential transmittance measurement of PtI in Figure 4.4.

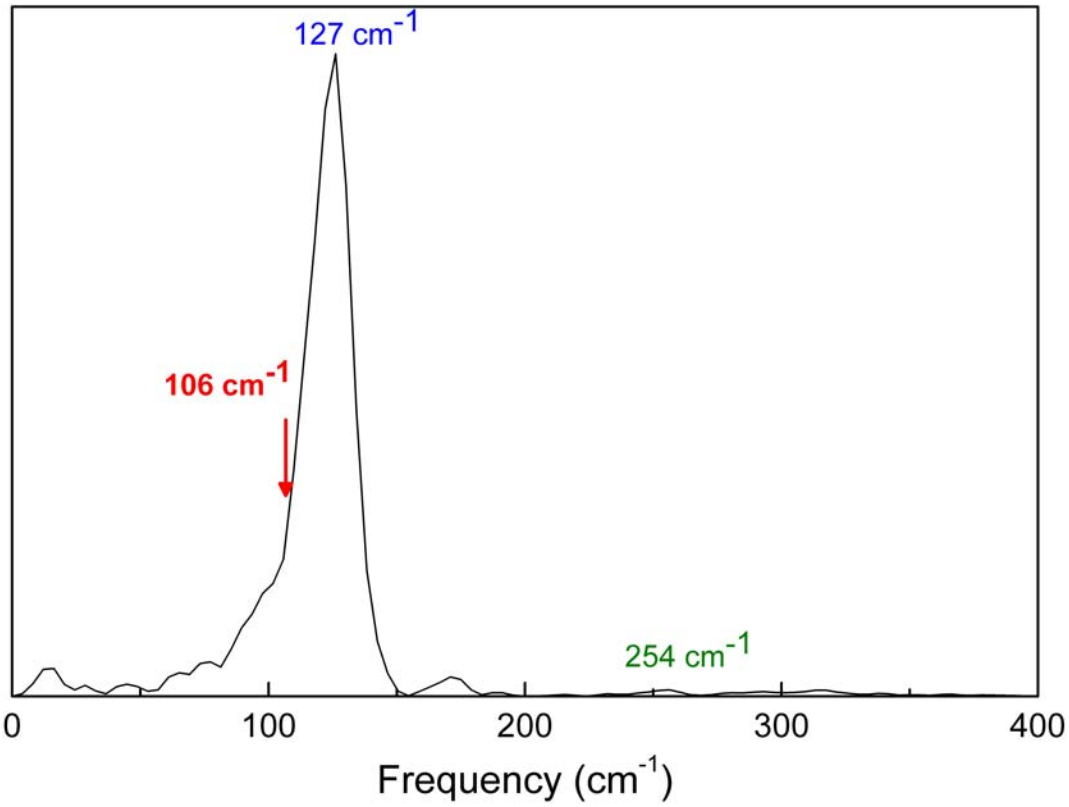

Figure 4.6: The Fourier power spectrum of the oscillatory part of wavelength-resolved differential transmittance measurement of PtI in Figure 4.4.

4.3 Excitonic Self-Trapping in PtI

The interpretation of the impulsive excitation measurements of PtI parallels that of PtBr laid out at the beginning of the chapter. The spectroscopic signatures of the self-trapped exciton dynamics have been observed in PtI. The motion of the excited state wavepacket is the origin of the strongly damped low frequency component at 106 cm^{-1} seen in the pump-probe measurement but absent from the Raman spectrum. Accompanying this vibration is the red-shifted exciton absorbance appearing on the time scale of ~ 400 fs, consistent with a rapid barrierless transition from the free to the self-trapped state in one-dimension. The onset of the fast formation is comparable to a single vibrational period of the low frequency vibration.

The ground state symmetric stretch vibration at 127 cm^{-1} (and the second harmonic) is due to the resonantly enhanced stimulated impulsive Raman process. This frequency is consistent with the symmetric stretch mode seen in the Raman spectrum [4,9].

Atsushi Sugita et al. measured the time-resolved transient absorption of PtI(en) pumped at 600 nm [16], high in the IVCT energy, and reported frequencies at 107 cm^{-1} and 124 cm^{-1} but assigned the first to the ground state process and the second to the excited state process. This assignment is inconsistent with ground state Raman studies of PtI(en) [4,9] and the observed frequency shift between the excited state motion and the ground state symmetric stretch mode of the PtX(en) series [1,2]. (The nature of this frequency shift is discussed in Section 4.6.)

4.4 Detection Wavelengths Dependence

Time-resolved differential transmittance of PtI at three detection wavelengths using a nondegenerate pump-probe configuration is shown in Figure 4.7. The data was analyzed using both LPSVD [6] and nonlinear least squares fitting method (NLLS) [14] using equation 4.1.

Using the NLLS, all three data sets were fitted simultaneously, where all values were "floated" (i.e., all values were allowed to vary to minimize Chi^2), while select "shared" parameters were constrained to be the same value for each trace in the global fit. Parameters in the global fit with a functional dependence on probe energy (e.g., amplitude and phase) were floated independently in each trace, while parameters expected to be independent of probe energy (e.g., frequency and dephasing time) were shared. The NLLS global fits are shown in red in Figure 4.7.

NLLS global fit at the three probe wavelengths determined that the ground state frequency was 131 cm^{-1} and the excited state frequency was 114 cm^{-1}. The excited state motion damped rapidly with a dephasing time of 375 fs at the three detection wavelengths. The Raman spectrum, shown in Figure 4.8, shows a ground state symmetric stretch frequency consistent with the ground state frequency measured in Figure 4.7. The discrepancy between the symmetric stretch frequencies (seen in the cw Raman versus the time-resolved pump-probe measurement) is due to the frequency's strong dependence on excitation energy [4,9] and temperature [17]. The results of the NLLS global fit is consistent with the fast Fourier transforms (FFT) [15] of the PtI measurements (after long term exponential decay and formation components were extracted) shown in Figure 4.9.

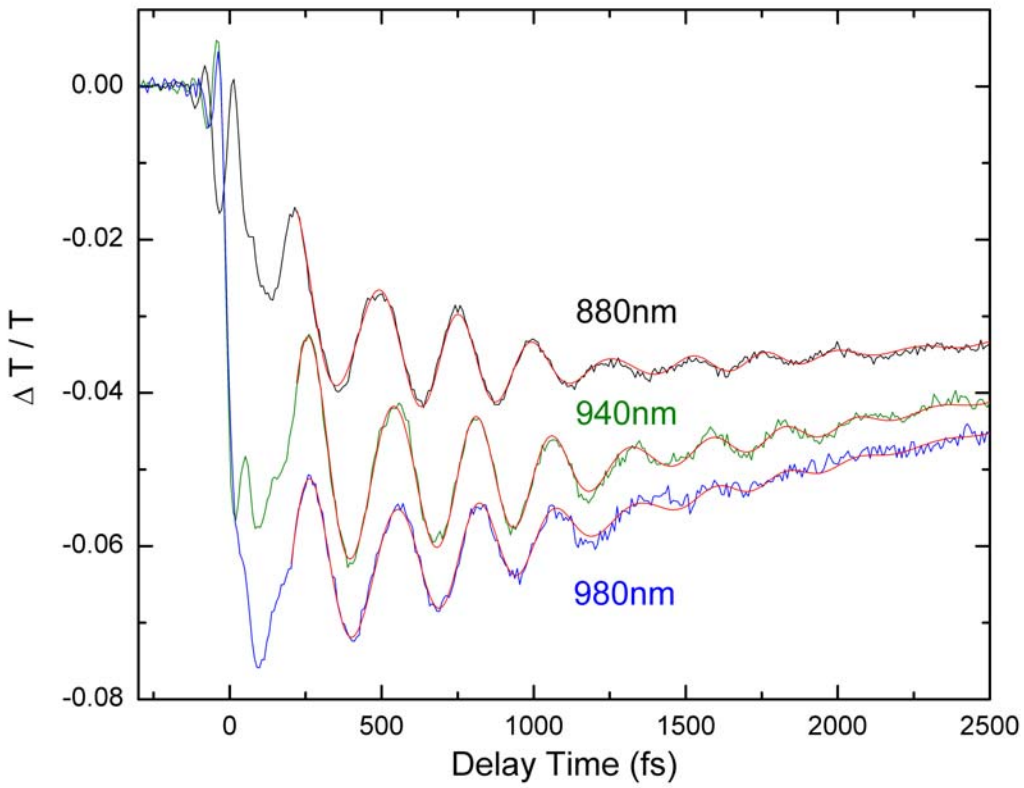

Figure 4.7: Comparison of the time-resolved differential transmittance of PtI with a NLLS global fit to the multi-component model (in red) of Equation 4.1. In the nondegenerate pump-probe measurement, PtI was excited with a 35 fs pulse centered at 800 nm and probed with a compressed white light continuum at detection wavelengths of **880 nm**, 940 nm, and 980 nm.

As discussed previously, the two components assigned to the excited state motion are the low frequency vibration and the corresponding formation component, the sum of which is plotted in Figure 4.10(b). This figure shows the phase dependence on detection wavelength revealing the evolution of the wavepacket in the excited state. Since the 880 nm probe wavelength falls outside the pump spectrum, the wavepacket is expected to have an initial phase less than 180°. As the probe wavelength sweeps from 880 nm to 980 nm, the wavepacket moves across the potential surface beyond its classical midpoint. This is seen from the progression of the phase from 128° for 880 nm to 63° for 980 nm shown in Table 4.3. This progression is an indication that as the wavepacket propagates in the excited state the induced absorbance shifts to longer wavelengths.

The appearance of a vibrational mode at ~ 170 cm^{-1} may be associated with a defect state since it does not show up in the Raman spectrum and the vibration shows no dependence on probe wavelength, that being a key excitonic signature. The LPSVD and NLLS determined that the amplitude of this mode is significantly smaller than both the ground state symmetric stretch and excited state oscillation. The wavelength-resolved studies presented in this section were conducted on an early batch of PtI crystals synthesized by Wayne Bushmann; where later batches of PtI crystals (the studies of which are discussed in Section 4.2) did not possess that ~ 170 cm^{-1} component.

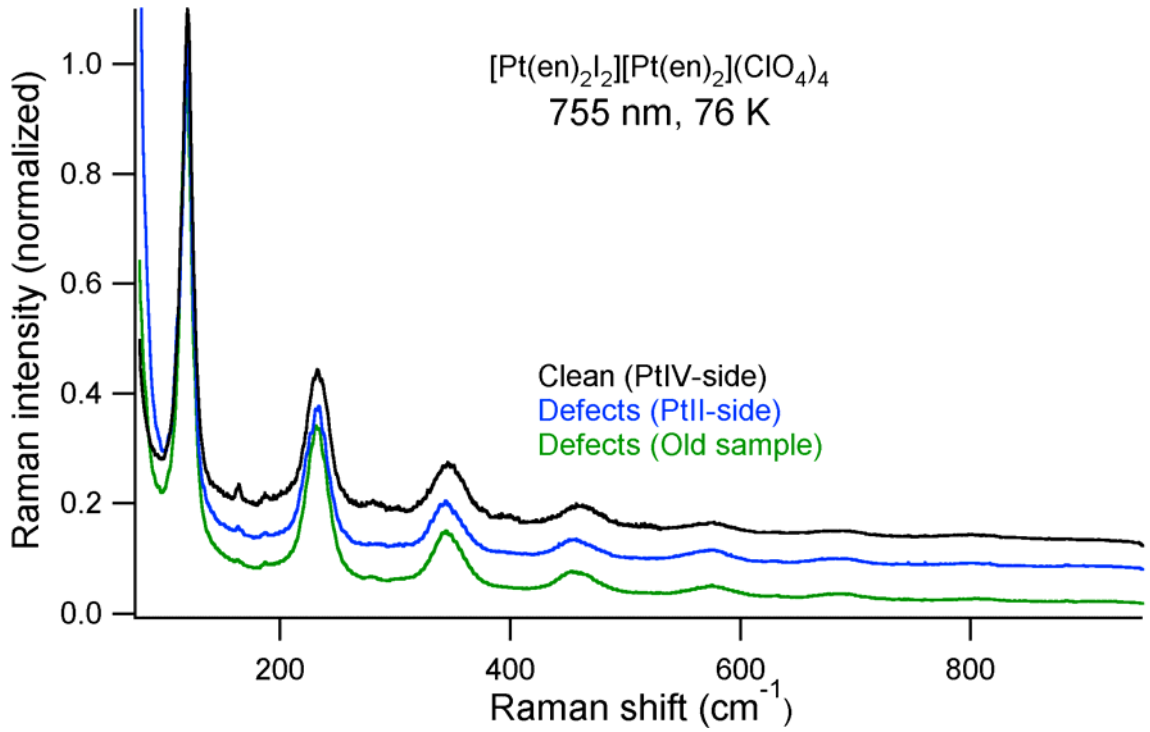

Figure 4.8: Low temperature (76 K) Raman spectra of $[Pt(en)_2I_2][Pt(en)_2]\cdot(ClO_4)_4$ excited at 755 nm. The top trace is of a "clean" sample while the bottom two traces were samples with defects. The author received the "clean" samples. (Provided by Wayne Bushmann)

Excited State Parameter Results NLLS Global Fit

		Shared Globally		Varied Independently	
detection wavelength		Frequency (cm^{-1})	τ (fs)	ϕ (deg)	Amplitude
	formation	0	415	…	0.024
880 nm	**excited state**	**114**	**375**	**128**	0.009
	formation	0	415	…	0.021
940 nm	**excited state**	**114**	**375**	**83**	0.020
	formation	0	415	…	0.009
980 nm	**excited state**	**114**	**375**	**63**	0.018
	decay	0	> 5000	…	0.043
880 nm	symmetric stretch	131	650	24	0.012
		167	630	57	0.004
	decay	0	> 5000	…	0.062
940 nm	symmetric stretch	131	650	-64	0.018
		167	630	-64	0.004
	decay	0	> 5000	…	0.072
980 nm	symmetric stretch	131	650	-77	0.012
		167	630	-65	0.004

Table 4.3: The top of the table presents the excited state parameter results from the NLLS global fitting of the time-resolved differential transmittance measurements of PtI in Figure 4.10(a). The bottom portion of the table reports all other parameters. The excited state parameter results are plotted in Figure 4.10(b).

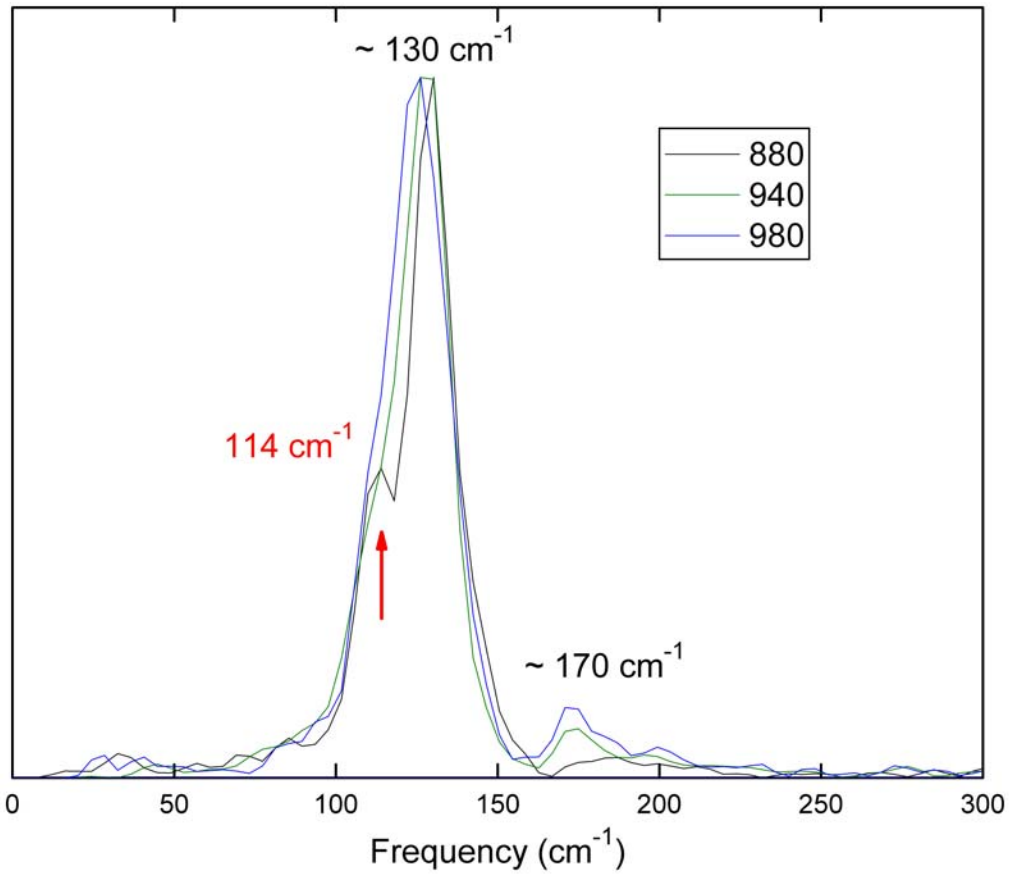

Figure 4.9: The Fourier power spectra of the oscillatory part of wavelength-resolved differential transmittance measurements of PtI in Figure 4.7.

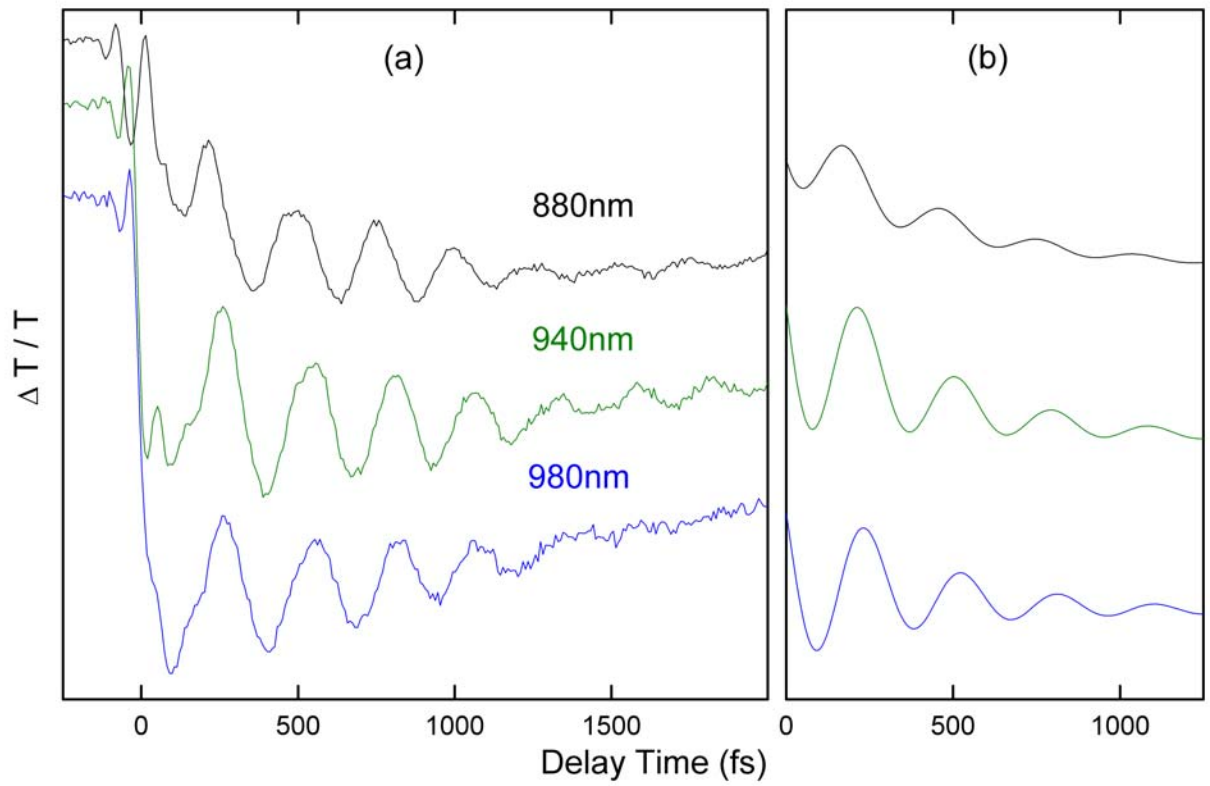

Figure 4.10: (a) The nondegenerate pump-probe PtI data taken at three detection wavelengths. (b) The sum of the low frequency and exponential formation component for each probe wavelength obtained from the NLLS global fitting results.

4.5 Further Studies

The impulsive excitation measurements conducted by the author have successfully identified the self-trapping dynamics in the weak electron-phonon coupled system, PtI. However, there are a number of issues that complicate measurements done on this complex. First, the PtI complex is excited with a pump pulse centered at 800 nm, which is at an energy high in the IVCT band. Pumping high in the IVCT band can directly create free electrons and holes, which can relax to form polarons, and can also lead to higher energy relaxation of the free exciton to form solitons (in addition to the self-trapped exciton) [18-20]. These structures have their own broad characteristic absorption bands which can overlap the self-trapped exciton absorption. Therefore, these non-exciton species can contribute to the pump-probe responses complicating the measurements and interpretation. Additional measurements at longer pump wavelengths are presented in Section 4.5.1, below. Second, in PtI the excited state vibration has a frequency close to the ground state symmetric stretch and both frequencies have relatively short dephasing times. Additional measurements at low temperature, which investigate the possibility of improved frequency resolution of the oscillatory components, are presented in Section 4.5.2, below.

Variation in the preparation and quality of the PtI crystals may lead to variations in the properties; for example, the frequency of the Raman symmetric stretch mode. This complication is further compounded by the dependence of symmetric stretch frequency on excitation energy [4,9]. Considering the net sum of the data obtained from the PtI samples, two types of signals were obtained. One group of results possessed all of the components discussed previously and typically had excellent signal to noise with large modulations of the induced absorption at a ground state frequency of ~ 130 cm^{-1}. A second group of measurements had a decay component in place of a formation and was always found to have poor signal to noise. The analysis of this

second group produced varying ground state frequencies, often much higher than 130 cm^{-1}. It is likely that the second group of measurements has contributions from defect states based on the poor optical quality at those particular sample locations. Nonetheless, the self-trapping dynamics have been unequivocally identified in PtI(en).

This section is organized as follows. First are presented PtI measurements pumped at energies lower than 800 nm, followed by low temperature PtI measurements.

4.5.1 Excitation of PtI with a 950 nm Pump Pulse

To address the complication of pumping high in the IVCT energy, measurements were taken with a pump pulse centered at 950 nm generated from a single-stage blue pumped noncollinearly phase matched optical parametric amplifier (NOPA) configured for an infrared signal pulse [21]. In the NOPA, a blue pump pulse and a continuum seed pulse are overlapped in a BBO crystal (where only the infrared portion of the continuum is used by inserting an 850 nm long pass filter after the continuum output). The timing between the pump and probe pulse and the tilt of the BBO crystal is adjusted for a (NOPA output) signal pulse centered at 950 nm.

In the degenerate measurements of PtI, the output of the NOPA passes through a beamsplitter to generate both the pump and probe pulse, centered at 950 nm with a duration of 35 fs. Probing (after transmission through PtI) on the red side of the pulse showed even larger wavepacket oscillations as compared to when pumped at 800 nm, as shown in Figure 4.11. The probe pulse was wavelength-resolved after transmission through the sample using a monochromator. The data were analyzed using both LPSVD [6] and nonlinear least squares fitting method (NLLS) [14] using equation 4.1. The initial values were obtained by analyzing the

data using the LPSVD method. The results of the fitted data in Figure 4.11 are shown in Table 4.4, while the component plots extracted by NLLS fits are shown in Figure 4.12.

Using a 950 nm pump, the same signal components with similar dephasing times were seen, as was the case with the 800 nm pump measurements. The motion of the excited state wavepacket is the origin of the strongly damped low frequency component at 116 cm^{-1} seen in the pump-probe measurement but absent from the Raman spectrum. Accompanying this vibration is the red-shifted exciton absorbance appearing on the time scale of ~ 500 fs, consistent with a rapid barrierless transition from the free to the self-trapped state in one-dimension. The onset of the fast formation is comparable to a single vibrational period of the low frequency vibration. The ground state symmetric stretch vibration at 122 cm^{-1} (and the second harmonic) is due to the resonantly enhanced stimulated impulsive Raman process. This shift in the ground state frequency from 122 cm^{-1} (950 nm pump) to 127 cm^{-1} (800 nm pump) is consistent with the dependence of the ground symmetric stretch frequency with excitation energy seen in Raman measurements [4,9].

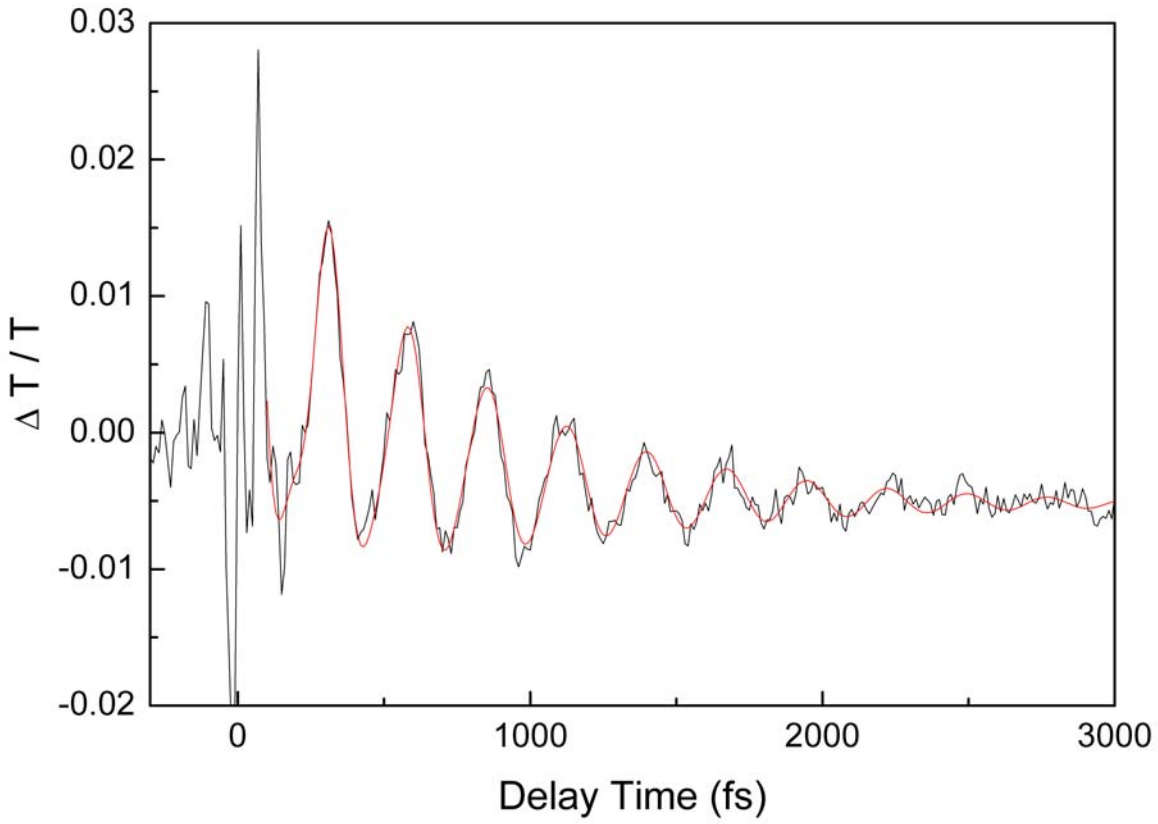

Figure 4.11: Comparison of the time-resolved differential transmittance of PtI (in grey) with a NLLS fit to the multi-component model (in red) of Equation 4.1. In the degenerate pump-probe measurement, PtI was excited with a 35 fs pulse centered at 950 nm and probed with the same pulse at a detection wavelength of 970 nm. The probe pulse was wavelength-resolved after transmission through the sample using a monochromator.

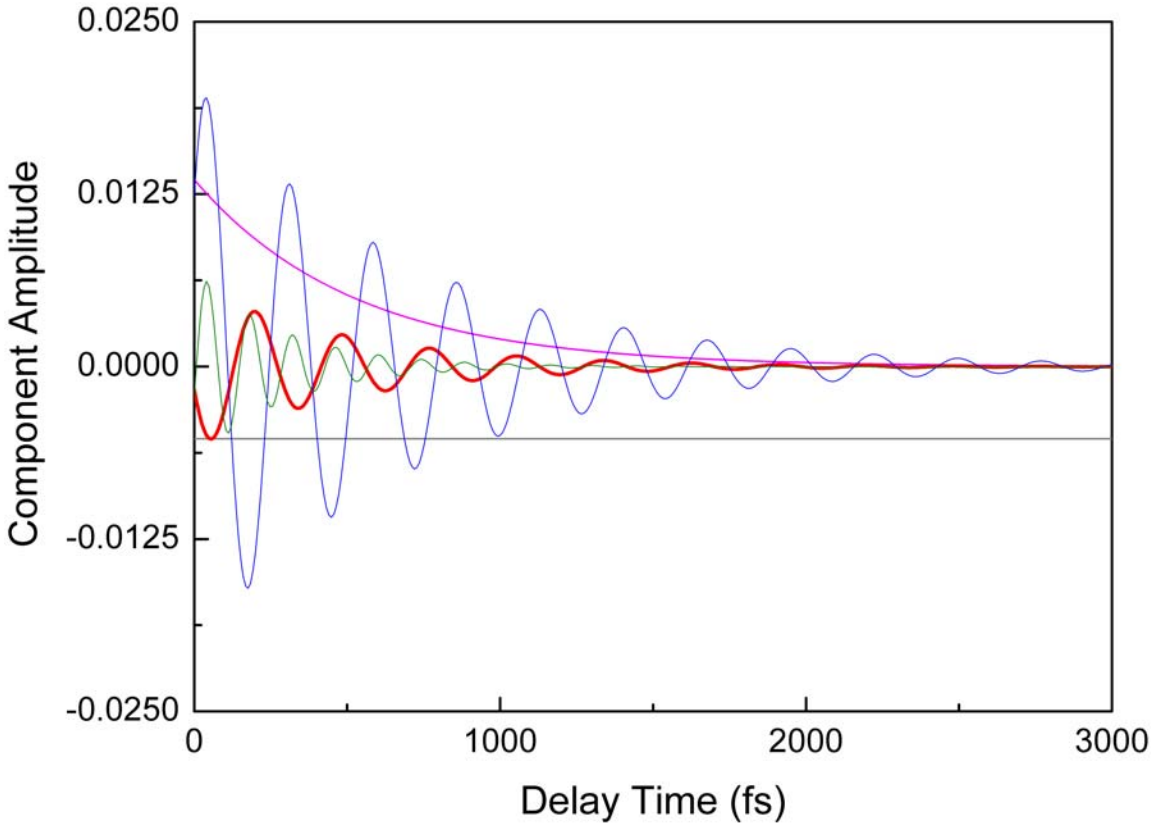

Figure 4.12: Component plots determined by NLLS of the PtI data (in Figure 4.11) at a detection wavelength of 970 nm. Contributing to the response is a constant offset (gray), a zero frequency component (magenta), a low frequency component at 116 cm^{-1} (red), the ground state symmetric stretch at 122 cm^{-1} (blue), and the second harmonic 238 cm^{-1} (green).

	Frequency (cm^{-1})	τ (fs)
formation	**0**	**520**
excited state	**116**	**500**
fundamental symmetric stretch	122	700
second harmonic	238	280

Table 4.4: Parameter results from the NLLS for the time-resolved differential transmittance measurement of PtI in Figure 4.11.

4.5.2 PtI Measurements at Low Temperature

Measurements were carried out at low temperature to investigate the possibility of improving the frequency resolution of the oscillatory components. This difficulty is due to the ground and excited state vibration being close in frequency and having relatively short dephasing times, as discussed at the end of Section 4.2. At low temperature we expect a longer dephasing time for the ground state vibration [17]. Low temperature nondegenerate pump-probe measurements of PtI were taken at 77 K (using liquid nitrogen) and at 40 K (using liquid helium) using an 800 nm 35 fs pump and a compressed broadband femtosecond white light continuum probe. Unfortunately, the low temperature time-resolved differential transmittance measurements on PtI did not show substantially increased dephasing times for either the ground state or excited state oscillatory components in this complex, unlike the changes reported in the low temperature measurements on PtBr reported in Chapter 6. No further frequency resolution was achieved at low temperature in PtI.

4.6 Self-Trapping in the PtX(en) Complexes

A consistent mechanism for the self-trapping dynamics has been identified in the PtX(en) series. From the strong to weak electron-phonon coupling cases, the self-trapped exciton forms on the time scale of a single vibrational period. Along with this formation is a rapidly dephasing excited state motion.

The electron-phonon coupling strength dependence on self-trapping dynamics shows some striking correlations. Table 4.5 details the frequency shift of the observed excited state oscillation relative to the ground state symmetric stretch, as a function of complex substitution and lattice distortion, ρ (see Section 2.3). Interestingly, the PtX series show a direct correlation

between the ratio of the vibrational frequencies and the degree of electronic delocalization. The more delocalized the system, the less of a frequency shift observed. Since the frequency of the excited state motion is dependent on the charge distribution that results after the IVCT transition, the magnitude of the frequency shift is related to the charge distribution leading to the self-trapped exciton. Therefore, the less distorted the system is in the ground state, the smaller the relative difference in the charge distribution in the self-trapped state.

Since the symmetric stretch vibration is strongly coupled to the IVCT transition, the lattice motion that brings the system from the final state of the IVCT transition to the self-trapped state is expected to have contributions from the symmetric stretch. The excited state oscillations are expected to involve motion of the halides away from the ground state Peierls distorted positions to positions in the self-trapped state. However, such a large frequency shift of the excited state motion (e.g., at ~ 180 cm^{-1} in PtCl) as compared to the ground state symmetric stretch (e.g., at 315 cm^{-1} in PtCl) can not be accounted for by dispersion in the phonon mode [22], indicating that additional factors are contributing to the self-trapping dynamics. These may include frequency shifts due to changes in the charge distribution and coupling to acoustic modes.

	Cl	Br	I
ρ	0.743	0.828	0.890
excited state frequency	180 cm^{-1}	110 cm^{-1}	106 cm^{-1}
ground state frequency	315 cm^{-1}	175 cm^{-1}	127 cm^{-1}
ratio	0.57	0.63	0.83

Table 4.5: Ratio of mode frequencies correlated with halide substitution (X = Cl [2], Br [1], I) in the PtX(en) series. The ratio of the short to long Pt-X bond lengths (ρ) [17,23,24] provide a measure of the degree of structural distortion. These systems range from the highly distorted valence-localized PtCl(en) to the less distorted valence-delocalized PtI(en). PtBr(en) represents the intermediate case of moderate distortion and delocalization.

4.7 References for Chapter 4

1. Dexheimer, S., A. Van Pelt, J. Brozik, and B. Swanson, *Femtosecond vibrational dynamics of self-trapping in a quasi-one-dimensional system.* Physical Review Letters, 2000. **84**(19): pp. 4425-4428.

2. Van Pelt, A. and S. Dexheimer, *Ultrafast dynamics of excitonic self-trapping* in Ultrafast Phenomena XII, T. Elsaesser, S. Mukamel, M. Murnane, N. Scherer, Editors. 2000, Springer-Verlag. pp. 393-397.

3. Dexheimer, S., A. Van Pelt, J. Brozik, and B. Swanson, *Ultrafast vibrational dynamics in a quasi-one-dimensional system: Femtosecond impulsive excitation of the PtBr(en) mixed-valence linear chain complex.* Journal of Physical Chemistry A, 2000. **104**(18): pp. 4308-4313.

4. Buschmann, W., S. McGrane, and A. Shreve, *Chemical tuning of nonlinearity leading to intrinsically localized modes in halide-bridged mixed-valence platinum materials.* Journal of Physical Chemistry A, 2003. **107**(40): pp. 8198-8207.

5. Wada, Y., T. Mitani, M. Yamashita, and T. Koda, *Charge transfer exciton in halogen-bridged mixed-valent Pt and Pd complexes: Analysis based on the Peierls-Hubbard Model.* Journal of the Physical Society of Japan, 1985. **54**(8): pp. 3143-3153.

6. Wise, W., M. Rosker, G. Millhauser, and C. Tang, *Application of linear prediction least-squares fitting to time-resolved optical spectroscopy.* IEEE Journal of Quantum Electronics, 1987. **QE-23**(7): pp. 1116-1121; Giordano, A. and F. Hsu, *Least square estimation with application to digital and signal processing.* 1985, New York: John Wiley & Sons; Rao, C. and H. Toutenburg, *Linear models and least squares and alternatives. Springer series in statistics.* 1995, New York: Springer-Verlag; Lay, D., *Linear algebra and its applications.* 1996, New York: Addison-Wesley; the LPSVD code employed by the author was modeled after the particulars in the following reference: Kumaresan, R. and D. Tufts, *Estimating the parameters of exponentially damped sinusoids and pole-zero modeling in noise*. IEEE Transactions on Acoustics, Speech and Signal Processing, 1982. **30**(6): 833-840; Implementation of the LPSVD uses Fortran subroutines from Linpack and Eispack.

7. Diels, J. and W. Rudolph, *Ultrashort laser pulse phenomena: fundamentals, techniques, and applications on a femtosecond time scale.* 1996, San Diego: Academic Press. chapters 5-9; C. Hirlimann, A. Ducasse, C. Rulliére, B. Couillaud, T. Amand, X. Marie, F. Salin, L. Sarger, J. Oberlé, M. Joffre, and A. Bonvalet, *Femtosecond laser pulses: Principles and experiments.* Rulliére, C., Editor. 1998, Germany: Springer. chapters 3.

8. Alfano, R., Q. Li, T. Jimbo, J. Manassah, and P. Ho, *Induced spectral broadening of a weak picosecond pulse in glass produced by an intense picosecond pulse.* Optical Letters, 1986. **11**(10): pp. 626-628; first observation of cross-phase modulation.

9. Clark, R., *Raman and resonance Raman spectroscopy of linear chain complexes,* in *Advances in infrared and Raman spectroscopy,* R. Clark and R. Hester, Editors. 1984, Wiley. pp. 95-132.

10. Scott, B., S. Love, G. Kanner, S. Johnson, M. Wilkerson, M. Berkey, B. Swanson, A. Saxena, X. Huang, and A. Bishop, *Control of selected physical properties of MX solids: an experimental and theoretical investigation.* Journal of Molecular Structure, 1995. **356**: pp. 207-229.

11. Love, S., L. Worl, R. Donohoe, S. Huckett, and B. Swanson, *Origin of the fine structure in the vibrational spectrum of* $[Pt(C_2H_8N_2)_2][Pt(C_2H_8N_2)_2Cl_2](ClO_4)_4$*: Vibrational localization in a quasi-one-dimensional system.* Physical Review B, 1992. **46**(2): pp. 813-816; Huang, X., A. Saxena, A. Bishop, L. Worl, S. Love, and B. Swanson, *Segment length dependence of Raman frequency and optical properties in mixed-halide* $PtCl_xBr_{1-x}$ *chain solids.* Solid State Communications, 1992. **84**(10): pp. 957-961; Huckett, S., R. Donohoe, L. Worl, A. Bulou, C. Burns, and B. Swanson, *On the origin of the resonance Raman* ν_1 *dispersion and fine structure of PtBr.* Synthetic Metals, 1991. **41-43**: pp. 2773-2776.

12. Tomimoto, S., S. Saito, T. Suemoto, K. Sakata, J. Takeda, and S. Kurita, *Observation of the wave-packet oscillation during the exciton self-trapping process in a quasi-one-dimensional halogen-bridged Pt complex.* Physical Review B, 1999. **60**(11): pp. 7961- 7965.

13. Tomimoto, S., S. Saito, T. Suemoto, J. Takeda, and S. Kurita., *Ultrafast dynamics of lattice relaxation of excitons in quasi-one-dimensional halogen-bridged platinum complexes.* Physical Review B, 2002. **66**(15): pp. 155112-155121.

14. Nonlinear least squares fits were obtained using the software package Origin® Pro 7.0 (Copyright © 1991-2001 Origin Lab Corporation). The nonlinear regression application is based on a Levenberg-Marquardt algorithm following a similar flow of control as the (popular) Minpack (Fortran) subroutines (employing the same algorithm) developed by J. More', B. Garbow, and K. Hillstromthe of Argonne National Laboratory. The specific details of this method can be found in the following two references; Levenberg, K., *A method for the solution of certain non-linear problems in least squares*. Quarterly of Applied Mathematics, 1944. **2**: pp. 164-168; Marquardt, D., *An algorithm for least-squares estimation of nonlinear parameters*. Journal of the Society for Industrial and Applied Mathematics, 1963. **11**: pp. 431-441.

15. Cooley, J., and J. Tukey, *An algorithm for the machine calculation of complex Fourier series*. Mathematics of Computation, 1965. **19**(90): pp. 297-301; Bracewell, R., *The Fourier Transform and Its Applications: Electrical and Electronic Engineering Series*, 1978. New York: McCraw-Hill; Jean Baptiste Joseph Fourier formulated the trigonometric analysis in 1807 (59 years earlier, L. Euler introduced the cosine representation of an analytical function, which is a less general construction of the before mentioned theory). Even though the Fourier transform has been named in his honor, recent rigorous historical investigations indicate Carl Friedrich Gauss conceived of the mathematical theory well beforehand: Heideman, M., D.

Johnson, and C. Burrus, *Gauss and the History of the Fast Fourier Transform.* IEEE Acoustics, Speech, and Signal Processing Magazine, 1984. 1(4): pp. 14-21; Gauss, C., *Nachlass: Theoria interpolationis methodo nova tracata*. pp. 265-303, in *Carl Friedrich Gauss, Werke, Band 3*, Göttingen: Königlichen Gesellschaft der Wissenschaften, 1866. ("unpublished", circa 1805).

16. Sugita, A, T. Saito, H. Kano, M. Yamashita, and T. Kobayashi, *Wave packet dynamics in a quasi-one-dimensional metal-halogen complex studied by ultrafast time-resolved spectroscopy.* Physical Review Letters, 2001. **86**(10): pp. 2158-2161.

17. Huckett, S., B. Scott, S. Love, R. Donohoe, C. Burns, E. Garcia, T. Frankcom, B. Swanson, *Effects of temperature on the crystal and molecular structure of the mixed-valence linear chain $[Pt(en)_2][Pt(en)_2X_2][ClO_4]_4$ (X = Cl, Br).* Inorganic Chemistry, 1993. **32**: pp. 2137-2144.

18. Suzuki, M. and K. Nasu, *Nonlinear lattice-relaxation process of excitons in quasi-one-dimensional halogen-bridged mixed-valence metal complexes: Self-trapping, solitons, and polarons.* Physical Review B, 1992. **45**(4): pp. 1605-1611.

19. Mishima, A. and K. Nasu, *Nonlinear lattice relaxation of photogenerated charge-transfer excitation in halogen-bridged mixed-valence metal complexes. I. Soliton and self-trapped exciton.* Physical Review B, 1989. **39**(9): pp. 5758-5762.

20. Mishima, A. and K. Nasu, *Nonlinear lattice relaxation of photogenerated charge-transfer excitation in halogen-bridged mixed-valence metal complexes. II. Polaron channel.* Physical Review B, 1989. **39**(9): pp. 5763-5766.

21. Piel, J., M. Beutter, and E. Riedle, *20-50-fs pulses tunable across the near infrared from a blue-pumped noncollinear parametric amlifier.* Optics Letters, 2000. **25**(3): pp. 180-182.

22. Bulou, A., R. Donohoe, and B. Swanson, *Phenomenological description of the longitudinal vibrations of the quasi-one-dimensional solid PtCl: calculation of the valence defect frequencies.* Journal of Physics: Condensed Matter, 1991. **3**(12): pp. 1709-1726.

23. Clark, R., V. Croud, R. Wills, P. Bates, H. Dawes and M. Hursthouse, *Mixed-valence linear-chain complexes: X-ray structural characterization of a $Pd^{II}/Pd^{IV}Br_2$ chain and of three mixed-metal chains, $[NiPt(en)_4Cl_2]^{4+}$, $[PdPt(pn)_4Cl_2]^{4+}$ and $[NiPt(pn)_4Cl_2]^{4+}$, all as perchlorate salt.* Acta Crystallographica Section B: Structural Science, 1989. **45**: pp.147-152.

24. S. Love, S. Huckett, L. Worl, T. Frankcom, S. Ekberg, and B. Swanson, *Far-infrared spectroscopy of halogen-bridged mixed-valence platinum-chain solids: Isotope-substitution studies.* Physical Review B, 1993. **47**(17): pp. 11107-11123.

Chapter 5

Excited State Resonant Impulsive Raman Spectroscopy: Vibrational Properties of the Equilibrated Self-Trapped Exciton

In the impulsive excitation measurements detailed in Chapter 4, wavepacket motion associated with the excited state rapidly damped as the self-trapped exciton formed. Due to the rapid damping, information on the vibrational properties of the exciton is lost as it self-traps. Impulsive Raman measurements of the equilibrated self-trapped state, conducted by the author and presented in this chapter, have revealed the frequency of a characteristic vibrational mode of the self-trapped exciton in its equilibrated structure [1]. Measurement of this vibration has revealed new information on the physics of localization.

5.1 The Multi-Pulse Optical Setup

A multi-pulse vibrationally impulsive pump-probe measurement on $[Pt(en)_2Br_2][Pt(en)_2]\cdot(ClO_4)_4$ (or PtBr) was carried out using the Hurricane commercial femtosecond laser system which produces optical pulses 110 fs in duration centered at 800 nm (discussed in Section 3.2.2). An optical parametric amplifier (OPA) [2], tuned to a wavelength within the self-trapped exciton absorption (1.31 μm), generated a pump and probe pulse used to do an impulsive Raman measurement on the self-trapped exciton. In the OPA, a portion of the Hurricane output and a continuum seed pulse are overlapped in a BBO crystal where the timing between the pump and probe pulse and the tilt of the BBO crystal is adjusted for an OPA output signal pulse centered at 1.31 μm (see Section 3.2.2).

In these pump-pump-probe measurements two optical pump pulses were used:

(1) the initial pump pulse, 110 fs in duration centered at 800 nm (Figures 3.13 and 3.14), creates an exciton population in PtBr (see Chapter 4) [3,4] via excitation of the IVCT transition. The duration of the pulse is selected to generate only a relatively small wavepacket response.

(2) After a delay of 1 ps, a second pump pulse, 45 fs in duration centered at 1.31 μm (Figures 5.1 and 5.2), which is well outside the IVCT energy but within the absorption band of the self-trapped exciton, impulsively excites the self-trapped exciton population generated by the first pump pulse.

The equilibrated self-trapped exciton response is investigated via a degenerate pump-probe measurement of the excited state. The signal beam from the OPA, tuned to a center wavelength of 1.31 μm and compressed to a duration of 45 fs, passes through a beamsplitter to generate the (second) pump and probe pulses. After transmission through PtBr, the probe pulse is wavelength-resolved using a monochromator.

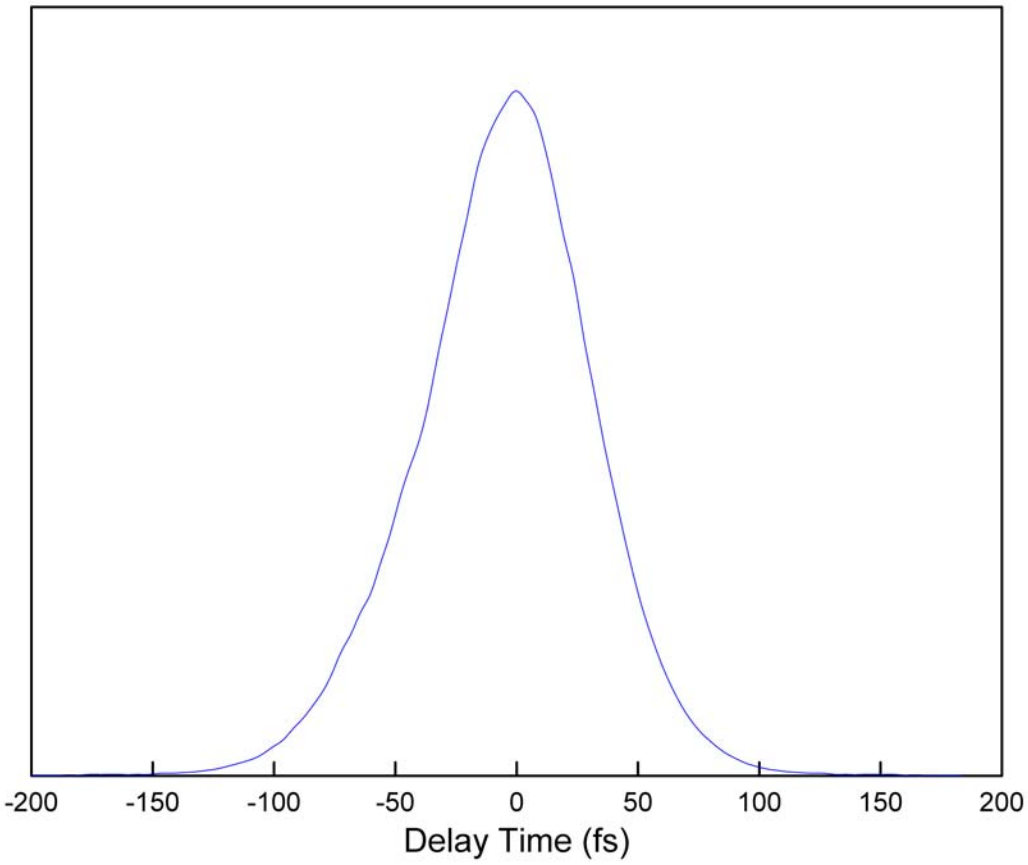

Figure 5.1: An autocorrelation of a 45 fs pulse out of the OPA tuned to 1.31 μm. The measurement was taken using a BBO crystal.

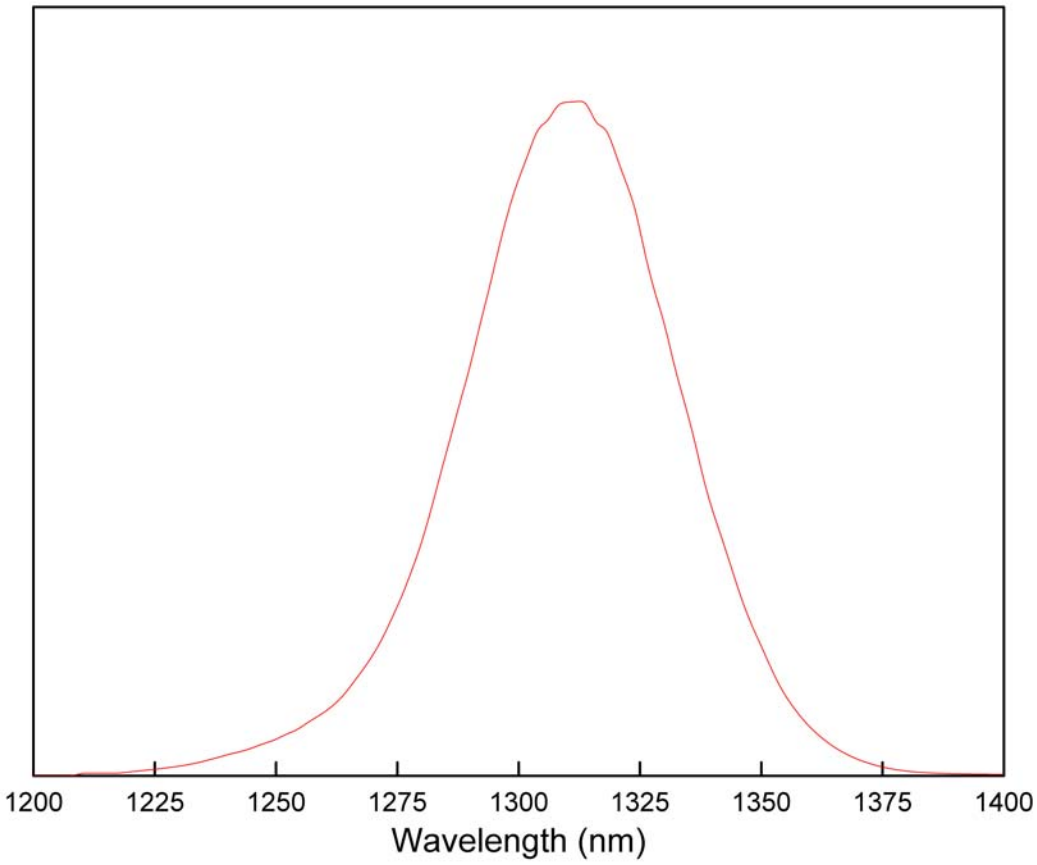

Figure 5.2: The spectrum of a pulse out of an OPA detailed in Section 3.2.2. The OPA spectrum is centered at 1.31 μm and has a FWHM of 52 nm.

The reasoning behind selecting a 1 ps duration between the first and second pump pulses is twofold: it ensures that the exciton has relaxed to the equilibrated structure since the self-trapped exciton forms in ~ 300 fs (see Section 4.1) and this duration allows for the small wavepacket response from the initial pump to decay away.

To carry out the measurements, a three arm pump-pump-probe apparatus was built with two independently adjustable arms, which provide a pump-pump-probe sequence of pulses at the sample with variable time delays. In the optical setup, all three pulses are focused to the same spot on the sample. The path length difference between the first pump pulse (at 800 nm), which has a fixed path length, and the second pump pulse (at 1.31 μm) is varied using a precision translation stage located in the second pump arm. The path length difference between the second pump (1.31 μm) and the probe beam is varied using a computer controlled translation stage located in the probe arm. As described in more detail below, double modulation allows for the detection of the response that is only due to double pump excitation. A simplified schematic of the apparatus is presented in Figure 5.3.

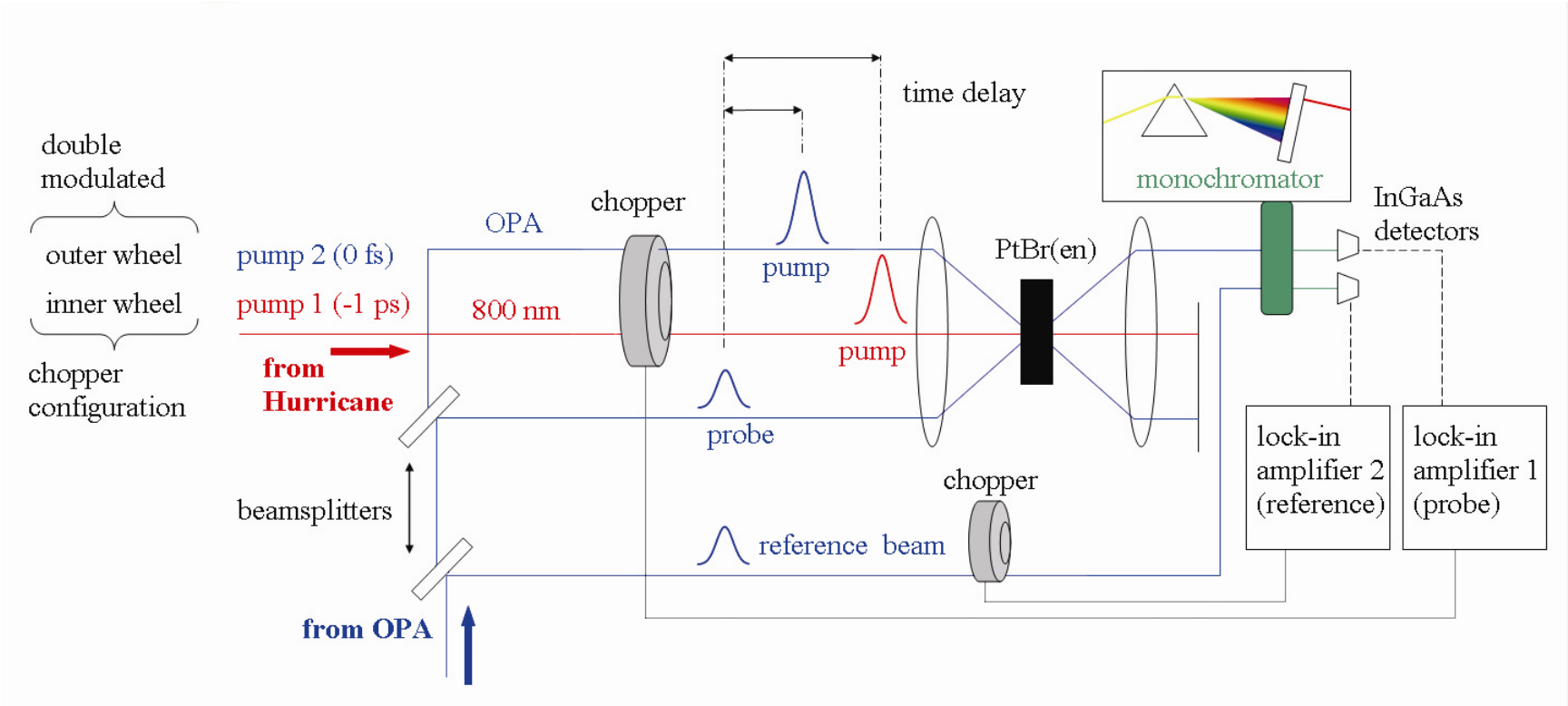

Figure 5.3: A simplified schematic of the apparatus used to carry out the pump-pump-probe technique.

The second pump and probe pulses are generated from an OPA, where a continuum seed and 800 nm pump pulse are mixed in a BBO crystal tuned to emit a signal pulse at 1.31 μm (see Section 3.2.2). The OPA pulse is compressed with a dispersive delay line constructed from a pair of fused silica prisms (see Section 3.1.6). Beamsplitters are used to generate an intense OPA pump pulse and a weak probe pulse (see Section 3.1.1). A second beamsplitter is used to generate a reference pulse for noise reduction and normalization, in the same manner as the single pump-probe measurements discussed in Section 3.1.2. Both the reference and the probe intensities, after passing through a monochromator (to select out a particular detection wavelength), were monitored using InGaAs detectors, which have an excellent response around 1.31 μm. A photograph of the pump-pump-probe apparatus is presented in Figure 5.4.

The wavepacket motion resulting from impulsive excitation of the equilibrated self-trapped exciton by the second pump pulse is detected as a function of time delay between the second pump and the probe pulse. Detection of the response originating from the excited state is achieved by simultaneously chopping both pump beams at different chopping rates and observing the probe intensity at the sum of the individual modulation frequencies using a lock-in amplifier. This detection scheme allows for the measurement of the vibrational response of the equilibrated self-trapped state since the measurement will be sensitive to only the differential changes originating from the excited state (i.e., those requiring the presence of both pump pulses) and will be insensitive to the individual pump responses.

Figure 5.4: The pump-pump-probe apparatus used to investigate the vibrational dynamics associated with equilibrated self-trapped state.

5.2 Excited-State Resonant Impulsive Raman Measurement

5.2.1 Pump-Pump-Probe Measurement

A representative pump-pump-probe measurement and analysis is presented in Figures 5.5 and 5.6 where the components of the response were determined using linear prediction analysis [5] and confirmed by nonlinear least squares fitting [6] of the data to a sum of exponentials and exponentially damped cosine waves given in Equation 4.1. The individual component parameters are detailed in Table 5.1. The measurement was carried out with a wavelength-resolved probe using a monochromator, and the detection wavelength for the measurement presented in Figure 5.5 was chosen on the red side of the probe pulse. Maximum amplitude of the impulsive Raman response is expected for detection wavelengths on the sides of the pulse spectrum. Double pump excitation reveals a new oscillatory component observed at 125 cm^{-1}, which is assigned to the equilibrated self-trapped exciton state as discussed in Section 5.2.3. Also present in the double pump response is an oscillation at the ground state symmetric stretch frequency. It can not be overstated that this component at 125 cm^{-1} is not present in the single pump measurements carried out at either 800 nm or 1.31 μm nor is it present in the ground state Raman spectrum. The single pump-probe measurements and analysis are detailed in the following section.

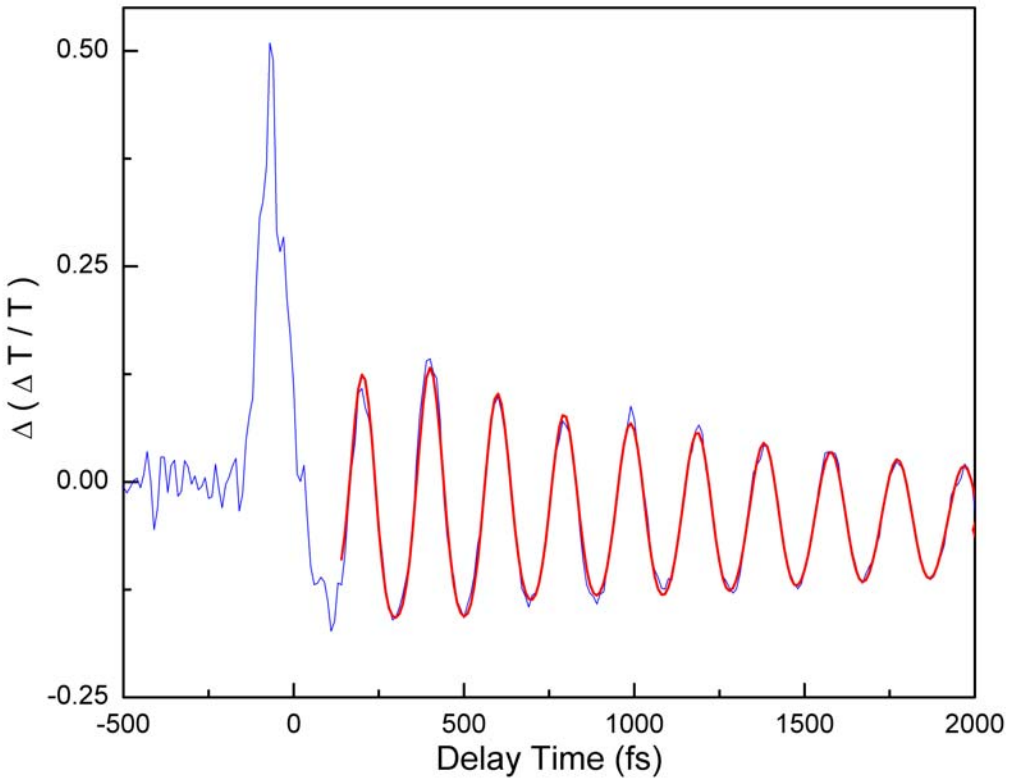

Figure 5.5: PtBr is pumped with two pulses: pump 1 at -1 ps, 800 nm, 110 fs pulse; pump 2 at 0 fs, 1.31 μm, 45 fs pulse. The vibrational coherence of the self-trapped state is investigated with a variable delay probe pulse at a detection wavelength of 1.33 μm, with a pulse width of 45 fs. The red trace represents a fit to the data using NLLS with parameters in Table 5.1. (Reprinted with permission from Morrissey, F. X. and S. L. Dexheimer, *Vibrational spectroscopy of nonlinear excitations via excited-state resonant impulsive Raman spectroscopy* in Ultrafast Phenomena XV, P. Corkum, D. Jonas, D. Miller, A. Weiner, Editors. 2007, Springer-Verlag. *in press*. Copyright 2007, Springer Science and Business Media.)

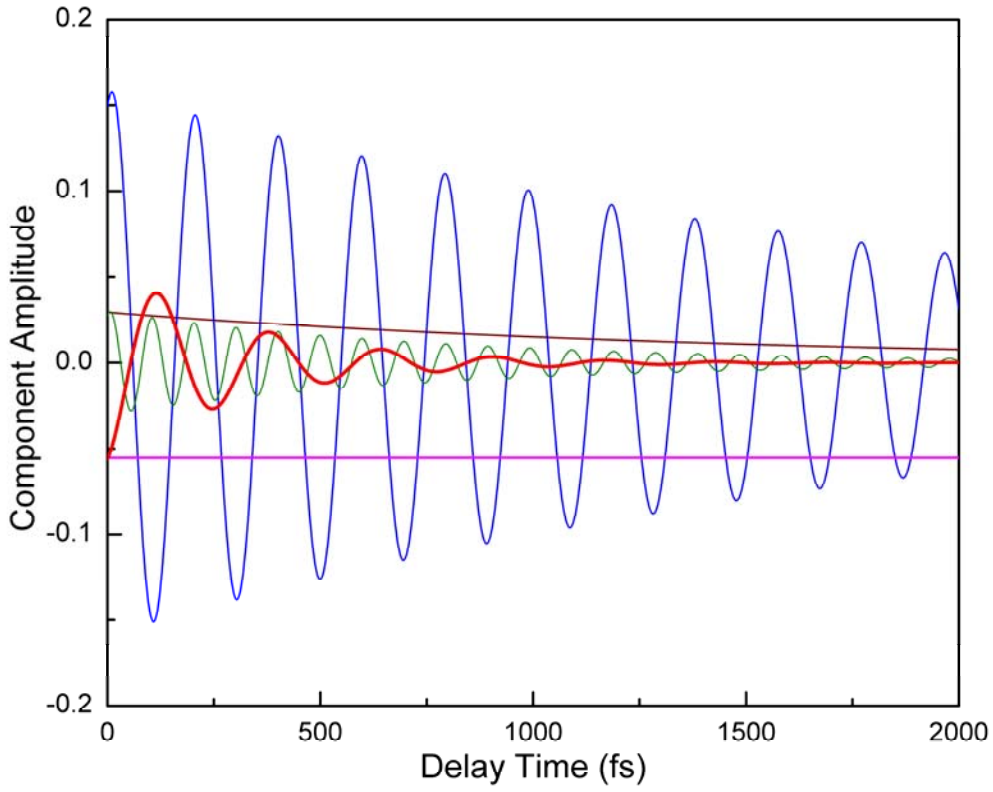

Figure 5.6: The individual components generated by the NLLS at the detention wavelength of 1.33 μm. Contributing to the oscillatory response is a low frequency component at 125 cm^{-1} (red), the ground state at 170 cm^{-1} (blue), and the second harmonic at 340 cm^{-1} (green). (Reprinted with permission from Morrissey, F. X. and S. L. Dexheimer, *Vibrational spectroscopy of nonlinear excitations via excited-state resonant impulsive Raman spectroscopy* in Ultrafast Phenomena XV, P. Corkum, D. Jonas, D. Miller, A. Weiner, Editors. 2007, Springer-Verlag. *in press*. Copyright 2007, Springer Science and Business Media.)

	Freq. (cm^{-1})	τ (fs)
	0	> 10000
	0	1500
equilibrated self-trapped exciton	**125**	**320**
fundamental symmetric stretch	170	2200
second harmonic	340	790

Table 5.1: Parameter results of the NLLS for the pump-pump-probe change in differential transmittance measurement of PtBr shown in Figure 5.5.

5.2.2 Single Pulse Excitation Pump-Probe Measurements

A careful analysis of the pump-probe measurements is paramount to ensure that the 125 cm^{-1} is inherent to only the double pump response. The components of the single pump responses were determined with LPSVD [5] and confirmed by NLLS [6] of the data to a sum of exponentials and exponentially damped cosine waves given in Equation 4.1.

The single 800 nm pump response (Figure 5.7) has the characteristic excitonic self-trapped red-shifted induced absorbance and corresponding strongly damped low frequency component at 107 cm^{-1} with a dephasing time of 270 fs. The long pump pulse duration severely reduces the ground state response (Figure 5.8) generated by resonantly enhanced stimulated impulsive Raman process for reasons discussed in Section 3.3.2. Nonetheless, these measurements establish the generation of self-trapped excitons via excitation of the IVCT transition at 800 nm.

The single 1.31 μm pump response (Figure 5.9) shows only ground state vibrations at the fundamental symmetric stretch and the second harmonic (Figure 5.10). The shorter duration pump pulse generates a greater wavepacket response and a better characterization of the ground state frequency and the dephasing time at 170 cm^{-1} and 2.5 ps, respectively. The wavepacket response is consistent with impulsive Raman excitation.

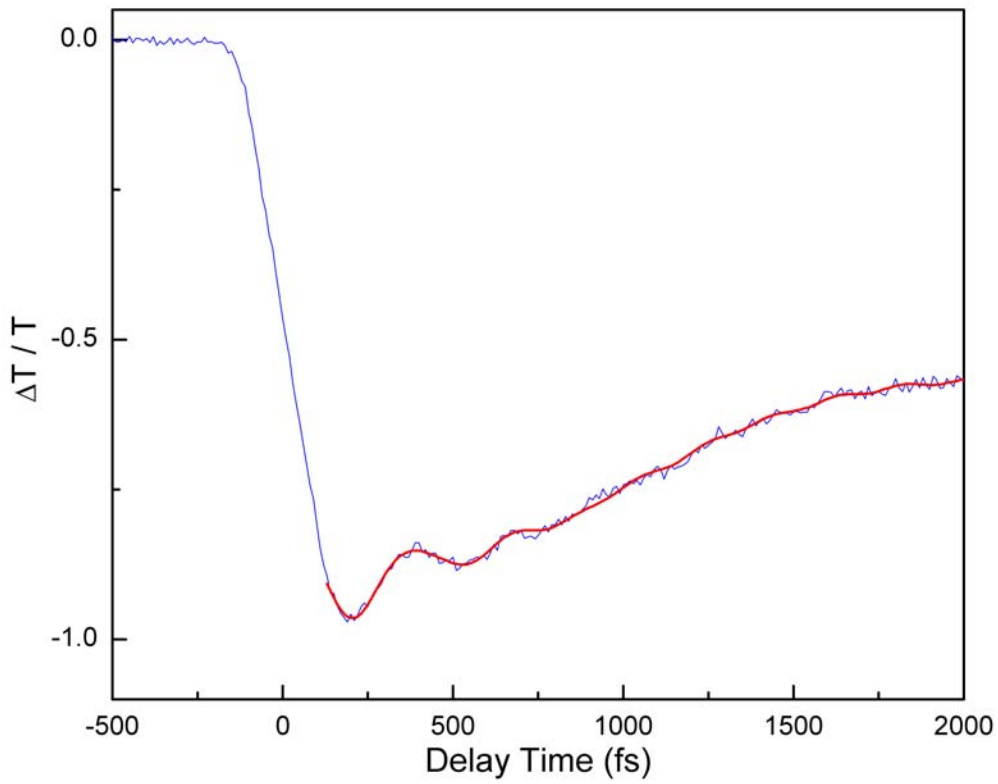

Figure 5.7: (Single Pump Measurement) The nondegenerate pump-probe measurement of the time-resolved differential transmittance of PtBr pumped with a 110 fs pulse centered at 800 nm and probed (with a 45 fs OPA pulse centered 1.31 μm) at a detection wavelength of 1.33 μm. The red trace represents a fit to the data using NLLS.

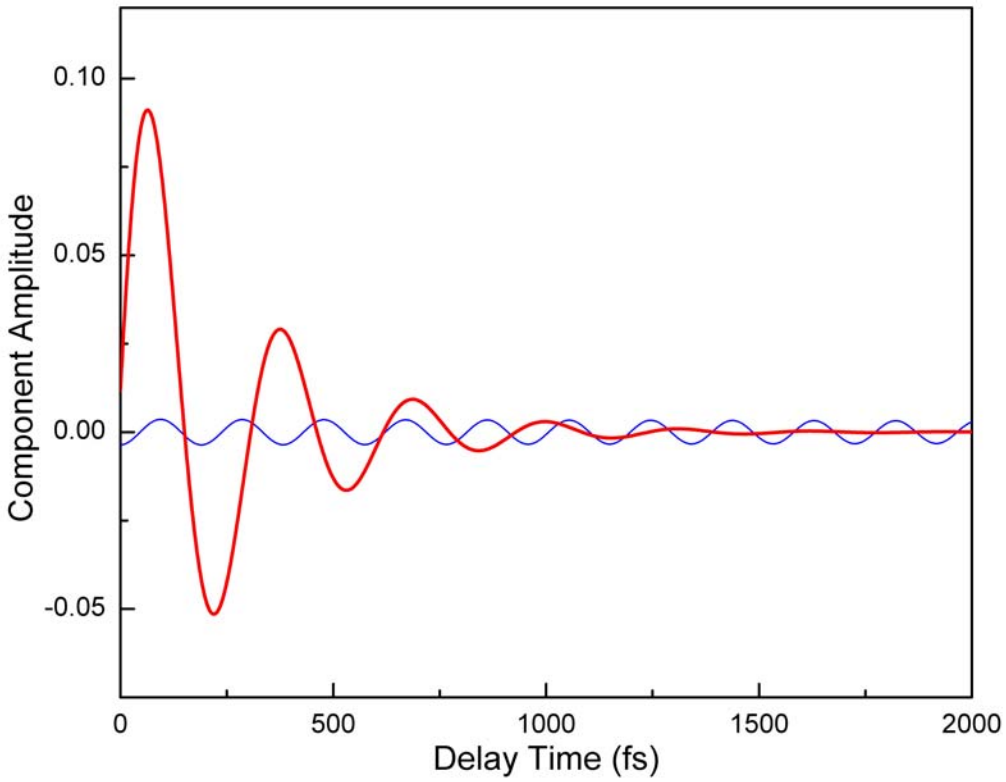

Figure 5.8: The individual components of the nondegenerate pump-probe measurement generated by the NLLS, with an 800 nm pump and a detection wavelength of 1.33 μm. Contributing to the oscillatory response is a low frequency component at 107 cm^{-1} (red) with a dephasing time of 270 fs and the ground state at 174 cm^{-1} (blue) with a dephasing time of > 10 ps.

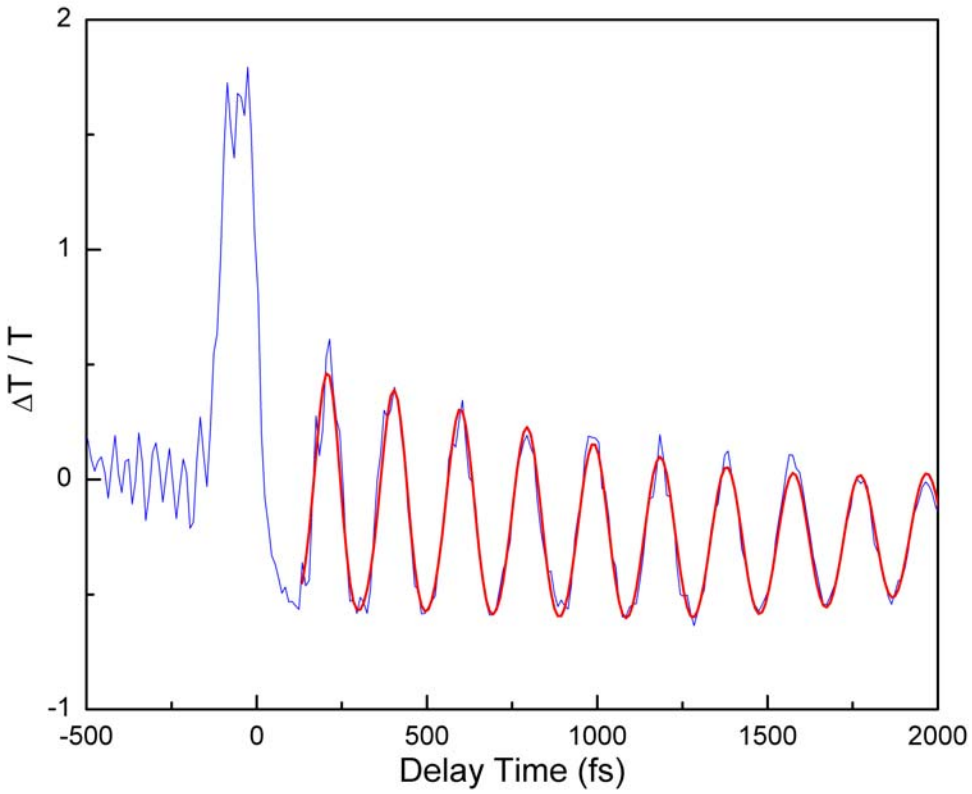

Figure 5.9: (Single Pump Measurement) The degenerate pump-probe measurement of the time-resolved differential transmittance of PtBr was pumped and probed with a pulse from an OPA having a duration of 45 fs centered at 1.31 μm. The probe pulse, after transmission through PtBr, was wavelength-resolved via a monochromator at a detection wavelength of 1.33 μm. The red trace represents a fit to the data using the NLLS.

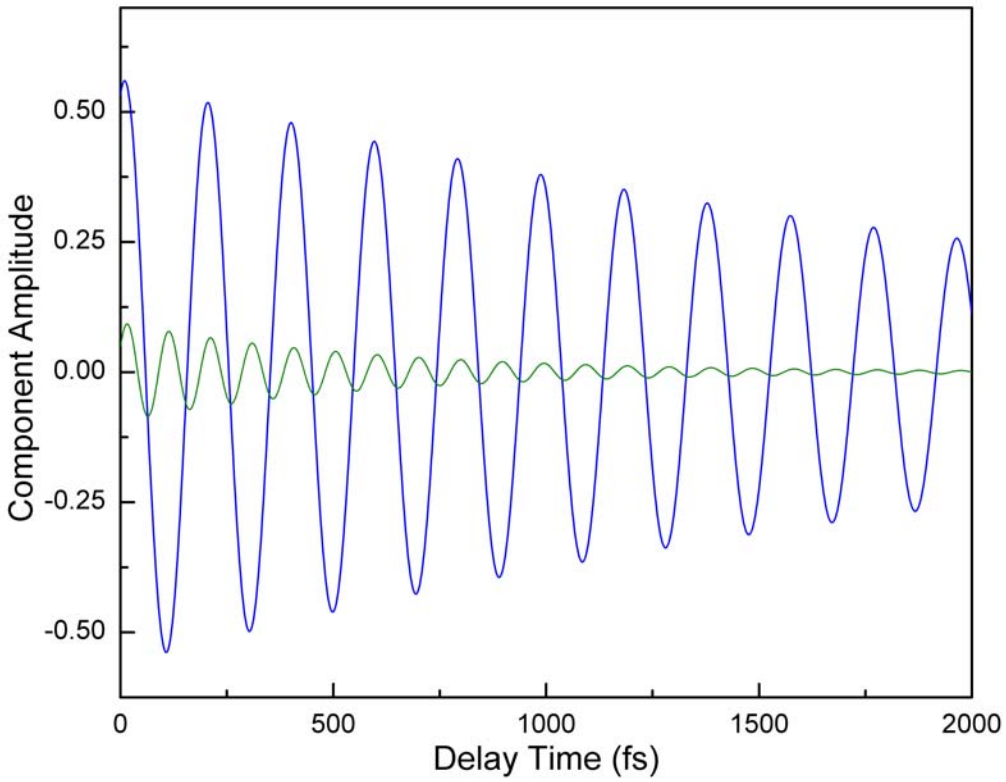

Figure 5.10: The individual components of the 1.31 μm degenerate pump-probe measurement generated by NLLS at the detection wavelength of 1.33 μm. Contributing to the oscillatory response is the ground state at 170 cm^{-1} (blue) with a dephasing time of 2.5 ps and the second harmonic at 340 cm^{-1} (green) with a dephasing time of 580 fs.

5.2.3 Interpretation of the Double Pump Response

The pump-pump-probe measurement reveals a new frequency at 125 cm^{-1}, which is assigned to the impulsive Raman excitation of the equilibrated self-trapped exciton, via the process shown in Figure 5.11. The system, prepared in the equilibrated self-trapped state, experiences resonantly enhanced stimulated impulsive Raman excitation by the second pump pulse (see Section 3.3.2). The nonstationary wavepacket motion on the self-trapped exciton potential is detected by the time delayed probe pulse (not shown in figure). The transition of the wavepacket to a higher electronic state is seen as an induced absorbance in the double modulated response.

The mechanism for the ground state 170 cm^{-1} vibration is consistent with stimulated emission pumping as shown in Figure 5.12. The 1.31 μm pump falls within the luminescence spectrum of the self-trapped exciton [7] and can drive the wavepacket back to the ground state. The nonstationary ground state wavepacket motion is detected by the time delayed probe pulse.

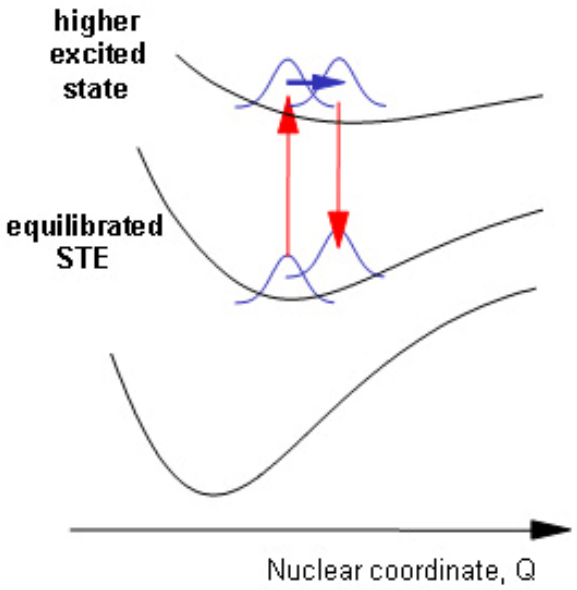

Figure 5.11: Schematic potential energy surfaces showing resonantly enhanced impulsive Raman excitation of the equilibrated self-trapped exciton.

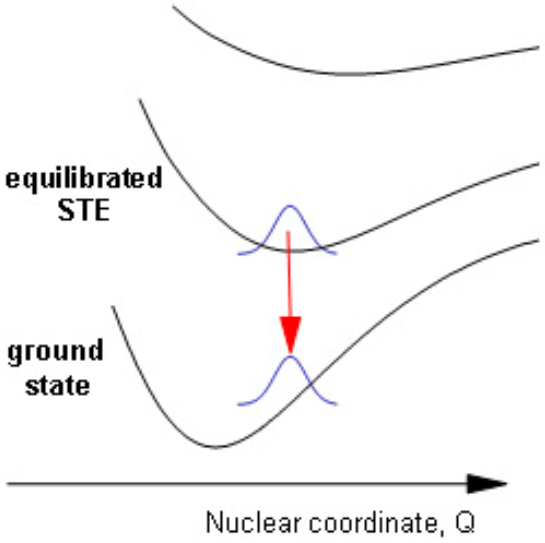

Figure 5.12: Schematic potential energy surfaces showing ground state wavepacket generation via stimulated emission pumping.

5.2.4 Detection Wavelength Dependence of the Double Pump Measurements

Additional wavelength-resolved pump-pump-probe measurements were carried out in order to further characterize the response. Time-resolved changes in the differential transmittance were observed in PtBr taken at a series of probe wavelengths on either side of the probe pulse spectrum ($\lambda_{detection} > 1.31$ μm and $\lambda_{detection} < 1.31$ μm), hereafter referred to as the red and blue side of the spectrum. The measurement of the wavelength dependence (probed at 1.32 μm and 1.29 μm) and analysis is plotted in Figures 5.13 and 5.14 with parameters listed in Table 5.2.

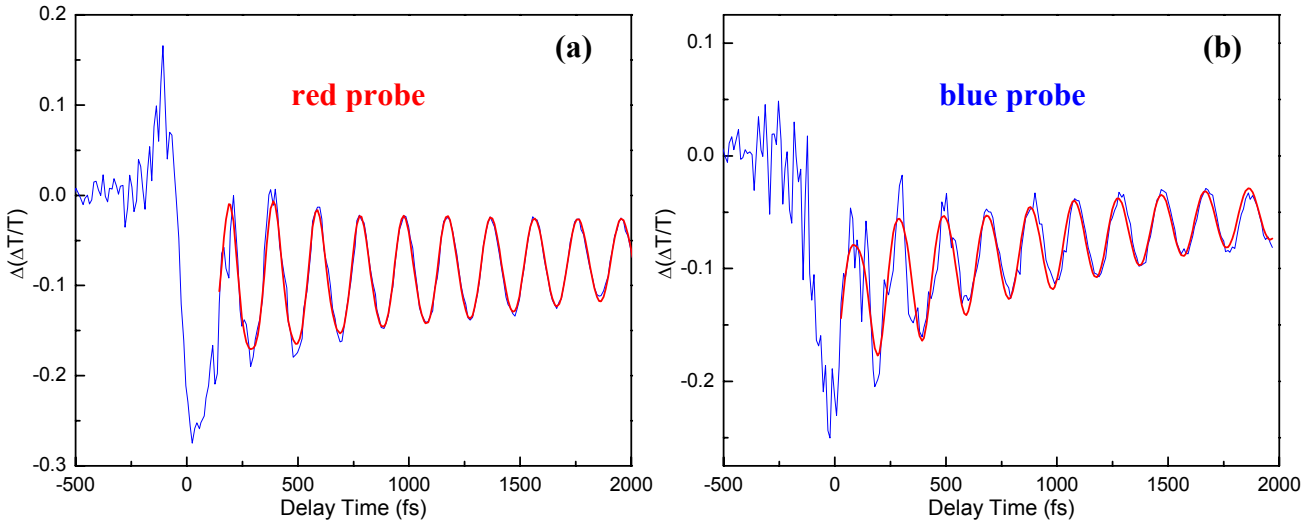

Figure 5.13: Wavelength-resolved double pump measurements probed on the red and blue side of the probe pulse. PtBr is pumped with two pulses: pump 1 at -1 ps, 800 nm, 110 fs pulse; pump 2 at 0 fs, 1.31 μm, 45 fs pulse. The vibrational coherence of the self-trapped state is investigated with a variable delay probe pulse at detection wavelengths: (a) 1.32 μm and (b) 1.29 μm. The red trace represents a fit to the data using NLLS with parameters in Table 5.2.

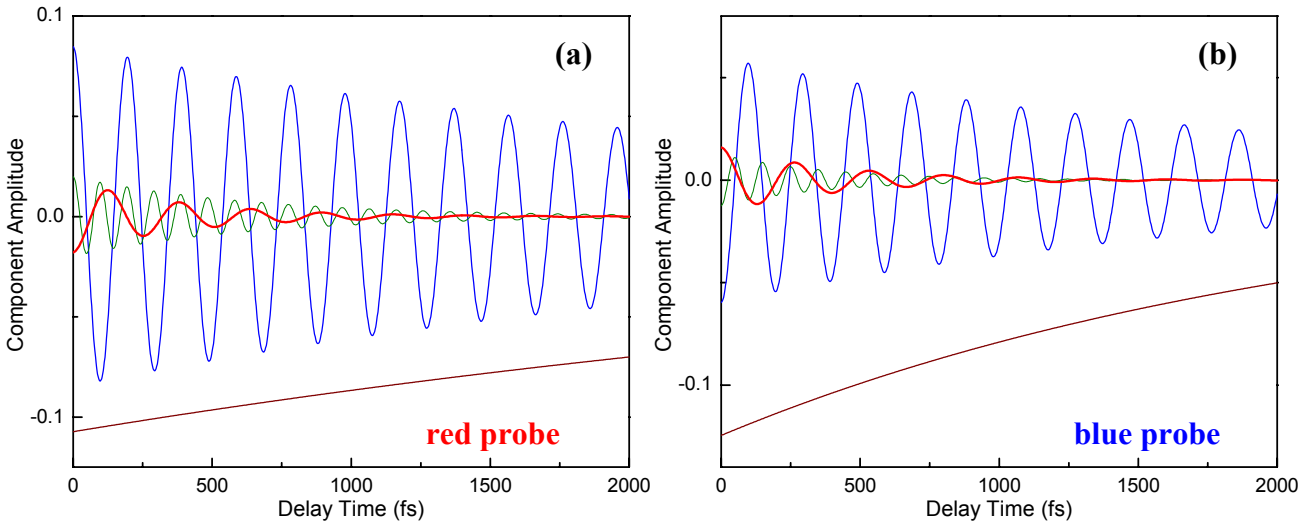

Figure 5.14: The individual components (of the double pump response) generated by the NLLS for specific detection wavelengths of (a) 1.32 μm and (b) 1.29 μm. Contributing to the oscillatory response is a low frequency component at ~ 125 cm^{-1} (red), the ground state at 170 cm^{-1} (blue), and the second harmonic at 340 cm^{-1} (green).

detection wavelength		Freq. (cm^{-1})	τ (fs)	ϕ (deg)
	decay	0	4700	…
1.33 μm	**equilibrated self-trapped exciton**	**130**	**410**	**-180**
red probe	fundamental symmetric stretch	170	3000	0
	second harmonic	344	650	0
	decay	0	2200	…
1.29 μm	**equilibrated self-trapped exciton**	**125**	**430**	**0**
blue probe	fundamental symmetric stretch	170	2100	180
	second harmonic	334	400	180

Table 5.2: Parameter results of the NLLS for the pump-pump-probe change in differential transmittance measurements detailed in Figure 5.13.

The double pump measurements probed on either side of the probe spectrum reveal two key results. First, the motion of the equilibrated self-trapped exciton is out of phase by 180° when probed on the red verse the blue side of the pump spectrum; 1.33 μm probe: 125 cm^{-1} is at -180° and 1.29 μm probe: 125 cm^{-1} is at 0°. Second, the ground state vibrational motion is out of phase with the motion of the equilibrated self-trapped exciton by 180°; 1.33 μm probe: 125 cm^{-1} is at -180° while ground state is at 0° and 1.29 μm probe: 125 cm^{-1} is at 0° while the ground state is at 180°. At each detection wavelength, the ground and excited state vibrations are out of phase with respect to each other. The phase relationships of the individual components are shown in Figure 5.14.

The phase of the 125 cm^{-1} oscillation assigned to the equilibrated self-trapped state is consistent with modulation of the excited-state absorption by the motion of the Raman-induced wavepacket. On the red side of the probe spectrum, the oscillation appears as a negative differential transmittance at t = 0, corresponding to an increase in absorption due to the displaced wavepacket shown in Figure 5.11. On the blue side of the probe spectrum, the modulation appears as an increase in transmission at t = 0, becoming a decrease in transmission one-half period later, when the wavepacket is at the opposite turning point of the well. The dependence of the 170 cm^{-1} ground state wavepacket oscillation on detection wavelength is consistent with modulation of the index of refraction by the coherent vibration, as seen in previous impulsive stimulated Raman measurements [8].

5.3 Summary

The vibrationally impulsive multi-pump probe measurements reveal two key results. (1) The observation of the motion associated with the equilibrated self-trapped exciton at a frequency of 125 cm^{-1}. (2) The observation of a vibrational frequency shift (from 110 cm^{-1} to 125 cm^{-1}) associated with self-trapping upon equilibration. The shift in the excited state frequency is expected to reflect a change in localization and charge distribution as the delocalized final state of the IVCT transition evolves into the more localized stabilized self-trapped exciton. Interestingly, this shift in frequency would be expected to contribute to the observed rapid dephasing of the 110 cm^{-1} wavepacket motion as the system evolves to the self-trapped state. The measurements in the next chapter report an increase in the excited state dephasing time at low temperature, indicating that at room temperature, thermal effects contribute to the excited state vibrational coherence. The shift of the excited state frequency from 110 cm^{-1} to 125 cm^{-1} (a change of 15 cm^{-1}) places an upper limit on the dephasing time on the order of 2 ps.

5.4 Reference for Chapter 5

1. Morrissey, F. and S. Dexheimer, *Vibrational spectroscopy of nonlinear excitations via excited-state resonant impulsive Raman spectroscopy* in Ultrafast Phenomena XV, P. Corkum, D. Jonas, D. Miller, A. Weiner, Editors. 2007, Springer-Verlag. *in press*.

2. Cerullo, G. and S. DeSilvestri, *Ultrafast optical parametric amplifiers.* Review of Scientific Instruments, 2003. **74**(1): pp. 1-18; the first experimental observation of optical parametric amplification is presented in the following reference: Giordmaine, J. and R. Miller, *Tunable Coherent Parametric Oscillation in $LiNbO_3$ at Optical Frequencies*. Physical Review Letters, 1965. **14**(24): pp. 973-976; the first theoretical treatment of optical parametric amplification where the pump, signal, and idler wave is free to have different directions of propagation: Kroll, N., *Parametric Amplification in Spatially Extended Media and Application to the Design of Tuneable Oscillators at Optical Frequencies*. Physical Review, 1962. **127**(4): pp. 1207-1211; the fundamental idea was first consider in: Lord Rayleigh, *On maintained vibrations.* The London, Edinburgh and Dublin Philosophical Magazine and Journal of Science, 1883. series 5, volume 15: pp 229-235; Lord Rayleigh, *On the maintenance of vibrations by forces of double frequency, and on the propagation of waves through a medium endowed with periodic structure.* The London, Edinburgh and Dublin Philosophical Magazine and Journal of Science, 1887. series 5, volume 24: pp 145-159.

3. Dexheimer, S., A. Van Pelt, J. Brozik, and B. Swanson, *Ultrafast vibrational dynamics in a quasi-one-dimensional system: Femtosecond impulsive excitation of the PtBr(en) mixed-valence linear chain complex.* Journal of Physical Chemistry A, 2000. **104**(18): pp. 4308-4313.

4. Dexheimer, S., A. Van Pelt, J. Brozik, and B. Swanson, *Femtosecond vibrational dynamics of self-trapping in a quasi-one-dimensional system.* Physical Review Letters, 2000. **84**(19): pp. 4425-4428.

5. Wise, W., M. Rosker, G. Millhauser, and C. Tang, *Application of linear prediction least-squares fitting to time-resolved optical spectroscopy.* IEEE Journal of Quantum Electronics, 1987. **QE-23**(7): pp. 1116-1121; Giordano, A. and F. Hsu, *Least square estimation with application to digital and signal processing.* 1985, New York: John Wiley & Sons; Rao, C. and H. Toutenburg, *Linear models and least squares and alternatives. Springer series in statistics.* 1995, New York: Springer-Verlag; Lay, D., *Linear algebra and its applications.* 1996, New York: Addison-Wesley; the LPSVD code employed by the author was modeled after the particulars in the following reference: Kumaresan, R. and D. Tufts, *Estimating the parameters of exponentially damped sinusoids and pole-zero modeling in noise*. IEEE Transactions on Acoustics, Speech and Signal Processing, 1982. **30**(6): 833-840; Implementation of the LPSVD uses Fortran subroutines from Linpack and Eispack.

6. Nonlinear least squares fits were obtained using the software package Origin® Pro 7.0 (Copyright © 1991-2001 Origin Lab Corporation). The nonlinear regression application is based on a Levenberg-Marquardt algorithm following a similar flow of control as the (popular) Minpack (Fortran) subroutines (employing the same algorithm) developed by J. More', B. Garbow, and K. Hillstromthe of Argonne National Laboratory. The specific details of this method can be found in the following two references; Levenberg, K., *A method for the solution of certain non-linear problems in least squares*. Quarterly of Applied Mathematics, 1944. **2**: pp. 164-168; Marquardt, D., *An algorithm for least-squares estimation of nonlinear parameters*. Journal of the Society for Industrial and Applied Mathematics, 1963. **11**: pp. 431-441.

7. Wada, Y., K. Era, and M. Yamashita, *Luminescence lifetimes in halogen bridged mixed valence metal complexes.* Solid State Communications, 1988. **67**(10): pp. 953-956.

8. Ruhman, S., A. Joly, and K. Nelson, *Time-resolved observations of coherent molecular vibrational motion and the general occurrence of impulse stimulated scattering.* Journal of Chemical Physics, 1987. **86**(11): pp. 6563-6565.

Chapter 6

Low Temperature Studies:

Acoustic Phonon Dynamics in Self-Trapping

Room temperature studies, as discussed in the previous chapters, clearly provided valuable insight on exciton self-trapping. However, thermal excitation potentially could contribute to the degree of initial lattice disorder and to wavepacket dephasing so that thermally-induced effects could effectively mask additional components of the dynamics. This chapter presents a comparison of measurements at room (293 K) and low temperature (77 K), employing impulsive excitation. At low temperature, a large amplitude strongly damped oscillatory component is observed at a frequency within the range characteristic of acoustic phonons. Simple physical models provide an interpretation of the low temperature response where an acoustic wave contribution is associated with the self-trapping dynamics.

6.1 Room and Low Temperature Response

In these experiments, the temperature dependent nondegenerate measurements were carried out on $[Pt(en)_2Br_2][Pt(en)_2]\cdot(PF_6)_4$ (or PtBr) using the optical pump-probe apparatus. A fixed pump and a variable probe path length provide a time delay between the pulses. The differential transmittance was measured using lock-in amplification. (The details of the experimental setup are presented in Section 3.1.) A 1 kHz Ti:sapphire regenerative amplifier (discussed in Section 3.2.1) produces optical pulses 35 fs in duration centered at 800 nm, which excites the IVCT transition. The transmission was probed with a compressed white light continuum, generated by focusing a portion of the amplifier beam into a 2 mm sapphire plate.

The PtBr crystals were mounted on a sapphire plate that was in contact with a cold finger attached to a liquid nitrogen bath. The samples were housed under vacuum in a KelTran PF Liquid Nitrogen Cryostat [1]. A comparison of the low (77 K) and room (293 K) temperature response at a detection wavelength of 940 nm is shown in Figure 6.1. The responses are normalized to the long term signal at 7.5 ps for comparison of the features at early time delay.

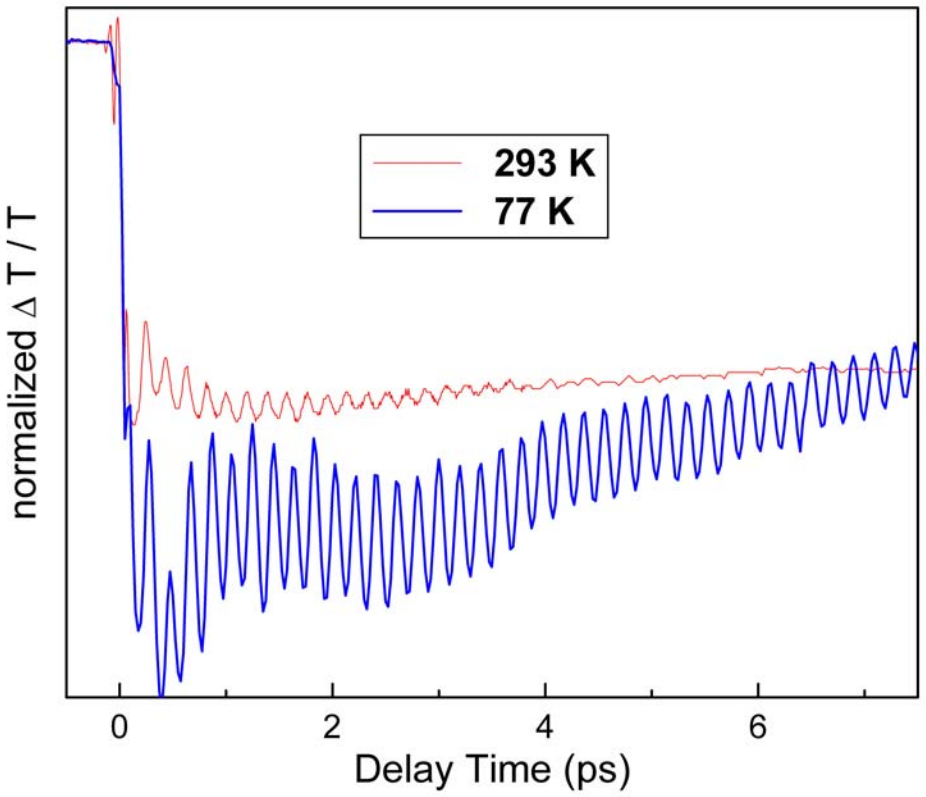

Figure 6.1: The room and low temperature response of PtBr following excitation with a 35 fs pulse centered at 800 nm and probed at a detection wavelength of 940 nm. The signals are normalized to the long term decay at 7.5 ps for comparison.

Comparison of the response at room and low temperature reveals two striking features only present at low temperature: (1) a large amplitude very low frequency component that modulates the induced absorbance and (2) an increase in the vibrational dephasing time. The interpretation of the very low frequency component is attributed to the generation of coherent acoustic waves, discussed in more detail in Section 6.2. The increased ground state dephasing is consistent with temperature dependent resonance Raman measurements, which show a peak narrowing of the symmetric stretch mode with decreasing temperature [2]. In addition to these two features just described, the low temperature optical response was found to possess all of the components seen at room temperature (e.g., ground state symmetric stretch, second harmonic, and excited state vibrations; induced absorption and fast formation). (Note that the room temperature response has been discussed extensively in Section 4.1.)

The low temperature (77 K) response in PtBr was probed at a series of detection wavelengths within the self-trapped exciton absorption band (i.e., 855 nm, 880 nm, and 940 nm). The differential transmittance measurements at these detection wavelengths all showed a large amplitude very low frequency component that modulates the induced absorbance, with no significant variation in the acoustic response. A large amplitude very low frequency component was also observed in the time-resolved differential transmittance of $[Pt(en)_2Br_2][Pt(en)_2]\cdot(ClO_4)_4$ at 77 K. These measurements showed no significant variation in the acoustic response due to a substitution in the counterions. Investigation of the dependence of the pump fluence on the acoustic response is discussed in Section 6.3.

To determine whether transverse components of the chain axis contribute to the response, impulsive excitation measurements were carried out with various pump and probe polarizations including: (H = horizontal, V = vertical)

pump H, probe V, chain axis H;

pump V, probe H, chain axis H;

pump V, probe V, chain axis H.

No response was observed in any state other than the pump and probe polarized parallel with the chain axis (pump H, probe H, chain axis H). This indicates that no transverse components contribute to the photoinduced lattice motions.

Fitting of the low temperature data to a sum of exponentially damped cosines and exponentials was complicated by the interdependence of the exponential formation and the very low frequency component. To address this obstacle, the nonlinear least squares fitting method (NLLS) [3] was used to fit the data to an exponential formation and decay component together with a sum of exponentially damped cosines and exponentials:

$$S(t) = a_{fd}\left[1 - e^{-\frac{t}{\tau_f}}\right] e^{-\frac{t}{\tau_d}} + \sum_i a_i \, e^{-\frac{t}{\tau_i}} \cos\left(2\pi v_i t + \phi_i\right) \tag{6.1}$$

where a_{fd} is the amplitude of the formation / decay component, τ_f is the exponential formation time constant, τ_d is the exponential decay time constant, the sum is over i (the number of components), a_i is the amplitude, τ_i is the exponential decay constant, υ_i is the frequency, and ϕ_i is the phase. The starting parameters for the NLLS fitting were obtained by analyzing the data using the LPSVD method [4] and Fourier analysis [5]. While other functional forms might be considered for the dynamics, these simple exponentials and cosine waves give an excellent characterization of the time-resolved response. A representative measurement of the low temperature response (shown in Figure 6.1) was analyzed by the NLLS, with the results plotted in blue on top of the data in Figure 6.2 and the components plotted in Figure 6.3

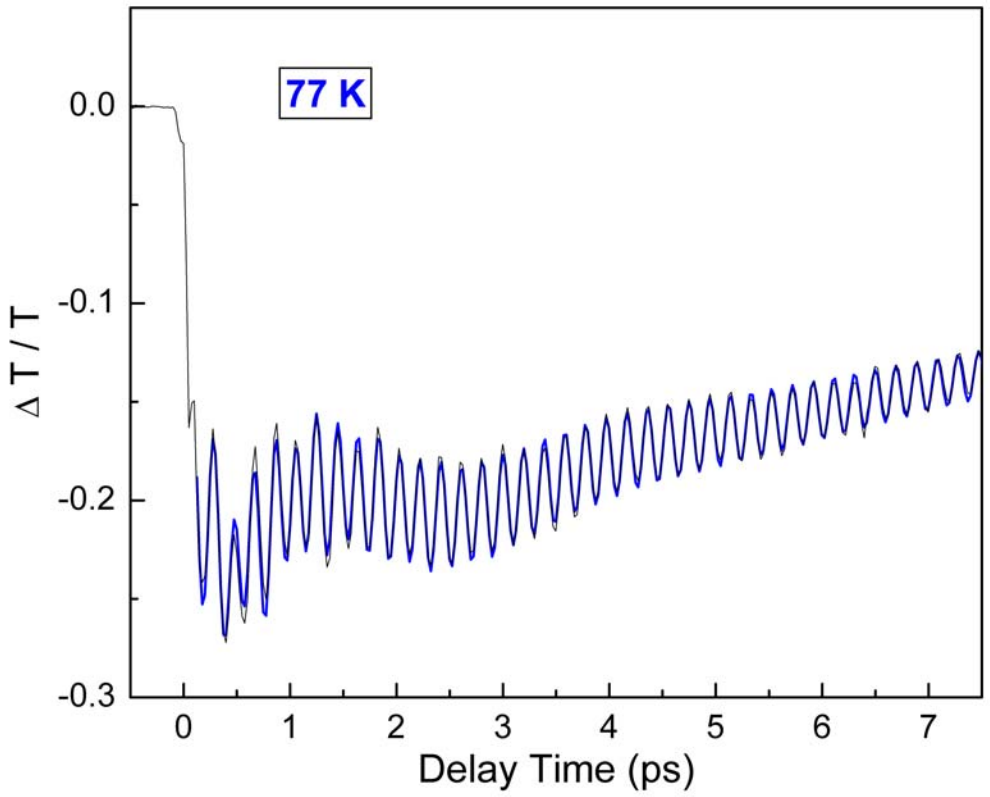

Figure 6.2: Comparison of the differential transmittance of PtBr at low temperature (77 K) (in grey) with a NLLS fit to the multi-component model (in blue) of Equation 6.1. In the nondegenerate pump-probe measurement, PtBr was excited with a 35 fs pulse centered at 800 nm and probed at a detection wavelength of 940 nm.

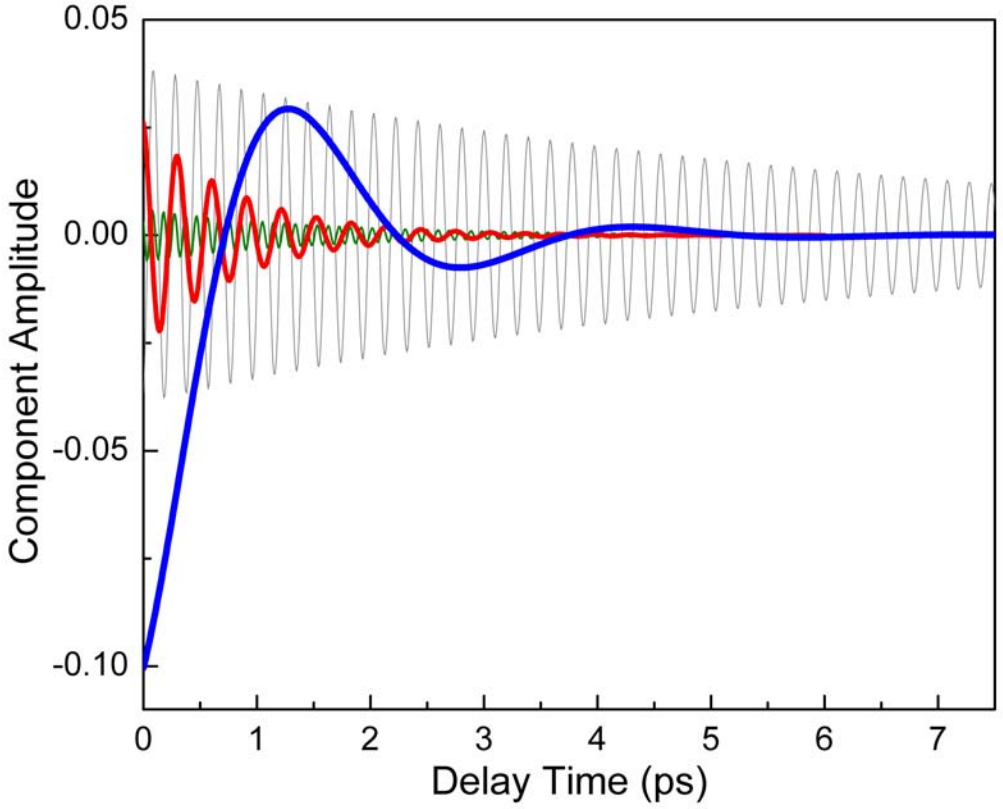

Figure 6.3: Oscillatory components determined by NLLS of the low temperature PtBr data (in Figure 6.2) at a detection wavelength of 940 nm. Contributing to the response is a very low frequency component at 11 cm^{-1} (blue), the excited state component at 109 cm^{-1} (red), the ground state symmetric stretch at 172 cm^{-1} (grey), and the second harmonic at 344 cm^{-1} (green).

	Freq. (cm^{-1})	τ (fs)
decay	0	13000
formation	0	250
very low	**11**	**1100**
excited state	109	840
fundamental symmetric stretch	172	6500
second harmonic	344	1600

Table 6.1: Parameter results of the NLLS for the low temperature time-resolved differential transmittance measurement of PtBr in Figure 6.2.

6.2 Acoustic Phonon Dynamics

The low temperature measurement reveals a new frequency component at 11 cm^{-1}, which is within the range characteristic of acoustic phonons. In this section the author will provide support for the assignment of this frequency to acoustic waves associated with the self-trapping transition. Therefore, both optical (~ 110 cm^{-1} component discussed in Chapter 4) and acoustic phonons (11 cm^{-1}) have been observed contributing to the self-trapping process in the PtBr.

Various theoretical works have modeled separately the interaction of acoustic and optical phonons in a number of limiting cases, as reviewed by Rashba [6]. Work by Toyozawa emphasized the essential role that acoustical modes may play in electronic self-trapping [7]. Toyozawa found that if the interaction between the charge and lattice vibration is strong then the system can be characterized as a linear combination of localized states accompanied by a surrounding lattice distortion, with contributions from acoustic phonons. Modeling of the self-trapping process by Toyozawa predicted that as the exciton wavefunction collapses to the localized structure, energy is released in the form of acoustic waves, which stabilizes the self-trapped state [8]. As the system transitions from the delocalized to the localized state, acoustic waves carry away the excess lattice energy associated with the deformation. In a simple physical picture, the acoustic waves generated during self-trapping appear as replicas of the local lattice deformation [9], as shown in Figure 6.4. By taking the FWHM of one half cycle of a wave as the approximate spatial extent of the self-trapping excitation and using an acoustic velocity (5 km/s) estimated from modeling of the vibrational spectra of PtBr(en) [10,11], the observed 11 cm^{-1} frequency corresponds to a deformation extending over ~ 50 Å or ~ 5 unit cells of PtBr(en), as shown below.

$$\lambda = \frac{v}{f} = \frac{5\ \ km/s}{\left(11\ \ cm^{-1}\right)\left(3\times10^{10}\,cm/s\right)} = \frac{5000\ \ m/s}{0.33\ \ THz} = 150\ \ \text{Å} \tag{6.2}$$

$$\frac{\lambda}{2} = 75\ \ \text{Å} \qquad \left(\frac{\lambda}{2}\right)_{FWHM} = 50\ \ \text{Å} \tag{6.3}$$

In these equations (6.2 and 6.3), λ is the acoustic wavelength, v is the acoustic velocity, f is the measured oscillation frequency, $(\lambda/2)_{FWHM}$ is the FWHM of a half cycle of the acoustic oscillation assuming a cosine wave. Remarkably, this value of 50 Å is consistent with the spatial extent of the self-trapped exciton wavefunction in PtBr(en) estimated by Peierls-Hubbard calculations [12] discussed in Section 2.6. This result provides support for the assignment of the very low frequency modulation to acoustic waves associated with the self-trapping dynamics.

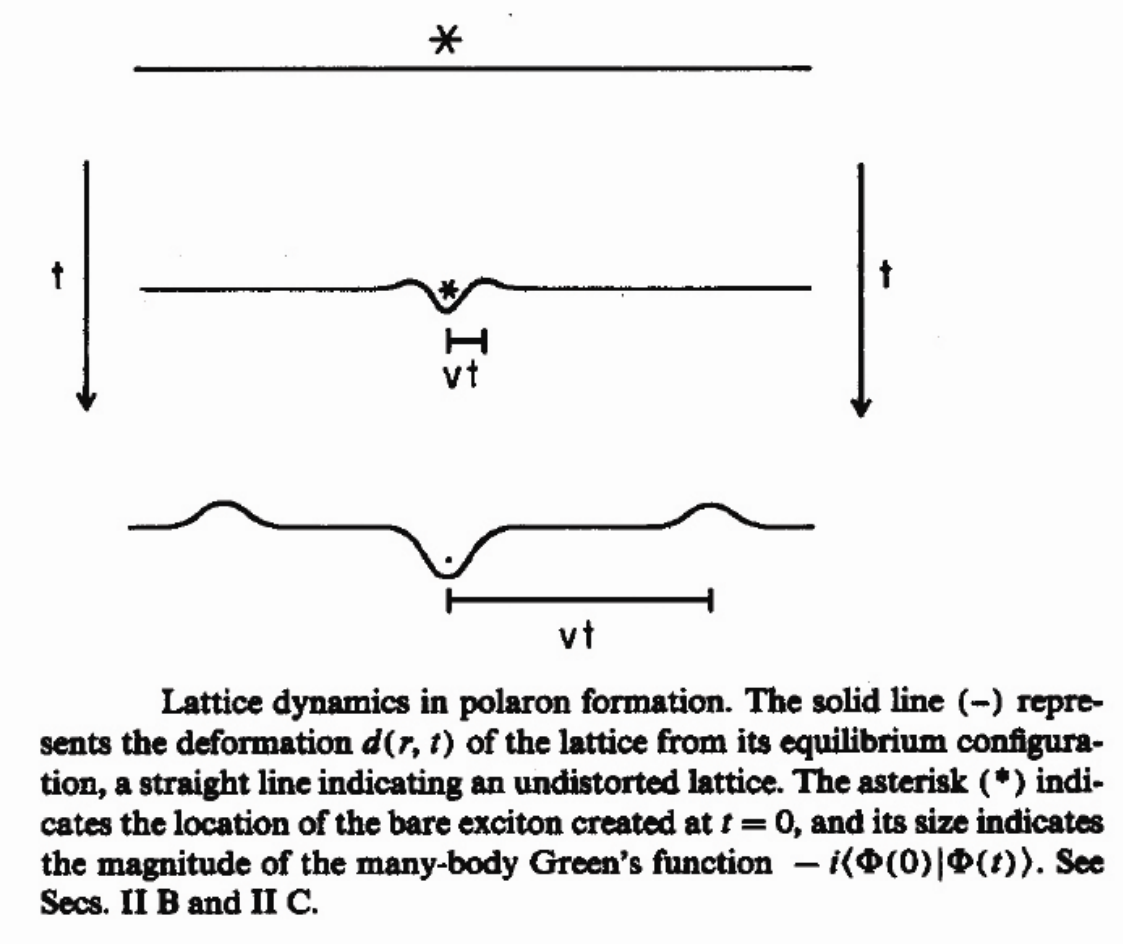

Lattice dynamics in polaron formation. The solid line (–) represents the deformation $d(r, t)$ of the lattice from its equilibrium configuration, a straight line indicating an undistorted lattice. The asterisk (*) indicates the location of the bare exciton created at $t = 0$, and its size indicates the magnitude of the many-body Green's function $-i\langle\Phi(0)|\Phi(t)\rangle$. See Secs. II B and II C.

Figure 6.4: Theoretical model of the acoustic phonon dynamics associated with self-trapping. An exciton deforms the surrounding lattice, where the lattice energy associated with the deformation is released (as the exciton localizes) in the form of acoustic waves. (Reprinted with permission from Brown, David W., Katja Lindenberg, and Bruce J. West, *On the dynamics of polaron formation in a deformable medium*. Journal of Chemical Physics, 1986. **84**(3): pp. 1574-1582. Copyright 1986, American Institute of Physics.)

Further support for the assignment of the very low frequency modulation to the generation of coherent acoustic waves during self-trapping is the dephasing time of the 11 cm^{-1} component. Modulation of the exciton's induced absorbance (at 11 cm^{-1}) is attributed to the acoustic pulse as it transverses the self-trapped exciton. A major contribution to the lifetime of the very low frequency oscillation would be the transit time of the acoustic pulse through the excitation. Using the calculated value of the deformation (50 Å) from equation 6.3 and the acoustic velocity (5 km/s) estimated from modeling of the vibrational spectra of PtBr(en) [10,11], the transit time is estimated to be 1 ps, which is consistent with the observed damping time of 1.1 ps (see Table 6.1). The calculation is shown below.

$$\tau = \frac{\left(\frac{\lambda}{2}\right)_{FWHM}}{v} = \frac{50\ \text{Å}}{5\ km/s} = 1\ ps \tag{6.4}$$

6.3 Dependence on Excitation Density

Fluence dependent measurements provide further support for the assignment of the very low frequency modulation to the generation of coherent acoustic waves during self-trapping. Figure 6.5 shows fluence dependent low temperature measurements normalized to the long term signal at 7.5 ps, at which time the very low frequency component has completely decayed away. Normalization of the signal allows for a comparison of the relative amplitudes of the very low frequency component, which decrease with increasing fluence.

The nature of the fluence dependence is as follows. After optical excitation, a randomly distributed population of optically generated excitons is expected. As the pump fluence is increased, the average distance between the excitons decreases. As exciton distances approach the

acoustic wavelength, interference would lead to a decrease in the acoustic phonon coherence and a reduction in the acoustic phonon response. This is consistent with the strongly diminished amplitude of the very low frequency modulation with increased pump fluence.

The room temperature fluence dependence in PtBr is shown in Figure 6.6. The differential transmittance measurements were normalized to the signal amplitude at 7.5 ps. A decrease in pump fluence showed no relative change in amplitude of the early time response. Therefore, only the acoustic phonon component shows a fluence dependence.

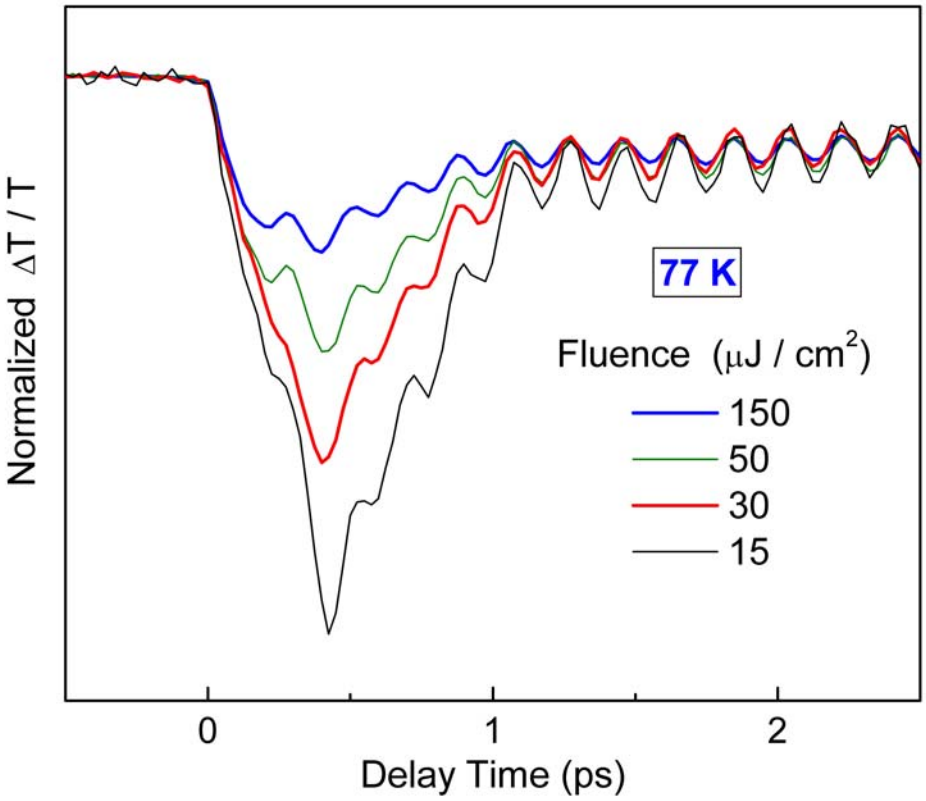

Figure 6.5: The low temperature response of PtBr at various pump fluences following excitation with a 35 fs pulse centered at 800 nm and probed at a detection wavelength of 940 nm. The differential transmittance measurements were normalized to the long time signal amplitude at 7.5 ps. A decrease in pump fluence corresponds to an increase in the relative amplitude of the acoustic wave response.

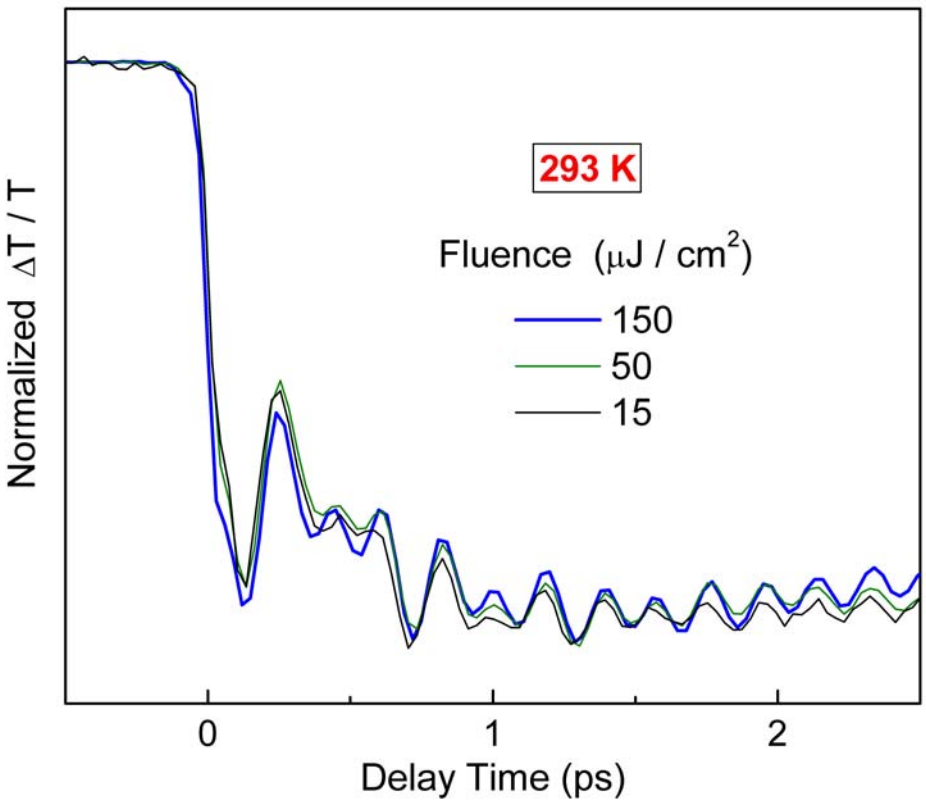

Figure 6.6: The room temperature response of PtBr at various pump fluences following excitation with a 35 fs pulse centered at 800 nm and probed at a detection wavelength of 940 nm. The differential transmittance measurements were normalized to the long time signal amplitude at 7.5 ps. A decrease in pump fluence showed no relative change in amplitude of the early time response.

6.4 Low Temperature Excited State Vibrational Coherence

The low temperature optical response of PtBr shows an increase in the excited state vibrational dephasing time relative to what is observed at room temperature (~ 300 fs). This increased vibrational coherence of the ~ 110 cm^{-1} excited state component at low temperature (~ 800 fs) indicates that the vibrational dephasing at room temperature is not simply limited by the excited state structural distortion, but has contributions from thermal effects. This conclusion is further supported by ultralow temperature measurements (~ 40 K) carried out on PtBr using liquid He in a Janis Research VT-100 variable temperature exchange gas cryostat, which revealed excited state optical phonon dephasing times approaching 2 ps. Interestingly, the vibrationally impulsive multi-pump probe measurements on PtBr (discussed in Chapter 5) reveal that as the system evolves from the final state of the IVCT transition to the equilibrated structure, the vibrational frequency shifts. The shift of the excited state frequency in PtBr from ~ 110 cm^{-1} to 125 cm^{-1} places an upper limit on the dephasing time of the optical phonon on the order of 2 ps.

6.5 Summary

The simplicity of the evidence for the acoustic phonon interaction in the localization process is striking. The three indicators are worth restating. (1) A quantity that had been undetermined experimentally was the spatial extent of the self-trapped exciton. Low temperature measurements revealed an acoustic phonon frequency allowing a calculation of the exciton spatial extent. This calculated value (using the measured acoustic phonon frequency) was found to be consistent with theoretical predictions, that being approximately 5 unit cells in PtBr. (2) Using the calculated spatial extent of the self-trapped exciton, the dephasing time of the very low

frequency component, which modulates the exciton's induced absorbance, supports the assignment of an acoustic wave that transits through the exciton. (3) Fluence dependent measurements further support the assignment of the very low frequency component to an acoustic wave associated with the self-trapping. Increased pump fluence results in a decrease in the average distance between the excitons leading to acoustic wave interference and a reduction in the acoustic phonon response.

The low temperature measurements have revealed two key results: (1) evidence for an acoustic phonon associated with the self-tapping of the exciton, indicating that not only do optical modes contribute to the self-trapping phenomenon but so do acoustical modes, and (2) the increase in the excited state dephasing time, which indicates that the dephasing mechanisms at room temperature are not entirely intrinsic to the excited state structural change but have contributions from thermal effects.

6.6 References for Chapter 6

1. Bailey, C., *Advanced cryogenics.* 1971. New York: Plenum Press. pp. 499-502; the success of a cryogenic system is strongly dependent on its vacuum system: Dennis, N. and T. Heppell, *Vacuum system design.* 1968. London: Chapman and Hall.

2. Huckett, S., B. Scott, S. Love, R. Donohoe, C. Burns, E. Garcia, T. Frankcom, B. Swanson, *Effects of temperature on the crystal and molecular structure of the mixed-valence linear chain* $[Pt(en)_2][Pt(en)_2X_2][ClO_4]_4$ *(X = Cl, Br).* Inorganic Chemistry, 1993. **32**: pp. 2137-2144.

3. Nonlinear least squares fits were obtained using the software package Origin® Pro 7.0 (Copyright © 1991-2001 Origin Lab Corporation). The nonlinear regression application is based on a Levenberg-Marquardt algorithm following a similar flow of control as the (popular) Minpack (Fortran) subroutines (employing the same algorithm) developed by J. More', B. Garbow, and K. Hillstromthe of Argonne National Laboratory. The specific details of this method can be found in the following two references; Levenberg, K., *A method for the solution of certain non-linear problems in least squares*. Quarterly of Applied Mathematics, 1944. **2**: pp. 164-168; Marquardt, D., *An algorithm for least-squares estimation of nonlinear parameters*. Journal of the Society for Industrial and Applied Mathematics, 1963. **11**: pp. 431-441.

4. Wise, W., M. Rosker, G. Millhauser, and C. Tang, *Application of linear prediction least-squares fitting to time-resolved optical spectroscopy.* IEEE Journal of Quantum Electronics, 1987. **QE-23**(7): pp. 1116-1121; Giordano, A. and F. Hsu, *Least square estimation with application to digital and signal processing.* 1985, New York: John Wiley & Sons; Rao, C. and H. Toutenburg, *Linear models and least squares and alternatives. Springer series in statistics.* 1995, New York: Springer-Verlag; Lay, D., *Linear algebra and its applications.* 1996, New York: Addison-Wesley; the LPSVD code employed by the author was modeled after the particulars in the following reference: Kumaresan, R. and D. Tufts, *Estimating the parameters of exponentially damped sinusoids and pole-zero modeling in noise*. IEEE Transactions on Acoustics, Speech and Signal Processing, 1982. **30**(6): 833-840; Implementation of the LPSVD uses Fortran subroutines from Linpack and Eispack.

5. Cooley, J., and J. Tukey, *An algorithm for the machine calculation of complex Fourier series*. Mathematics of Computation, 1965. **19**(90): pp. 297-301; Bracewell, R., *The Fourier Transform and Its Applications: Electrical and Electronic Engineering Series*, 1978. New York: McCraw-Hill; Jean Baptiste Joseph Fourier formulated the trigonometric analysis in 1807 (59 years earlier, L. Euler introduced the cosine representation of an analytical function, which is a less general construction of the before mentioned theory). Even though the Fourier transform has been named in his honor, recent rigorous historical investigations indicate Carl Friedrich Gauss conceived of the mathematical theory well beforehand: Heideman, M., D. Johnson, and C. Burrus, *Gauss and the History of the Fast Fourier Transform.* IEEE Acoustics, Speech, and Signal Processing Magazine, 1984. 1(4): pp. 14-21; Gauss, C., *Nachlass: Theoria interpolationis methodo nova tracata*. pp. 265-303, in *Carl Friedrich*

Gauss, Werke, Band 3, Göttingen: Königlichen Gesellschaft der Wissenschaften, 1866. ("unpublished", circa 1805).

6. Rashba, E., *Self-trapping of excitons* in Excitons, E. Rashba and M. Sturge, Editors. 1979, New York: North-Holland. pp. 547-602.

7. Toyozawa, Y., *Self-trapping of an electron by the acoustical mode of lattice vibration. I.* Progress of Theoretical Physics, 1961. **26**(1): pp. 29-44.

8. Toyozawa, Y., *Electrons, Holes, and Excitons in Deformable Lattice.* presented in *Relaxation of Elementary Excitations,* Springer Series in Solid-State Sciences. Volume 18, R. Kubo and E. Hanamura, Editors. 1980, Springer-Verlag. pp. 3-18.

9. Brown, D., K. Lindenberg, and B. West, *On the dynamics of polaron formation in a deformable medium*. Journal of Chemical Physics, 1986. **84**(3): pp. 1574-1582; Brown, D., K. Lindenberg, B. West, J. Cina, and R. Silbey, *Polaron formation in the acoustic chain*. Journal of Chemical Physics, 1987. **87**(11): pp. 6700-6705.

10. Love, S., S. Huckett, L. Wori, T. Frankcom, S. Ekberg, and B. Swanson, *Far-infrared spectroscopy of halogen-bridged mixed-valence platinum-chain solids: isotope-substitiution studies.* Physical Review B, 1993. **47**(17): pp. 11 107-11 123.

11. Clark, R., *Raman and resonance Raman spectroscopy of linear chain complexes,* in *Advances in infrared and Raman spectroscopy,* R. Clark and R. Hester, Editors. 1984, Wiley. pp. 95-132.

12. Gammel, J., A. Saxena, I. Batistic, A. Bishop, and S. Phillpot, *Two-band model for halogen bridged mixed-valence transition-metal complexes. I. Ground state and excitation spectrum.* Physical Review B, 1992. **45**(4): pp. 6408-6434.

Chapter 7

Conclusion

The results of the studies conducted by the author and reported in this dissertation present detailed information on the dynamics of formation of localized excitations in quasi-one-dimensional halide-bridged mixed-valence transition metal chains. These systems have proven to be ideal for investigating localized states due to the strong coupling between the electronic and vibrational dynamics, the reduced dimensionality which simplifies the electron-phonon interactions, and the tunability of the relative strength of the electron-phonon coupling by chemical substitution of the halides in the molecular chains. The author employed impulsive excitation techniques on the PtX(en) complexes to study (1) the weak electron-phonon coupled valence-delocalized system, (2) the vibrational dynamics associated with the equilibrated self-trapped state, and (3) acoustic phonon response associated with the self-trapping dynamics. These results are briefly reviewed below followed by a discussion of how they are interrelated. Included in this discussion is the dependence on the relative strength of the electron-phonon coupling with the self-trapping dependence. This section concludes with a brief note on future work.

In the weak electron-phonon coupling limit of PtI, we assign a low frequency modulation of the induced absorbance, at 106 cm^{-1}, to the motion that drives the system to the self-trapped state. A formation component, which damps within approximately a single period of the low frequency motion, is assigned to the transfer of population from the free exciton to the self-trapped exciton state.

Using a multiple pulse pump-pump-probe sequence on PtBr, the observed vibrational frequency (at 125 cm^{-1}) is assigned to a characteristic mode of the self-trapped exciton in its equilibrated structure. Time-domain excited state resonant stimulated impulsive Raman excitation revealed a shift in frequency from the final state of the intervalence charge transfer transition (at ~ 110 cm^{-1}) to the equilibrated configuration (at 125 cm^{-1}). This upward shift in frequency is consistent with a structural change in the equilibrated state that is expected to include both a change in charge distribution and associated bond lengths.

Low temperature pump-probe measurements uncovered an acoustic phonon response, at 11 cm^{-1}, seen as a large amplitude very low frequency modulation of the induced absorbance. Using this frequency, the localized lattice deformation was estimated to have a spatial extent of ~ 5 unit cells, which reflects the size of the self-trapped exciton, consistent with theoretical models for polaron formation. This assignment of the 11 cm^{-1} oscillation to acoustic waves associated with the self-trapping dynamics is further supported by the dephasing time of the vibration (corresponding to a transit time of the wave across the deformation) and fluence dependent measurements (which show increasing fluence corresponding to a decrease in the average distance between excitons resulting in interference of the acoustic waves). An enhancement of the excited state optical phonon wavepacket dephasing time indicates that the vibrational coherence properties of the exciton at room temperature are not simply limited by the excited state structural distortion.

The PtX series show a direct correlation between the shift of the vibrational frequencies (optically active ground state Raman active symmetric stretch and the excited state vibration associated with the motion that drives the system to the self-trapped state) and the degree of

electronic delocalization. The more delocalized the system, the less of a frequency shift observed. These smaller frequency shifts correlate with a lesser degree of initial lattice distortion.

The impulsive excitation measurements conducted on the PtX series revealed an excited state motion which rapidly dephases. Low temperature measurements indicate that the dephasing time of the excited state vibration has thermal contributions. Multiple pump measurements investigate the vibrational coherence of the excited state motion that drives the system to the self-trapped state. As the system evolves from the final state of the IVCT transition to the equilibrated structure, the vibrational frequency shifts ~ 15 cm^{-1}, providing an upper limit on dephasing time of the excited state motion on the order of 2 ps. This upshift in frequency from ~ 110 cm^{-1} to 125 cm^{-1} occurs as the electronic wavefunction becomes more localized as the system evolves to the equilibrated self-trapped exciton. This localization is also reflected in the acoustic phonon dynamics measured at low temperature. In this simple picture, the electronic wavefunctions collapse into a more localized state resulting in the release of energy in the form of acoustic waves, which stabilizes the structure. These measurements show that both optical and acoustic modes are involved in the localization process.

This study has motivated future low temperature investigations. Thermal excitation could potentially still play a role in the low temperature measurements present in this dissertation. Lower temperature liquid helium measurements (at ~ 4 K) might uncover additional dynamics obscured at 77 K. Future works will also include time-domain excited-state resonant impulsive Raman measurements. An interesting correlation is that as the strength of the electron-phonon coupling is increased, there is an increase in the vibrational dephasing rate of the excited state motion. Therefore, one might expect to see a greater relative upshift in the equilibrated self-trapped exciton frequency in PtCl as compared to PtBr consistent with an increased degree of

localization in the stabilized structure. Additional studies using optical pump-terahertz probe measurements will investigate the formation and evolution of polarons in the PtX systems.

APPENDIX A

Linear Prediction Singular Value Decomposition Method

The least-squares (LS) technique addresses the problem of

$$A\ x = b \tag{A.1}$$

where no solution exists (where x is the parameter vector, b is the observation, and A is the design matrix). In principle the LS method determines a vector x that makes A x as close to b as possible. This is done by finding the minimum distance between Col A (column space of A) and b. Naively, this is simply analogous to the difference in the length (or norm) between the vectors. The length between to vectors u and u is the dot product:

$$\sqrt{(u \cdot u)} = \sqrt{u^T u} \tag{A.2}$$

and superscript T designates the transpose of a matrix). Therefore, one can write the distance between the vectors u and v:

$$dist(u, v) = \sqrt{\left[(u_1 - v_1)^2 + (u_2 - v_2)^2 + \ldots\right]} \tag{A.3}$$

Furthermore, the essence of the LS technique is the orthogonality condition (concerning projections), where there is a unique vector $\boldsymbol{y}$ in W space such that y - $\boldsymbol{y}$ is orthongonal to W. This is applied to the orthogonal *decomposition* theorem which reformulates y as a linear combination of an orthogonal basis of W ($\boldsymbol{y}$) and a basis orthogonal to W, noted as $W^{\perp}$. The set of solutions to the linear LS problem coincide with the solutions of

$$A^T A\ x = A^T b \tag{A.4}$$

Single value decomposition (SVD) of A is defined as

$$A = U\ \Sigma\ V^T \tag{A.5}$$

where Σ has m - r rows and n - r columns (with the matrix D imbedded). U and V are orthogonal (m x m) and (n x n) matrices, respectively. The D matrix is r x r and has diagonal entries of increasing rank ($d_1 \geq d_2 \geq \ldots \geq d_r \geq 0$). The most common method for solving the LS problem utilizes the reduced singular value decomposition and the pseudoinverse method (a clever method for calculating a matrix inversion, also known as the Moore-Penrose inverse). If Σ contains zeros, a *reduced* SVD can be employed where

$$U = \left[u_r \cdots u_{m-r}\right] \quad and \quad V = \left[v_r \cdots v_{n-r}\right] \tag{A.6}$$

The more compact decomposition of A is $U_r D V^T_r$, where the pseudoinverse of A is

$$A^+ = U_r\ D^{-1}\ V_r^T \tag{A.7}$$

Given A x = b and $\boldsymbol{x} = A^+ b$ then

$$A\ x = U_r\ U_r^T\ b \tag{A.8}$$

The othogonal proj ***b*** of b onto Col A is $U_r U^T_r$ b, if U is an orthonormal basis of W then proj $_W$ y = U U^T y. Ergo, ***x*** has the smallest norm of all LS solutions of A x = b.

For more details concerning this analysis technique: Wise, W., M. Rosker, G. Millhauser, and C. Tang, *Application of linear prediction least-squares fitting to time-resolved optical spectroscopy.* IEEE Journal of Quantum Electronics, 1987. **QE-23**(7): pp. 1116-1121. The LPSVD code employed by the author was modeled after the particulars in the following reference: Kumaresan, R. and D. Tufts, *Estimating the parameters of exponentially damped sinusoids and pole-zero*

modeling in noise. IEEE Transactions on Acoustics, Speech and Signal Processing, 1982. **30**(6): 833-840.

APPENDIX B

Nonlinear Least Squares Fitting Method

The nonlinear regression is based on the Levenberg-Marquardt algorithm, which amalgamates the methods of gradient descent (GD) and Gauss-Newton iteration (GNI). The GD finds the function minima by adding the negative of the scaled gradient at each step:

$$x_{i+1} = x_i - \lambda \; grad\left[f\right] \tag{B.1}$$

where f is a function of x_i and λ is a free parameter used to either increase or decrease the effect of the gradient. The GNI employs additional curvature information (i.e., second derivative) by expanding the gradient in a Taylor expansion:

$$grad\left[f\left(x\right)\right] = grad\left[f\left(x_0\right)\right] + \left(x - x_0\right)^T \left(grad\left[f\left(x_0\right)\right]\right) + \ldots \tag{B.2}$$

Truncation assumes the function is quadratic about x_0. The system is minimized by setting that gradient to zero (where the superscript T designates the transpose of a matrix). The update rule (improved upon by Marquardt:

$$x_{i+1} = x_i - \left\{ \left(grad\left[f\right]\right)^2 + \lambda \; diag\left[\left(grad\left[f\right]\right)^2\right] \right\}^{-1} grad\left[f\right] \tag{B.3}$$

where f is a function of x_i) is based on these two minimizations where if the error decreases following an update, the contribution of GD (λ) is decreased (quadratic assumption is working) while if the error increases then the contribution of GD is increased (to follow the gradient more closely). Note that given the Jacobian matrix (and its transpose) both the gradient and the square of the gradient can be calculated. (This is only valid if the residuals are small using the quadratic approximation.)

For more details concerning this analysis technique see the following two references:

Levenberg, K., *A method for the solution of certain non-linear problems in least squares*. Quarterly of Applied Mathematics, 1944. **2**: pp. 164-168.

Marquardt, D., *An algorithm for least-squares estimation of nonlinear parameters*. Journal of the Society for Industrial and Applied Mathematics, 1963. **11**: pp. 431-441.

The End ☺